

**Metal-organic nanowires:
Microfluidic-based synthesis, optical and
electrical characterization and label-free
sensing applications**

vorgelegt von
Master of Science (M. Sc.)
Yanlong Xing
aus Zibo, China

Von der Fakultät II – Mathematik und Naturwissenschaften
der Technischen Universität Berlin
zur Erlangung des akademischen Grades
doctor rerum naturalium (Dr. rer. nat.)
genehmigte Dissertation

Promotionsausschuss:

Vorsitzende: Prof. Dr. Birgit Kanngießer (Technische Universität Berlin)

Gutachter: Prof. Dr. Norbert Esser (Technische Universität Berlin)

Gutachter: Prof. Dr. Peter Hildebrandt (Technische Universität Berlin)

Gutachterin: Prof. Dr. Petra. S. Dittrich (Eidgenössische Technische Hochschule
Zürich)

Tag der wissenschaftlichen Aussprache: 21. Oktober 2016

Berlin 2016

For my family...

List of publications

Journal Articles

1. Yanlong Xing, Andreas Wyss, Norbert Esser and Petra S. Dittrich*, Label-free biosensors based on *in situ* formed and functionalized microwires in microfluidic devices, *Analyst*, 2015, 140, 7896-7901.
2. Yanlong Xing, Norbert Esser, Petra S. Dittrich*, Conductive single nanowires formed and analysed on microfluidic devices. *Journal of Material Chemistry C*, 2016, 4, 9235-9244.
3. Yanlong Xing, Guoguang Sun, Eugen Speiser, Norbert Esser and Petra S. Dittrich*, Localized synthesis of conductive Cu-TCNQ nanostructures in ultra-small microchambers for nanoelectronics. Ready for submission. Oct. 2016.
4. Yanlong Xing, Eugen Speiser, Petra S. Dittrich and Norbert Esser*, Polarized confocal Raman microscopy of TTF crystal and single Au-TTF nanowires. Oct. 2016, Manuscript prepared.

Conference Proceedings

1. Yanlong Xing, Eugen Speiser, Dheeraj Kumar Singh, Petra S. Dittrich, Norbert Esser, the 2016 Raman Fest Conference, May 2016, Berlin, Germany (Poster, 3rd prize of *Best Poster Award*).
2. Yanlong Xing, Eugen Speiser, Princia Salvatore, Petra S. Dittrich, Norbert Esser, the 8th congress on X-ray analytics for industrial processes (PRORA 2015), November 2015, Berlin, Germany (Poster).
3. Mario Lenz, Yanlong Xing, Petra. S. Dittrich, 4th International Symposium on Sensor Science, July 2015, Basel, Switzerland (Poster).
4. Yanlong Xing, Andreas Wyss, Norbert Esser, Petra. S. Dittrich, 9. Deutsches BioSensor Symposium, March 2015, Munich, Germany (Poster).
5. Yanlong Xing, Norbert Esser, Petra S. Dittrich, EMBL Conference, Microfluidics 2014, July 2014, Heidelberg, Germany (Poster).

Abstract

Metal-organic nanowires exhibit not only the properties of one-dimensional structures including ultra-small scale, large surface-to-volume ratio *etc.*, but also obvious advantages in their tunable properties and label-free sensing ability by optical or electrical readout. Thus, the evaluation of metal-organic materials by the use of transition metal ions and organic ligands including tetrathiafulvalene (TTF) and tetracyanoquinodimethane (TCNQ) were focused in this thesis. Concerning the synthesis of metal-organic nanowires, microfluidics offers various benefits, e.g. laminar flow, reduced sample/reagent consumption and control of self-assembly of nanostructures. Therefore, microfluidic techniques have been mainly applied to the synthesis and application of nano-/microstructures.

In the first part of this thesis, label-free biosensors based on *in situ* formed and functionalized gold-tetrathiafulvalene (Au-TTF) wires were developed using an integrated microfluidic system. Au-TTF microwires were formed and immobilized inside the microchip. Then, different surface modification protocols were applied to modify Au-TTF wires which were used for sensitive label-free detection of catecholamines and human IgG by Raman spectroscopy.

Following, a study of molecular self-organization in individual Au-TTF nano-/microwire by polarized confocal Raman spectroscopy was performed to understand the growth mechanism of Au-TTF. Single nanowires were analysed using non-destructive polarized Raman spectroscopy. Angular polarization Raman measurement of a single TTF crystal and single nanowire showed the periodic variations in typical Raman bands, indicating preferential ordering of molecules in both crystal and Au-TTF wire. Based on the density functional theory (DFT) calculation and simulation of depolarization ratio, the molecular assembly in a single TTF crystal was confirmed. The tilted stacking of TTF units in single Au-TTF nanowire along the long axis was also proved.

Afterwards, the formation of fibres and particles made of metal salts and TTF derivatives on a microfluidic device and in a conventional reaction flask was investigated. Their morphologies, optical properties and electrical conductivities were characterized. This study provides a comprehensive overview of the morphologies of the products obtained from reactions between metals and different commercially available TTF derivatives.

Finally, a microfluidic-assisted synthesis of copper-tetracyanoquinodimethane (Cu-TCNQ) nanostructures based on TCNQ was performed. A two-layer microfluidic device comprising parallel actuated microchambers was used for the synthesis, and enabled the excellent fluid handling for the continuous and multiple chemical reactions in confined ultra-small chambers. The as-prepared Cu-TCNQ wire bundles showed good conductivity and hysteresis reversing memory effect, which proved the possibility in using them to build advanced nanoelectronics.

Zusammenfassung

Metall-organische Nanodrähte besitzen nicht nur die Eigenschaften eindimensionaler Materialien wie z.B. großes Oberflächen-Volumen-Verhältnis, Teilchengrößen im Nanometerbereich usw., sondern haben auch bedeutende Vorteile durch ihre durchstimmbaren Eigenschaften und den Einsatz als markierungsfreie Sensoren für optische oder elektronische Messungen. Deshalb legt die vorliegende Arbeit den Fokus auf die Charakterisierung von metall-organischen Materialien, die aus Übergangsmetallionen und organischen Liganden wie Tetrathiafulvalen (TTF) und Tetracyanochinodimethan (TCNQ) synthetisiert werden. Für die Synthese von metall-organischen Nanodrähten eignen sich Mikrofluidik-Techniken besonders gut, da sie laminare Strömungen erzeugen, in denen die Zufuhr von Substanzen sehr genau kontrolliert werden kann.

Der erste Teil dieser Dissertation enthält die Entwicklung von markierungsfreien Biosensoren basierend auf *in situ* produzierten und funktionalisierten Gold-Tetrathiafulvalen (Au-TTF)-Drähten mittels eines integrierten mikrofluidischen Systems. Zunächst wurden Au-TTF-Mikrodrähte in einem Mikrochip gebildet und immobilisiert. Daraufhin wurden verschiedene Modifikationsprotokolle angewandt um die Au-TTF-Drähte für den sensitiven und markierungsfreien Nachweis von Katecholaminen und menschlichem IgG mit Raman-Spektroskopie vorzubereiten.

Im Anschluss an diesen Teil folgt eine Studie der molekularen Selbstorganisation in individuellen Au-TTF-Nano-/Mikrodrähten mit zerstörungsfreier, konfokaler Polarisations-Raman-Spektroskopie um den Wachstumsmechanismus der Drähte genauer zu verstehen. Polarisations-Raman-Spektren eines einzelnen TTF-Kristalls und eines einzelnen TTF-Nanodrahts zeigten die üblichen periodischen Abhängigkeiten der polarisationsabhängigen Raman-Moden und ließen so auf eine bevorzugte räumliche Anordnung der Moleküle sowohl im Kristall als auch in den Drähten schließen. Basierend auf DFT-Berechnungen und der Simulation des Depolarisierungsverhältnisses konnte die molekulare Anordnung in einem einzelnen TTF-Kristall bestätigt werden. Die Stapelung von gekippten TTF-Einheiten in einzelnen Au-TTF-Nanodrähten entlang der langen Achse konnte ebenfalls bewiesen werden.

Im dritten Teil der vorliegenden Arbeit wurde die Bildung von Fasern und Teilchen aus Metallsalzen und TTF-Derivaten in einem mikrofluidischen System und einem konventionellen Reagenzglas untersucht. Morphologien, optische Eigenschaften und elektrische Leitfähigkeiten wurden charakterisiert. Die Ergebnisse geben eine umfassende Übersicht über die Beschaffenheit der Reaktionsprodukte zwischen Metallsalzen und verschiedenen kommerziell erwerblichen TTF-Derivaten.

Schlussendlich wurde die Synthese von Kupfer-Tetracyanochinodimethan (Cu-TCNQ)-Nanostrukturen durchgeführt. Als Basis diente eine mikrofluidische Doppelzelle bestehend aus zwei parallel betriebenen Mikrokammern, wodurch eine exzellente Steuerung der Flüssigkeiten für kontinuierliche und multiple chemische Reaktionen innerhalb der Kammern möglich war. Die hergestellten Cu-TCNQ-Bündel zeigten gute Leitfähigkeitswerte und ein Hystereseverhalten und bestätigten somit die Verwendungsmöglichkeit als innovative nanoelektronische Komponenten.

List of Figures

- 1.1. Chemical structures of TTF, its cation radical TTF⁺ and dication TTF²⁺.
- 1.2. Chemical structures of TCNQ and its anion radical.
- 1.3. Stacking of charge-transfer salts.
- 1.4. Crystal structure of TTF-TCNQ 2:1 charge-transfer compound (ac face).
- 1.5. The formation of Au-TTF nanowires by charge-transfer.
- 1.6. The synthesis of Ag-TCNQ complex.
- 2.1. Microfluidic synthesis based on continuous laminar flow.
- 2.2. Microfluidic device with valves.
- 2.3. Microfluidic-assisted application of conductive nanostructures.
- 2.4. Images of chrome masks and wafers used in this thesis.
- 2.5. A photograph of a glass slide with microelectrodes.
- 2.6. The formation of PDMS by catalytic cross-linking reaction.
- 2.7. Photographs of two microchips used in this project.
- 3.1. Simplified Jablonski diagrams of light scattering.
- 3.2. Raman spectrum of TCNQ under laser excitation of 532 nm.
- 3.3. Components of a polarized confocal Raman microscope with backscattering geometry.
- 4.1. Images of TTF crystal and Au-TTF nano-/microwires.
- 4.2. Photograph of microchips and optical image of microchannels.
- 4.3. Schematic illustration of Cu-TCNQ wire formation in microchamber.
- 4.4. Optical images of a microchamber showing the operation of control layer.
- 4.5. Photographs of conductivity measurement devices.
- 5.1. Graphic abstract showing the sensing mechanism of the *in situ* label-free sensor in this work.
- 5.2. The open-donut microchip and its features.
- 5.3. Images of Au-TTF wire formation.
- 5.4. Characterization of Au-TTF wires.
- 5.5. A second microchip design for wire formation.
- 5.6. Fluorescent images of wires with surface modification for biosensors.
- 5.7. Control experiment without GA solution.
- 5.8. Raman spectra of various bioamines on functionalized Au-TTF wires.
- 5.9. Quantitative Raman measurement of DA based on the functionalized wire for biosensor.

- 5.10. Data analysis method of Raman spectrum.
- 5.11. Fluorescent images of wires after surface modification as immunosensor.
- 5.12. Raman measurement results of functionalized wire for immunosensor.
- 5.13. Graphic abstract of the polarization Raman measurement of TTF crystal and Au-TTF wire.
- 5.14. DFT modelling of TTF and TTF cation.
- 5.15. The view from three faces of crystalline TTF and the calculated angle between two TTF molecules in a unit cell of TTF crystal.
- 5.16. Sketch of TTF crystal and a Raman spectrum.
- 5.17. Angular variations of Raman spectra from different faces of TTF crystal under parallel and crossed polarization configurations.
- 5.18. Simulated depolarization ratio of TTF crystal.
- 5.19. Raman spectra of single Au-TTF wire under parallel (black curves) and crossed (grey curve) polarization configurations.
- 5.20. Angular variation of Raman spectra of single Au-TTF nanowire under parallel and crossed polarization configurations.
- 5.21. Simulated depolarization ratio of six Au-TTF nanowires.
- 5.22. The 3D model of Au-TTF wire showing rotation of molecules.
- 5.23. Graphic abstract of the synthesis and analysis of metal-TTF (derivatives) in this project.
- 5.24. Chemical structures of TTF derivatives.
- 5.25. Synthesis of wires, exemplary for $(\text{TTF})_7(\text{CuCl}_2)_3$ (**2a**).
- 5.26. SEM images of $(\text{TTF})_2\text{CuCl}_2$ (**2b**), $(\text{TTF})_4\text{Cu}(\text{NO}_3)_2$ (**3a**) and $(\text{TTF})_4\text{Cu}(\text{NO}_3)_2$ (**3b**).
- 5.27. SEM images of $(\text{TTF})_5\text{FeCl}_3$ (**4a**), $(\text{TTF})_5\text{FeCl}_3$ (**4b**), $(\text{TTF})_5\text{Fe}(\text{NO}_3)_3$ (**5a**) and $(\text{TTF})_5\text{Fe}(\text{NO}_3)_3$ (**5b**).
- 5.28. Optical images of products derived from compounds **6**, **7**, **8**, **9**, **10**, **11**, **12**, **13**, **14**.
- 5.29. EDX-SEM spectra of $(\text{TTF})_2\text{CuCl}_2$ (**2b**), $(\text{TTF})_4\text{Cu}(\text{NO}_3)_2$ (**3a**) and $(\text{TTF})_4\text{Cu}(\text{NO}_3)_2$ (**3b**).
- 5.30. EDX-SEM spectra of $(\text{TTF})_5\text{FeCl}_3$ (**4a**), $(\text{TTF})_5\text{FeCl}_3$ (**4b**), $(\text{TTF})_5\text{Fe}(\text{NO}_3)_3$ (**5a**) and $(\text{TTF})_5\text{Fe}(\text{NO}_3)_3$ (**5b**).
- 5.31. UV-Vis absorption spectra of solutions of **2a**, **2b**, **3a**, **3b**, **4a**, **4b**, **5a**, **5b**, **6**, **7**, **8**, **9**, **10**, **11**, **12**, **13**, **14**.
- 5.32. IR spectra of compounds $(\text{TTF})_7(\text{CuCl}_2)_3$ (**2a**) and $(\text{TTF})_4\text{Cu}(\text{NO}_3)_2$ (**3a**).
- 5.33. Raman spectra of compounds **2a**, **2b**, **3b**, **4a**, **4b**, **5a** and **5b** at 532 nm excitation.

- 5.34. Representative I - V curves of single nanowires of M-TTF complexes.
- 5.35. Linear range of the I - V curves in Figure 5.34 with the electrical conductivities of single nanowires of **2a**, **2b**, **3a**, **3b**, **4a**, **4b**, **5a** and **5b**.
- 5.36. UV-Vis absorption spectra of the solutions of M-FTTF.
- 5.37. Optical and SEM images of M-FTTF generated by bulk synthesis and on microchip.
- 5.38. Optical images of structures from **17**, **18**, **19**, **20**, **21** and **22** in bulk and on microchips.
- 5.39. IR spectra of M-FTTF complexes.
- 5.40. EDX-SEM spectra of M-TTF complexes.
- 5.41. I - V curves of M-FTTF nanowires.
- 5.42. Optical images of compounds **28**, **29** and **30**.
- 5.43. UV-Vis absorption spectra of solutions of M-BEDT-TTF.
- 5.44. Optical images of compounds **23**, **24**, **25**, **26** and **27** formed in bulk synthesis.
- 5.45. SEM images and I - V curves of structures of **23**, **25** and **27**.
- 5.46. SEM images and I - V curves of structures of **24** and **26**.
- 5.47. Linear I - V curves and calculated electrical conductivity of single wires of **23**, **25** and **27**.
- 5.48. EDX-SEM spectra of M-BEDT-TTF.
- 5.49. Sensing of organic gases by single Au-TTF wire.
- 5.50. Graphic abstract of the synthesis, characterization and analysis of Cu-TCNQ.
- 5.51. Microchip device for the synthesis of Cu-TCNQ structures.
- 5.52. Photograph of Cu⁰ and Cu-TCNQ.
- 5.53. The Cu⁰ layer and Cu-TCNQ formed by using different concentrations of Cu²⁺ and reductant.
- 5.54. SEM images and EDX spectra of Cu-TCNQ nanostructures.
- 5.55. UV-Vis absorption spectra of TCNQ (black) and Cu-TCNQ (red) solutions in CH₃CN.
- 5.56. FT-IR and Raman analysis of TCNQ and Cu-TCNQ.
- 5.57. EDX-SEM spectra of a) glass slide and b) Cu-TCNQ microstructures.
- 5.58. FT-IR and Raman Characterization of Cu-TCNQ microstructures.
- 5.59. I - V characteristics of Cu⁰ and Cu-TCNQ at room-temperature.
- 7.1. Structures of catecholamines and aromatic amino acids.

List of Schemes

- 2.1. Schematic of the microfabrication steps of a SU-8 master mold.
- 2.2. Schematic of the microfabrication steps of an AZ master mold.
- 5.1. Functionalization on Au-TTF wire for the sensing of amines (RNH_2).
- 5.2. Functionalization of Au-TTF wire for immunoassay.
- 5.3. Reaction mechanisms for binding of fluorophores to the SAM of 4-ATPh.
- 5.4. Reaction mechanism for the formation of Cu^0 and Cu-TCNQ.

List of Tables

- 2.1. An overview of the microdevices used in different Chapters of this thesis.
- 5.1. Raman tensors for the symmetry classes of the C_{2v} and D_{2h} point groups.
- 5.2. Calculated Raman tensor values.
- 5.3. Raman assignments of TTF, TTF^{n+} ($0 < n < 1$) and TTF^+ .
- 5.4. An overview of the experimental parameters, morphology, conductivity and characterization of metal-TTF (and derivatives) complexes.
- 5.5. Elemental analysis of compounds **2a**, **2b**, **3a**, **3b**, **4a**, **4b**, **5a** and **5b**.
- 5.6. IR assignments of TTF^0 and TTF^+ .
- 5.7. IR assignments of other M-TTF compounds **2b**, **3b**, **4a**, **4b**, **5a** and **5b**.
- 5.8. Elemental analysis of **15** and **16** complexes.
- 5.9. Morphology of structures formed under different reaction conditions on microchip.

List of Equations

- 1.1. Electrical resistive switching properties of M-TCNQ.
- 2.1. Reynolds number in microfluidic system.
- 3.1. Energy equation in IR absorption.
- 3.2. Definition of induced molecular dipole moment μ_{ind} .
- 3.3. Definition of nuclear displacement Q_k .
- 3.4. Definition of molecular polarizability α .
- 3.5. General expression of induced dipole moment.
- 3.6. The Raman scattering intensity I .
- 3.7. Definition of depolarization ratio P .
- 5.1. Definition of depolarization ratio with a constant factor D .
- 5.2. The reversible switching states of Cu-TCNQ upon voltage sweeping.

Abbreviations and Acronyms

A	Acceptor
Ag-TCNQ	Silver-tetracyanoquinodimethane
4-ATPh	4-aminothiophenol
Au-TTF	Gold-tetrathiafulvalene
BEDT-TTF	Bis(ethylenedithio)tetrathiafulvalene
CAD	Computer-aided design
CEA	Cysteamine
CH ₃ CN	Acetonitrile
C ₆ H ₅ O ₇ Na ₃	Sodium citrate dehydrate
CoCl ₂ ·6H ₂ O	Cobalt(II) chloride hexahydrate
Co(NO ₃) ₂	Cobalt(II) nitrate
CuCl	Copper(I) chloride
CuCl ₂	Copper(II) chloride
Cu(NO ₃) ₂	Copper(II) nitrate
CuSO ₄	Copper(II) sulfate
Cu-TCNQ	Copper-tetracyanoquinodimethane
D	Donor
1D	One dimensional
DA	Dopamine
DFT	Density functional theory
DI	Deionized
DMSO	Dimethyl sulfoxide
EDC	1-Ethyl-3-(3-dimethylaminopropyl)carbodiimide hydrochloride
EDX	Energy dispersive X-ray

EPI	Epinephrine
FET	Field-effect transistor
FeCl ₃	Iron(III) chloride
FeCl ₂ ·4H ₂ O	Iron(II) chloride tetrahydrate
Fe(NO ₃) ₃	Iron(III) nitrate
FTTF	Formyl-tetrathiafulvalene
GA	Glutaldehyde
HWP	Half-wave plate
HAuCl ₄	Hydrotetrachloroaurate
IgG	Immunoglobulin G
IR	Infrared
ISP	Isoprenaline hydrochloride
<i>I-V</i>	Current-voltage
K-TCNQ	Potassium-tetracyanoquinodimethane
LP	Linear polarizer
MnCl ₂	Manganese(II) chloride
μTAS	Micro total analysis systems
NA	Numerical aperture
NaBH ₃ CN	Cyanoborohydride
NaBH ₄	Sodium borohydride
NaOH	Sodium hydroxide
Na-TCNQ	Sodium-tetracyanoquinodimethane
Nd:YAG	Neodymium yttrium aluminium garnet
NE	Norepinephrine hydrochloride
NHS	N-Hydroxysuccinimide
Ni(NO ₃) ₂	Nickel(II) nitrate hexahydrate
nm	nanometre
PBS	Phosphate buffered saline

PDMS	Polydimethylsiloxane
Phe	Phenylalanine
PA	Polarizer analyser
Pt	Platinum
SAM	Self-assembled monolayer
SEM	Scanning electron microscopy
SERS	Surface-enhanced Raman scattering
SWNT	Single-walled carbon nanotube
TCE-TTF	2,3,6,7-Tetrakis(2-cyanoethylthio)tetrathiafulvalene
TCNQ	Tetracyanoquinodimethane
TET-TTF	Tetrakis(ethylthio)tetrathiafulvalene
THF	Tetrahydrofuran
TTF	Tetrathiafulvalene
TTF-TCNQ	Tetrathiafulvalene-tetracyanoquinodimethane
Tyr	Tyrosine
μm	Micrometre
μM	Micromolar
VOC	Volatile organic compounds
ZnCl_2	Zinc chloride
$\text{Zn(NO}_3)_2$	Zinc nitrate hexahydrate

Contents

1 Introduction	1
1.1 Electron donor and acceptor molecules	1
1.2 Metal-organic charge-transfer complexes	4
1.3 One-dimensional (1D) nanostructures	7
1.4 Scope of the thesis	9
2 Methods-1: Microfluidics and microfabrication	13
2.1 Introduction to microfluidics	13
2.2 Microfluidic-guided synthesis of nano-/microwires	14
2.3 Microfluidic-assisted application of nano-/microwires	18
2.4 Microfabrication	20
2.4.1 Wafers and masters	20
2.4.2 Soft lithography	23
2.4.3 Microchip fabrication	24
3 Methods-2: Raman microspectroscopy	27
3.1 Raman scattering	27
3.1.1 Stokes, anti-Stokes and resonance Raman scattering	27
3.1.2 Raman spectroscopy and fingerprint	29
3.1.3 Raman and Infrared spectroscopy	31
3.2 Theoretical basis of Raman scattering	31
3.2.1 Normal modes	31
3.2.2 Polarizability and Raman selection rules	32
3.2.3 Raman tensor	33
3.3 Light polarization and depolarization ratio	33
3.4 Confocal and polarized Raman microscopy: principles and setups	34
3.4.1 Confocal Raman microspectroscopy	34

3.4.2 Polarized Raman microspectroscopy.....	36
3.4.5 <i>In situ</i> Raman measurements.....	37
3.5 Instrumentation for Raman spectroscopy.....	37
4 Methods-3: Sample preparation and characterization	39
4.1 Microchip operation.....	39
4.2 <i>In situ</i> synthesis, immobilization and functionalization of Au-TTF microwires	39
4.2.1 <i>In situ</i> synthesis and immobilization of Au-TTF microwires	39
4.2.2 Functionalization protocol for biosensing applications	40
4.2.3 Functionalization protocol for immunosensing applications.....	41
4.3 Synthesis of TTF crystal and Au-TTF nano-/microwires	42
4.4 Microfluidic synthesis of metal-TTF structures.....	43
4.5 <i>In situ</i> formation of Cu-TCNQ nano-/microstructures.....	45
4.6 Sample characterization.....	47
4.6.1 Electrical characterization	47
4.6.2 Other characterization techniques.....	49
4.7 Methods for data analysis	50
4.7.1 Data analysis of fluorescent images, Raman, IR spectra and <i>I-V</i> curves	50
4.7.2 DFT calculations	50
4.7.3 Single TTF crystal analysis	51
5 Results and discussion.....	53
5.1 Label-free biosensors based on <i>in situ</i> formed and functionalized microwires in microfluidic devices.....	53
5.1.1 Microchip and synthesis of Au-TTF microwires.....	55
5.1.2 Label-free biosensing of catecholamines.....	59
5.1.3 Label-free immunosensors for detection of human IgG	65
5.2 Study of molecular self-organization in TTF crystals and individual Au-TTF nano-/microwires by polarized confocal Raman spectroscopy	71

5.2.1 DFT calculations of Raman tensor	72
5.2.2 Polarized confocal Raman spectra of single TTF crystals	74
5.2.3 Polarized confocal Raman spectra of single Au-TTF nanowires ..	81
5.3 Conductive single nanowires formed and analysed on microfluidic devices.....	87
5.3.1 Microfluidic guided synthesis of charge-transfer complexes	88
5.3.2 Metal-TTF complexes	93
5.3.3 Metal-FTTF complexes	108
5.3.4 TCE-TTF, TET-TTF and BEDT-TTF	113
5.3.5 Metal-BEDT-TTF nano-/microstructures.....	114
5.3.6 Sensing of organic gases by single TTF-based wires	120
5.4 Localized synthesis of conductive Cu-TCNQ nanostructures in ultra-small microchambers for nanoelectronics.....	123
5.4.1 Microchips with a microchamber array	125
5.4.2 Reaction mechanism.....	126
5.4.3 Controlled synthesis of Cu and Cu-TCNQ structures.....	126
5.4.4 Characterization of Cu-TCNQ nanostructures	130
5.4.5 Characterization of Cu-TCNQ microstructures	134
5.4.6 Electrical properties of Cu-TCNQ nano-/microstructures	135
6 Conclusions and outlook.....	139
Bibliography	143
Appendix.....	159
Acknowledgement	161
Statement of authorship.....	163

1 Introduction

1.1 Electron donor and acceptor molecules

Electron donors refer to those molecules rich in electrons, which can act as a reducing agent and transfer electrons to electron acceptors in reactions. It is reported that the most promising candidates for good organic electron donors are multisulphur heterocycles, such as TTF. Since its discovery in 1970,¹ this well-known organic electron donor has received intense focus on synthesizing conductive compounds via charge-transfer. The reaction between TTF and the strong electron acceptor, TCNQ,² results in the formation of TTF-TCNQ (tetrathiafulvalene-tetracyanoquinodimethane) nanowires which show metallic conductive behaviour.^{3,4} This explains ongoing research interest in developing organic conductive materials, as well as studying the mechanism of organic electronics based on TTF.

TTF consists of two five-membered rings connected by a carbon-carbon double bond. It is an excellent electron donor because each 1,3-dithiole ring has seven π -electrons (one from each carbon and two from each sulphur), so that the monocationic state has six π -electrons.⁵ In early studies,⁶ it was considered that TTF had a planar structure. However, in modern studies it is widely accepted that the neutral TTF shows boat-like conformation while charged TTF has a planar molecular structure, on the basis of theoretical calculation results.^{7,8} Upon charge-transfer, TTF can form the cations TTF⁺ and TTF²⁺ (Figure 1.1).

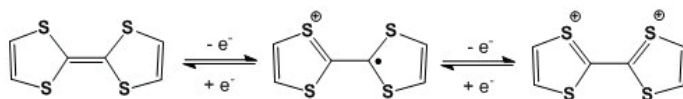


Figure 1.1. Chemical structures of TTF, its cation radical TTF⁺ and dication TTF²⁺.⁹

In a charge-transfer reaction, when the electron acceptor (e.g. metal ion) is in excess, both TTF⁺ and TTF²⁺ can be formed.¹⁰ Thus, a mixed-valence of TTF units (TTF⁺ and TTF²⁺) exists in the final charge-transfer compounds. The compounds with TTF²⁺ showed low conductivity ($<10^{-4}$ S cm⁻¹).^{10,11} In contrast,

when TTF is in excess, only TTF^+ is formed. As a result, the mixed-valence states, i.e., TTF^0 and TTF^+ are present in the obtained complexes.^{10,12,13} It has been reported that the common feature of conductive donor-acceptor complexes is the mixed-valence (or partial-oxidation) state of constituent molecules in the compound. Thus, appropriate oxidants are needed for the preparation of conductive TTF-based complexes which can oxidize TTF^0 partially to TTF^{n+} ($n < 1$). In this work, in order to obtain conductive nano-/microstructures, the concentration of TTF solution is higher than metal salt, so that partially oxidized TTF (TTF^0 and TTF^+) were formed in the charge-transfer complexes (detailed results can be found in Chapter 5.3).

Apart from TTF, its seleno and telluro analogues show good conductivities for organic conductors. These two analogues were not used in this project, so no further discussion in this thesis. Detailed information can be found in literature.⁵ Various TTF derivatives are reported for building organic conductors, and this makes TTF to be the widely used electron donor molecule. For example, a TTF derivative bis(ethylenedithio)tetrathiafulvalene (BEDT-TTF) which exhibits predominant electrical properties, has been used as electron donors to form charge-transfer compounds.¹⁴

Electron acceptors refer to the molecules that accept electrons from electron donors and act as the oxidizing agent in reaction. TCNQ is a well-known strong electron acceptor with the strong electron withdrawing cyano-group in the structure (Figure 1.2). It was first synthesized in 1973, and was found to yield a class of anion-radical derivatives with high stability and low resistivity.² Upon the reaction with electron donors, the strong π -acid TCNQ can undergo complete electron transfer to form anion radical $\text{TCNQ}^{\cdot-}$. The resulting complexes have two series of crystalline structures, with the first series of $\text{M}^+\text{TCNQ}^{\cdot-}$ which shows high electrical resistivity, and the second one of $\text{M}^+(\text{TCNQ}^{\cdot-})\text{TCNQ}$, involving neutral TCNQ in the structure and exhibiting low electrical resistivity. Figure 1.2 shows the molecular structure of TCNQ and its anion radical $\text{TCNQ}^{\cdot-}$.

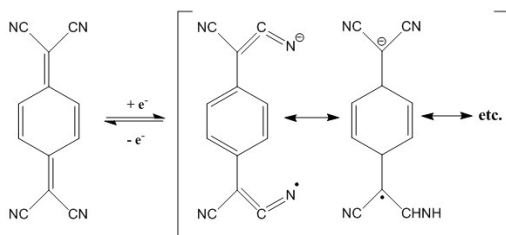


Figure 1.2. Chemical structures of TCNQ and its anion radical.²

TTF can react with different electron acceptors to form a variety of electrical conductive materials from insulators to superconductors.¹⁰ The electrical properties of TTF-based complexes depend on the charge-transfer and also the stacking mode of TTF in the obtained compounds.¹⁵ As for the charge-transfer salts, the mixed-valence TTF systems showed very high electrical conductivities for organic solids.^{16,17} On the other hand, for the orientation and alignment of TTF units, the uniform spacing between the components in such complexes can contribute to the good conductive behaviour. Charge-transfer compounds will exhibit high conductivity performance when donor (D) and acceptor (A) units alternately stacked to form a mix-stack structure (Figure 1.3a).⁵ In a special case, when neutral molecules (D^0A^0) and charged molecules (D^+A^-) stacked, partial charge-transfer complexes can be obtained, with a segregated stack structure consisting of two independent columns of donors and acceptors (Figure 1.3b).¹⁸ A typical example is TTF-TCNQ, which shows segregated columnar stacks of cations (TTF^+) and anions ($TCNQ^-$), as can be seen from the crystal structure (Figure 1.4).¹⁹

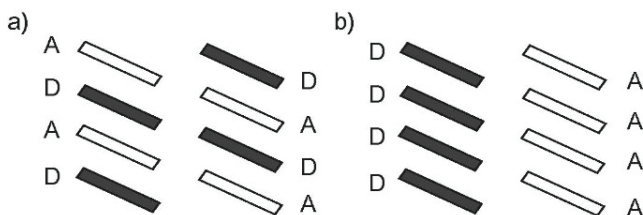


Figure 1.3. Stacking of charge-transfer salts. a) Mixed-stack, and b) Segregated arrangements of D (hatched) and A (open) molecules in charge-transfer salts.⁵

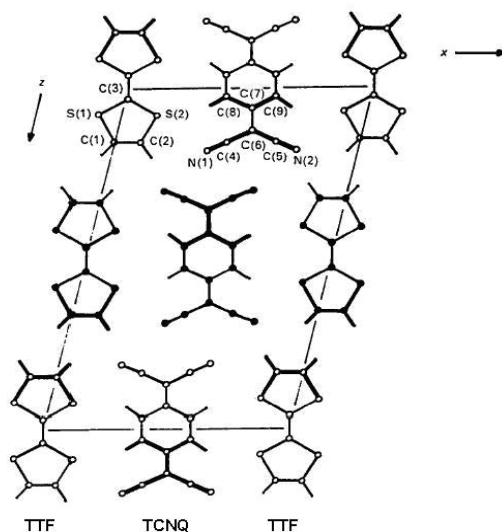


Figure 1.4. Crystal structure of TTF-TCNQ 2:1 charge-transfer compound (ac face).^{19,20} Reproduced with permission of the International Union of Crystallography.

1.2 Metal-organic charge-transfer complexes

Metal-organic frameworks refers to coordination polymers with metal ions coordinated to organic ligands to form one, two, or three-dimensional structures.²¹ Another class of metal-organic materials are charge-transfer complexes. For metal-organic charge-transfer compounds, organic conductors which are characterized as strong electron donor and acceptors are used as organic ligands. When TTF is used as electron donor, an oxidized state of metal ions will be the electron acceptor.¹² When TCNQ is applied as oxidizing agent, a neutral metal is required in spontaneous electrolysis process,²² while metal ions can be used in electro-crystallization synthesis.²³

Because of the properties mentioned in Chapter 1.1, TTF has been widely used not only for synthesis of numerous organic conductors, but also as a precursor for low scale self-assembled structures formed upon reaction with transition metal salts. Various metal-TTF charge-transfer compounds have been synthesized, either in bulk reactions²⁴⁻²⁶ or by microfluidics.^{27,28} These metal-organic complexes showed different morphologies, such as dendritic,²⁶ rod

like,²⁴ wire like,²⁷ *etc.*, among which wire-like structures exhibited the most intriguing characteristics. TTF-based metal-organic charge-transfer nanostructures were synthesized by self-organization of the 1D stacking of TTF component. A typical structure was Au-TTF, which was generated by the redox reaction between TTF and hydrotetrachloroaurate (HAuCl_4) solutions (Figure 1.5).²⁴ The electron transfer between TTF and Au(III) induced the formation of TTF radical cation ($\text{TTF}^{\cdot+}$) and neutral Au^0 . The 1D crystalized nanowires were formed with a backbone of the mixed stacking of neutral TTF (or derivatives) and TTF (or derivatives) radical cation.^{24,25}

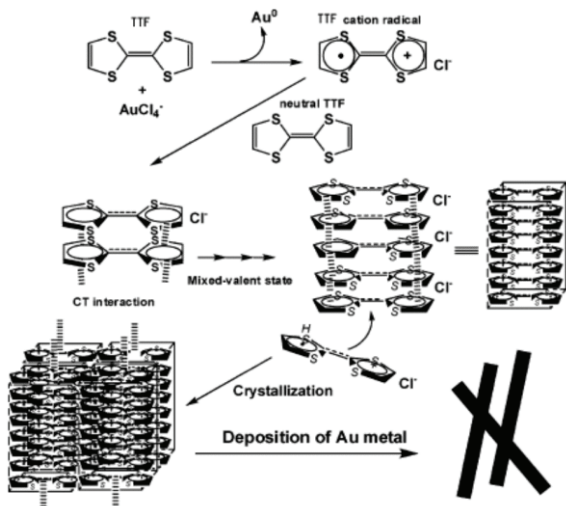


Figure 1.5. The formation of Au-TTF nanowires by charge-transfer. Reprinted with permission from (Naka, K.; Ando, D.; Wang, X.; Chujo, Y. *Synthesis of Organic-Metal Hybrid Nanowires by Cooperative Self-Organization of Tetrathiafulvalene and Metallic Gold via Charge-Transfer*, *Langmuir* 2007, 23, 3450-3454).²⁴ Copyright (2007) American Chemical Society.

In the present work, the synthesis of Au-TTF nano-/microwires was achieved both by bulk synthesis and on microchips. The diameter of these wires varied according to the synthesis method, either by stirring in bulk, or by laminar flow or diffusion-based synthesis on microchips (see details in Chapters 5.1 and 5.3). Due to the existence of the mixed-valence of TTF, Au-TTF wires showed good

conductivity behaviour. The source-drain current of single Au-TTF wires were measured, with no gate effect observed in the measurement, indicating the metallic behaviour of Au-TTF charge-transfer wires.²⁷ Furthermore, due to the existence of Au⁰, surface modification on the active surface of Au-TTF was possible by adding Au-active molecules into the system. For example, fluorescent carboxylate-modified nanoparticles were used to bind on Au-TTF nano-/microwire surface.^{27,29}

Metal-organic charge-transfer salts based on TCNQ exhibit good conducting and magnetic properties.^{5,30,31} The synthesis of TCNQ-based materials has received considerable research interest due to potential applications in optical, electrical and sensing devices.^{32,33} TCNQ acts as a bidentate, as well as a tetradentate organic bridging ligand, which allows the formation of products with 1:1 and 1:2 metal-TCNQ ratios.³⁴⁻³⁶ TCNQ can react with metal ions to form stable 1:1 charge-transfer complexes like K-TCNQ and Na-TCNQ, which are highly 1D compounds, consisting of TCNQ stacks and showing semiconductor behaviour above room temperature.³⁷ The 1:1 charge-transfer complexes of Ag and Cu are of intense interest due to the fact that these complexes undergo electric field induced bistable switching effect.^{38,39} In particular, Ag-TCNQ and Cu-TCNQ can form quasi-1D wire-like structures, which make them intriguing in the field of nanoelectronics.⁴⁰ Apart from their good resistive-switching properties, Ag-TCNQ and Cu-TCNQ have showed their advantages over other organic memory materials because they can be formed via self-assembly on the corresponding metal by spontaneous chemical reaction with TCNQ (either in gas⁴¹ or solution³⁹ phase). This aspect is very promising to fabricate novel nanoelectronic memory devices. Figure 1.6 shows a typical synthesis of Ag-TCNQ by spontaneous electrolysis method.

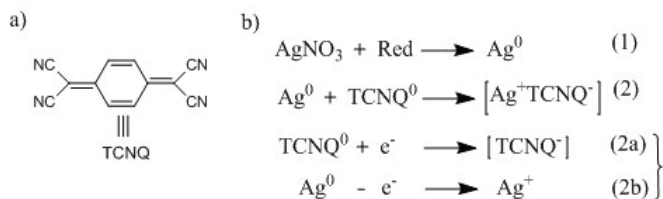
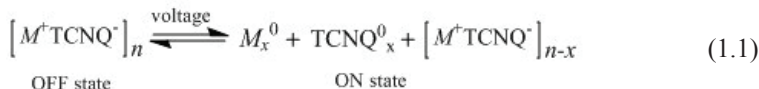


Figure 1.6. The synthesis of Ag-TCNQ complex. a) Structure of TCNQ molecule. b) Equations showing the reactions towards Ag-TCNQ wire formation. (1) The silver ion salt (AgNO_3) is reduced by reductant (Red) to metallic silver (Ag^0). (2) Neutral Ag

spontaneously reacts with TCNQ to form the charge-transfer complexes Ag^+TCNQ^- . For the formation of Ag-TCNQ , two steps can be illustrated: with (2a) TCNQ reduced to TCNQ^- and simultaneously (2b) Ag^0 is oxidized to Ag^+ .²⁸ Reprinted with permission from (Cvetkovic, B. Z.; Puigmarti-Luis, J.; Schaffhauser, D.; Ryll, T.; Schmid, S.; Dittrich, P. S. Confined Synthesis and Integration of Functional Materials in Sub-nanoliter Volumes, *ACS Nano* 2013, 7, 183-190). Copyright (2013) American Chemical Society.

As organometallic semiconductors, Ag-TCNQ and Cu-TCNQ exhibit bistable reproducible and electrical resistive switching properties because of the changes in composition. $\text{M}^+(\text{TCNQ}^-)$ (M represents metal, also as following) exhibits high resistance of 10^4 - $10^{12} \Omega\cdot\text{cm}$, while $\text{M}^+(\text{TCNQ}^-)(\text{TCNQ}^0)$ with neutral TCNQ shows low resistance of 0.01 - $100 \Omega\cdot\text{cm}$.⁴² When a reversible voltage is applied to M-TCNQ , it can show the reversible electronic behaviour between high resistance (OFF) and low resistance (ON) states (Equation 1.1. Reprinted with permission from *Applied Physics Letters*. Copyright (2006) AIP Publishing LLC).^{38,43}



Although the exact switching mechanism has not yet been determined, reported studies have already proved the existence of TCNQ^0 after the switching process to “ON” state.⁴⁴ Thus, in the low resistance state, neutral TCNQ contributes to the stack with TCNQ anions to form the mixed-valence structure. These results proved the importance of the organic memory complex M^+TCNQ^- in the switching process.⁴⁵

1.3 One-dimensional (1D) nanostructures

1D or quasi-1D structures such as nanowires, nanofibers, nanorods, and nanoparticles have been widely studied due to their physical properties of ultra-small scale, large surface-to-volume ratio and possible applications in the field of electronics, optics, magnetic devices, sensors, *etc.*⁴⁶⁻⁴⁸ For sensors, the size of substrate compared to that of target molecules is one of the most important factors determining the detection limit. Thus, nanowires and nanofibers are considered as optimal building blocks for sensing substrate. Their large surface-

to-volume ratio is suitable to study chemical compounds and biomolecules with high sensitivity.⁴⁹ In the past decades, different classes of materials have been extensively reported as sensor substrates, such as silicon nanowires, carbon nanotubes, metal nanowires, *etc.*^{47,49,50} However, metal-organic structures have not been explored to a large extent. Compared to other materials, nanowires made from metal-organic compounds have showed their obvious advantages in tunable properties based on the use of different metal units and organic ligands and label-free sensing by optical or/(and) conductive readout.^{28,51} Thus, using such metal-organic materials as sensing platform is one of the focuses of this research.

1D or quasi-1D structures exhibit interesting and unique properties because of the anisotropic structures, quantum confinement and high surface-to-volume ratios. The mechanical, electronic and optical properties of such structures greatly depend on their particle size. Furthermore, nanostructures are the smallest structures employed for electron transport, and thus of special interest in nanoelectronics. Therefore, the development of nano-/microstructures represents an important issue for the miniaturization of electronic devices.^{50,52,53} In the past decades, various nanostructures have been studied and reported,⁵⁴⁻⁵⁷ among which metal-organic nanomaterials⁵⁸⁻⁶⁰ showed their unique optical and electrical properties, compared to other materials such as metals, organic materials, inorganic materials and conducting polymers.

To obtain nano-/microstructures, different chemical methods have been established, such as template-assisted top-down synthesis, which is most widely used for metallic or inorganic nanowires,⁶¹⁻⁶³ while organic polymers, bio-organic and metal-organic nanomaterials can form anisotropic structures via bottom-up process.^{57,58} The variabilities in chemical reactants allow the ease of fabrication of anisotropic nanostructures, as well as fine-tuning of their physical and chemical properties. For metal-(bio)organic structures, the most common approach is based on the self-assembly of metal ions and (bio-)organic ligands in solution under certain reaction conditions,^{64,65} or with the assistance of other advanced synthesis techniques, such as electrospinning and ultrasonic.⁶⁶⁻⁶⁸ However, bulk synthesis based on above-mentioned bottom-up approaches faces the challenges including the size-selective synthesis, controlling and guiding the assembly of precursors, synthesis under less harsh experimental conditions, *etc.*^{69,70}

1.4 Scope of the thesis

The overall goal of this project is the microfluidic-assisted formation of nanowire-based sensors that are capable of detecting chemical molecules and biomolecules. With this aim, novel materials (transition metal and organic ligands, TTF and TCNQ) for metal-organic nanowire synthesis will be used and evaluated. The binding of analytes on the wire structures can be quickly determined by changes of the electrical conductivity, while the identification of the bound molecules can be done by Raman spectroscopy. Thus, highly sensitive nanosensors for the label-free detection of gaseous and liquid bioanalytes will be developed. However, several challenges such as the immobilization of the nanowires in withstand liquid flow, the optimization of the microfluidic platform to Raman spectroscopy have to be addressed.

Specifically, the main objectives of this doctoral project are in four aspects:

a) Formation of nanowires with suitable materials: Various precursors need to be tested. In particular, transition metal salts (such as Au, Ag, Cu and Fe salts) in combination with the important organic molecules TTF and TCNQ are used for synthesis in liquid. The formation of nanowires will be performed on microfluidic platforms.

b) Optical and electrical characterization of such nanowires: to determine their optical (mainly Raman) properties and conductive behaviour, depending on the size (length and diameter) as well as the material composition (Ag, Au, *etc.*). For Raman analysis, the resonance enhancement and resonance energy are necessary. This was done via polarization dependent optical analysis in the present work.

c) Localized synthesis and immobilization of wires: nano-/microwires will be synthesized in confined area of microchannel and immobilized for further modification. Both the synthesis and immobilization of the nanowires will be finished in withstand liquid flow, in this case, different valves in microchips will be applied for synthesis and trapping purposes.

d) Functionalization of the nano-/microwires for specific detection of selected molecules: to test the sensing behaviour of as-prepared nano-/microwires, these structures will be surface modified for binding target molecules. In reported work, Au-TTF nano-/microwires have shown to sense different gases by changes in electrical readout.²⁸ In addition, the Raman signal from the TTF ligand has been obviously enhanced. Based on these findings, the

use Au-TTF wires as sensing elements combined to on-chip Raman measurements can be proposed.

Based on the above mentioned objectives, the following parts of work were accomplished, with each part addressed one or more aspects of the objectives:

1) Label-free biosensors based on *in situ* formed and functionalized Au-TTF wires were developed on an integrated microfluidic system. After the synthesis of Au-TTF microwires in microchip, the immobilization of wires was achieved by pressing the control layer with nitrogen gas. With an active Au surface on Au-TTF wires, different surface modification protocols were applied to modify these wires which were used for sensitive label-free detection of catecholamines and human IgG via Raman spectroscopy. The proposed method enabled an easy functionalization of *in situ* formed structures and could favour their use as sensing elements in microfluidic devices. In this part, the objectives of localized synthesis and immobilization of wires and the functionalization for sensing application were achieved.

2) Study of molecular self-organization in single TTF crystal and individual Au-TTF nano-/microwire by polarized confocal Raman spectroscopy was performed. A detailed structure analysis of Au-TTF wires was important to understand the orientation of TTF molecules in a nanowire, the growth mechanism of Au-TTF and the influence of the absorbent on the surface. The proposed method based on polarized Raman spectroscopy and simulation was first tested by studying the orientation of TTF molecules in TTF crystal. Then, the same analysis was applied to the single Au-TTF nanowire. The results of angular polarization Raman measurements and the simulation of depolarization ratio demonstrated the tilted stacking of TTF units in single Au-TTF nanowire along the long axis. This is the first study on molecular orientation of metal-organic charge-transfer nanowires via polarized Raman spectroscopy. In this part, the objective of characterizing and understanding wire structures was achieved.

3) The formation of fibres and particles made of metal salts and derivatives of TTF in a microfluidic device and in a conventional reaction flask was comparatively investigated. Their morphologies, optical properties and electrical conductivities were characterized. A series of uniform 1D structures were successfully formed via charge-transfer interactions at the interface of two laminar streams in the microdevice. The reaction occurred between metal and different TTF derivatives indicated that the high planarity and strong molecular interaction of TTF derivatives are beneficial to the formation of nanowires. This

study provided a comprehensive overview of the morphologies of the products obtained from reactions between metals and different commercially available TTF derivatives such as TTF, formyl-TTF (FTTF), and BEDT-TTF. In this subproject, the aims of finding suitable materials for nanowire sensors, characterizing and understanding the structure were achieved.

4) The synthesis based on another organic ligand TCNQ was addressed. The microfluidic-assisted synthesis of Cu-TCNQ nanostructures at ambient environment is reported for the first time. A two-layer microfluidic device comprising parallel actuated microchambers was used for the synthesis, and enabled an excellent fluid handling for continuous and multiple chemical reactions in confined ultra-small chambers. The localized synthesis of copper and *in situ* transformation to Cu-TCNQ wires in solution was achieved by applying different gas pressures in the control layer. The as-prepared Cu-TCNQ wire bundles showed good electrical conductivity and hysteresis reversing memory effect, which proved the possibility of using them to fabricate advanced nanoelectronic components. In this subproject, the aims of locally synthesizing of wires, and formation of suitable materials for potential sensing applications were achieved.

The outline of this thesis is as follows: the thesis is divided into 6 Chapters, in Chapter 1 (Introduction), a general introduction to the research is presented: concepts of electron donor and acceptor molecules (Chapter 1.1), metal-organic charge-transfer complexes (Chapter 1.2), one-dimensional nanostructures (Chapter 1.3) are illustrated. The scope of thesis is introduced in Chapter 1.4. Microfluidic technology is described in Chapter 2, which includes an introduction to microfluidics (Chapter 2.1), microfluidic-guided synthesis (Chapter 2.2) and microfluidic-assisted applications (Chapter 2.3) of nano-/microwires, and microfabrication (Chapter 2.4). The experimental techniques used in this work are described in Chapters 3, including optical techniques (Raman spectroscopy in Chapter 3.1) and electrical techniques (Chapter 3.2). The detailed sample preparation and characterization including materials, microchip operation, preparation of solutions and characterization techniques are described in Chapter 4. Results are discussed in Chapter 5 in four parts. In the first part, Chapter 5.1, label-free biosensors based on *in situ* formed and functionalized microwires in microfluidic devices are discussed. In Chapter 5.2, the study of molecular self-organization in single TTF crystal and individual Au-TTF nano-/microwire by polarized confocal Raman spectroscopy is discussed. In Chapter 5.3, a comprehensive overview of the morphologies of the products obtained from reactions of metal salts and TTF and TTF derivative are

discussed. In Chapter 5.4, the synthesis and electric properties of Cu-TCNQ which are based on a different organic ligand are described. Chapter 6 contains conclusion and the outlook based on this project. Finally, molecular structures of the main chemicals used for this work, as well as the materials and details on suppliers are reported in Appendix.

2 Methods-1: Microfluidics and microfabrication

2.1 Introduction to microfluidics

Microfluidic systems refer to miniaturized systems in micrometre (μm) dimensions. Miniaturization of analytical systems for chemical and biological applications has attracted great attention in the past decades. The first micrometre-sized device was fabricated in the 1970s,⁷¹ and used as a miniaturized gas chromatograph. After the introduction and great development of micro total analysis systems (μTAS) in the 1990s,⁷² an increasing research interest has emerged in this field worldwide, with a growing number of publications on device fabrication and applications. Microfluidics involves two aspects, on one hand the miniaturized system with dimensions of tens to hundreds of micrometres, and on the other hand the technology in manipulating small volumes (from nanolitre (10^{-9} L) to attolitre (10^{-18} L) range) of fluids with this system.⁷³ Since the miniaturized “lab-on-a-chip” device enables the manipulation of ultra-small volumes, it offers obvious advantages over conventional devices. A most important effect is that in microfluidics, viscous forces are stronger than inertial forces, leading to the absence of turbulences, i.e. laminar flow. Whether the flow of liquid is laminar or turbulent, can be described by the Reynolds number (Equation 2.1), which is an important dimensionless parameter in fluid mechanics,

$$Re = \frac{v\rho l}{\mu} = \frac{\text{inertial forces}}{\text{viscous forces}} \quad (2.1)$$

with flow velocity v , density ρ , length scale l and dynamic viscosity of the fluid μ . For the flow at low Reynolds numbers (less than 2000), the viscous forces dominate the fluid properties in microchannel, and the liquid flow is laminar. The transition between laminar and turbulent is in the range of 2000-3000,⁷⁴ when Reynolds number is larger than 3000, inertial forces are dominant, resulting in a typical turbulent flow behaviour. The Reynolds number of microfluidic systems is typically in the range of less than 10, indicating the laminar flow behaviour in microfluidic devices. If two reactant solutions flow into one channel and the flow is laminar, a stable interface between two reactive

streams can be established, and the mixture of the solutions will be determined by diffusion. Therefore, the reaction will take place preferentially at the interface of the reactant solutions. Since reaction is determined by both the length of the channel and the flow rates, tuning of reaction times inside a microfluidic system is possible by controlling the flow rates of solutions, and this can be an advantage for fast chemical reactions.

For the substrate of microfluidics, it was firstly performed on etched and bonded silicon and glass, which required a clean room environment and thus was limited in use because of the high fabrication cost. In the year 1998, Duffy *et al.* introduced the soft lithography technology for microfluidics fabrication and use polymers such as poly(dimethylsiloxane) (PDMS) to replicate microstructures from silicon wafers in normal laboratories.⁷⁵ Since only silicon wafers need to be prepared in clean room, soft lithography became an important technique in making microchips due to advantages such as low cost, ease of fabrication and rapid prototyping. After further development of monolithic micro-fabricated valves and pumps by multilayer soft lithography in 2000 by Unger *et al.*,⁷⁶ microchips based on soft lithography fabrication turned to be an more advanced technology.

In general, microfluidics offers various benefits for different research fields. Miniaturized systems are very promising and efficient in cell analysis, due to the ultra-small size. Apart from the easyhandling of fluids, the use of microfluidic reactors for chemical processes offers several advantages. The decreased sample consumption can be advantageous for the generation and screening of huge compound libraries, but also allows to reduce the costs of expensive biological samples and the volume of generated chemical wastes, with a great benefit for environment. Combined with increasing number of advanced microchip devices, microfluidics technique has become more and more important with growing applications in many different subjects and modern analytical fields, such as chemistry,^{77,78} biology,^{79,80} material sciences,^{81,82} drug discovery,⁸³ and cell analysis.^{84,85}

2.2 Microfluidic-guided synthesis of nano-/microwires

In the past couple of years, much effort has been focused on the development of new techniques to produce uniform nanowires using top-down (lithography) and bottom-up (self-assembly) approaches.⁸⁶⁻⁸⁸ For bottom-up processes, a variety of solution-based deposition techniques have been developed including

chemical synthetic approaches, self-assembled monolayers, Langmuir-Blodgett films, electrochemical methods, *etc.*^{89,90} Although these techniques made much progress in the fabrication of nanowires, it is still challenging to obtain uniform wires, to control and guide the assembly of structures at the nanoscale.

In recent years, microfluidics techniques have been demonstrated to be an attractive approach for fabricating micro- and nanostructures due to the excellent properties when scaling-down the dimensions of a system. It can offer numerous benefits, e.g. laminar flow, reduced sample/reagent consumption, fast analysis and separation.^{91,92} Compared to conventional large-scale methods, microfluidic systems provide unique advantages in precise fluid handling and metering, which enable spatial localization of small reagent volumes in microchannels.⁹²⁻⁹⁵ In particular, under the non-turbulent laminar flow conditions, a stable interface between two co-flowing streams can be established. In this case, reaction and structure assembly will directly take place at the interface and the diffusion zone of the reactants (Figure 2.1).^{91,96} In addition, microfluidics facilitates the reproducible and well-controlled supply of reagents, leading to the formation of high-quality homogeneous micro- and nanostructures. Hence, microfluidics is considered as an advanced tool for forming low scale structures and many new microfluidic devices have been presented in recent years for these purposes. Thus, different microfluidics devices were also applied for the synthesis of nano-/microstructures in this project.

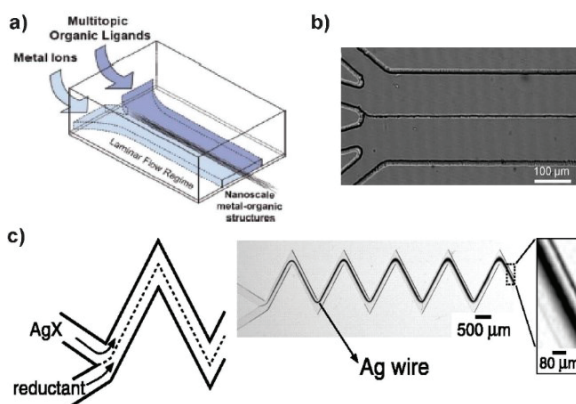


Figure 2.1. Microfluidic synthesis based on continuous laminar flow. a) Schematic illustration of the fabrication of 1D coordination polymer nanostructures using laminar

flow in a microfluidic platform. b) Optical microscope image showing the guided assembly of 1D nanostructure bundles created at the interface between aqueous Ag(I) metal ions and cysteine solutions. Scale bar: 100 μm . c) Optical micrograph of a silver wire deposited in a zigzag channel at the laminar flow interface between solutions containing the components of an electroless silver plating solution. Scale bar is 500 μm and 80 μm for the low and high magnification of channel. Figures a) and b) were reprinted with permission from (Puigmartí-Luis, J.; Rubio-Martínez, M.; Hartfelder, U.; Imaz, I.; Maspoch, D.; Dittrich, P. S. Coordination Polymer Nanofibers Generated by Microfluidic Synthesis, *Journal of the American Chemical Society* **2011**, 133, 4216-4219).⁵⁸ Copyright (2011) American Chemical Society. Figure c) was reprinted with permission from (Science 1999, 285, 83-85).⁹¹ Copyright (1999) The American Association for the Advancement of Science.

Furthermore, microfluidics systems can be integrated with pneumatically actuated valves^{29,97-100} that can create micrometre-sized reaction chambers inside the channels. This is particularly useful to handle ultra-small amount of liquids and to enable the chemical reactions in confined chambers. The valves can have a round shape like a “donut” or a line shape, depending on various applications. A typical “donut”-shaped valve shown in Figure 2.2a was firstly developed to realize the on-chip immobilization of small particles and used to obtain different lengths of metal-organic wires. Another two-valve microchip design was developed based on the “donut” valve for single cells trapping and analysis.¹⁰¹ Linear gas control was used to control solution supply, usually in a parallel way (Figure 2.2 b). A microchamber array composed of ten parallel microchambers was controlled by three gas control channels. By applying different pressure to different channels, the solution supply is controlled to allow the reaction in the confined microchambers.²⁸ These static micrometre-sized reactors can be designed in a highly parallel way and used for biochemical and chemical reactions.⁷⁶

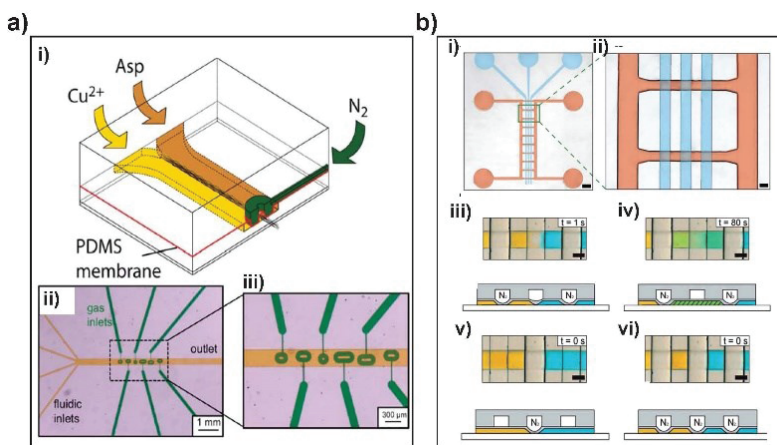


Figure 2.2. Microfluidic devices with valves. a) Microfluidic device with donut shape valve. i) Schematic illustration depicting the principle of wire trapping. The bottom fluidic layer is used for nanowire formation when co-flowing the reactant solutions and the top layer is the control layer that can be pressurized by N_2 gas. Donut-like features and N_2 gas supply channels are impressed into this layer. A flexible PDMS membrane separates both layers. Wires formed at the interface can be selectively immobilized by pressurizing the donut, thereby defining the length of the trapped nanowires. ii) Micrograph of the device. The channels in the fluid layer and the control layer are filled with food dye. Scale bar: 1 mm. iii) Magnification of the donut features. Scale bar: 300 μm . Figures are adapted from Reference 29 with permission from The Royal Society of Chemistry. b) Microfluidic device with linear valve and multi-chamber arrays. i) Micrograph of the multilayer PDMS chip with an array of 10 parallel microchambers in the fluid layer (red channels, 10 μm high). Fluid metering and supply is controlled by three pneumatically actuated valves (control layer, blue channels, 100 μm high). Scale bar: 750 μm . ii) Magnification of two microchambers. The final microchambers are confined by the two side valves and encapsulate a volume of 675 pL. Scale bar: 150 μm . iii-vi) Series of micrographs showing the operation of the valves and the diffusive mixing of two food dyes in a typical reaction procedure, corresponding schematic side views are shown on the bottom of each figure. iii) Introduction of the reagents, iv) Compartmentalization of two reagent volumes on either side, v) opening of the central valve, and vi) diffusive mixing. Scale bars: 100 μm . Reprinted with permission from (Cvetkovic, B. Z.; Puigmarti-Luis, J.; Schaffhauser, D.; Ryll, T.; Schmid, S.; Dittrich, P. S. Confined Synthesis and Integration of Functional Materials in Sub-nanoliter Volumes, *ACS Nano* 2013, 7, 183-190).²⁸ Copyright (2013) American Chemical Society.

2.3 Microfluidic-assisted application of nano-/microwires

For applications in nanoelectronics, nanostructures must be not only synthesized, but also positioned and integrated with electrodes. On one hand, these multiple-steps can be done separately, that is, by aligning pre-synthesized nanostructures onto microchip devices for analysis. For example, a single-walled carbon nanotube (SWNT) prepared by chemical-vapour-deposition growth was aligned to a PDMS microchip and connected to Pd/Au source and drain contacts. Because a microchip can be used as a microdevice with a delivering system for further reactions on the nanowires formed/trapped inside the microchip. This SWNT transistors was successfully used to sense the local potential generated by a fluidic flow of ionic solutions on charged surfaces.¹⁰² On the other hand, the synthesis and application can be in principle totally performed in one microfluidic device. To achieve this goal, a microchip with prefabricated microelectrodes is needed.⁹⁸ Together with the localized formation of structures, direct analysis of electronical characteristics of conductive nanostructures is possible, without further complicated manipulation (Figure 2.3).

Thus, features as the ease of fabrication, laminar flow, elimination of local variation, control of reaction times by diffusion and total integrated system make microfluidics systems very attractive and promising for synthesis and analysis of nanoscale structures. Therefore, a huge effort has been made worldwide in order to explore the appealing features that microfluidics offers for the formation and analysis of various micro and nanoscale structures and devices.

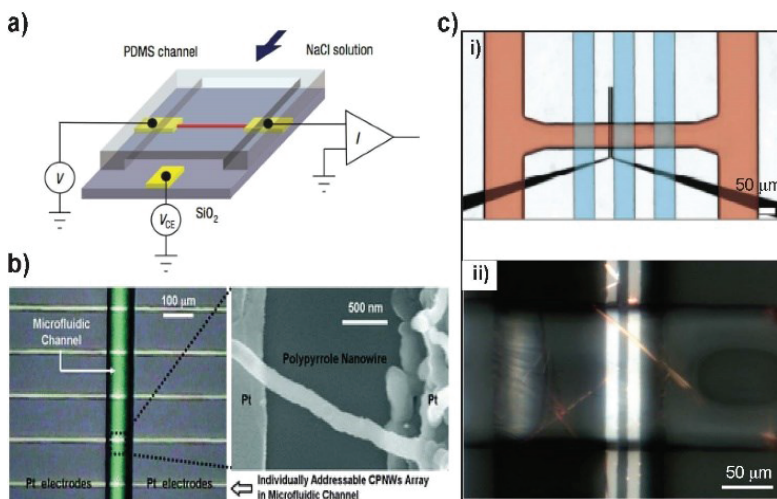


Figure 2.3. Microfluidic-assisted application of conductive nanostructures. a) Schematic diagram of a nanotube-based flow sensor showing a nanotube integrated with source, drain and counter electrodes. The device is covered by a PDMS membrane with a micro-fabricated channel. The channel is placed over the device and liquid is caused to flow through it. Figure was adapted from Reference 102 with permission from Nature Publishing Group. b) Optical image of the electrochemical fabrication of conducting polymer nanowires in the microfluidic channel (left) and the SEM image showing the nanowire grown in the channel on top of the pre-existing Pt electrodes. Figure adapted from Reference 98. c) i) Scheme showing a microchamber integrated with prefabricated electrodes. ii) Polarized micrograph of Au-TTF wires formed inside a microreactor chamber, showing the alignment of the wire on top of the microelectrodes. Scale bars: 50 μm . Reprinted with permission from (Cvetkovic, B. Z.; Puigmarti-Luis, J.; Schaffhauser, D.; Ryll, T.; Schmid, S.; Dittrich, P. S. Confined Synthesis and Integration of Functional Materials in Sub-nanoliter Volumes, ACS Nano 2013, 7, 183-190).²⁸ Copyright (2013) American Chemical Society.

Reported studies have shown the possibilities of using microfluidics to form metal nanowires,⁹¹ metal-(bio)organic nanostructures,⁵⁸ polymer fibres,⁹⁸ *etc.*, as well as to develop microfluidic-synthesized nano-/microstructures for sensors and nanoelectronics.

2.4 Microfabrication

Before the fabrication of a microchip, the first step is the development of a microchip design for the specific application. The microchip design is prepared as a schematic drawing showing the specific microchip properties, with the help of a computer-aided design (CAD) software. Secondly, this CAD drawing has to be transferred onto a film mask. Afterwards, the micropatterns on the film mask are transferred into a photosensitive polymer (photoresist) to form a mold by photolithography. Finally, the microchip is fabricated by soft lithography using PDMS and bonded to a glass slide to form the final device. The introductory knowledge on the fabrication of silicon wafers, masters, glass slide with microelectrodes is shown in Chapter 2.4.1. The mechanism of soft lithography is explained in Chapter 2.4.2, followed by the detailed description of the microchip preparation protocols applied in this work (Chapter 2.4.3).

2.4.1 Wafers and masters

a) Silicon wafers

Nowadays, silicon wafers used for building microfluidic devices are predominantly fabricated by photolithography, due to its possibility to prepare structures down to sub-micron size. Photolithography is a technique to transfer a structure from a photomask to photoresist using light, e.g. UV light at 365 nm or 405 nm. In general, depending on the working mechanism of photoresists, two different behaviours can be observed upon UV-irradiation. A negative photoresist e.g. SU-8, the illuminated areas polymerize when exposed to UV light, whereas for a positive photoresist, e.g. AZ 9260, the non-exposed areas polymerize. These two different photoresist are used for the fabrication of different channels, for rectangular channels SU-8 is used, while for round channels the AZ resistant is applied. Depending on the photoresist used for wafer fabrication, different photomasks are applied. For negative resist SU-8, a dark field mask is prepared because features in white will result in a structure (Figures 2.4a and 2.4c). In contrast, for positive resist AZ, bright field mask will be used since features in black generate the structures (Figures 2.4b and 2.4 d).

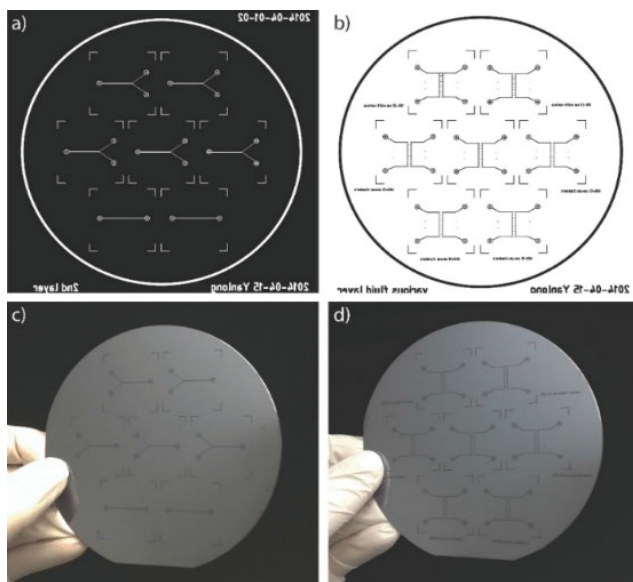
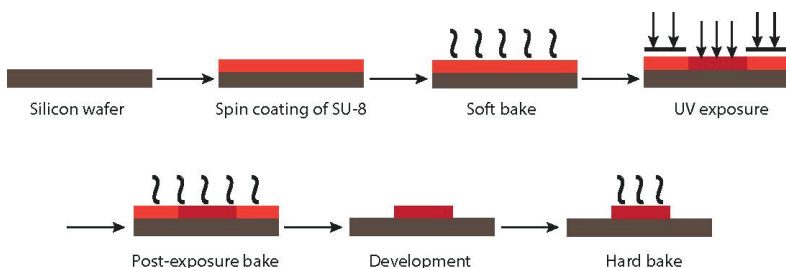


Figure 2.4. Images of chrome masks and wafers used in this thesis. Test plot images of a) SU-8 dark field chrome mask and b) AZ bright field chrome mask. Photographs of 4-inch wafers of c) SU-8 produced from a) and d) AZ fabricated from b). Note: mirror images of wafers are shown in test plots.

b) SU-8 silicon masters

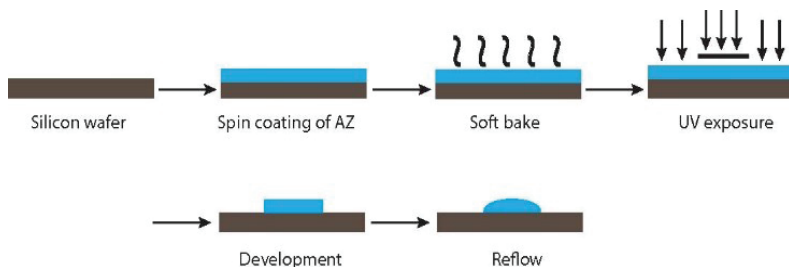
To fabricate the master forms for preparing microchip layers, a 4-inch silicon wafer is first spin-coated with SU-8 photoresist and soft baked. The microchip features are transferred from the silicon wafer onto SU-8 by the use of photomask and UV-light exposure. After the post-exposure baking step, the non-exposed SU-8 is developed and hard-baked to get the final device. All master forms were silanized overnight under vacuum using 1H,1H,2H,2H-perfluorodecyl-dimethylchlorosilane in order to avoid PDMS adhesion during chip fabrication. For the fabrication of different master molds with various heights, different types of SU-8 photoresists with their own process parameters can be applied. An introductive schematic illustration is shown in Scheme 2.1. Details on the fabrication method can be found in literature.¹⁰³



Scheme 2.1. Schematic of the microfabrication steps of a SU-8 master mold. Scheme reproduced from Reference 103.

c) AZ silicon masters

For the fabrication of pneumatic actuated valves, round-shaped fluidic channels are needed. The master mold for the liquid channel was prepared using a 4-inch silicon wafer. A silicon wafer was first spin-coated with AZ photoresist and soft baked. The desired microchip features were transferred onto AZ using a photomask and UV-light exposure. After the development of the non-exposed AZ, a reflow procedure was performed to get the final device. An introductory schematic illustration is shown in Scheme 2.2. More details on the fabrication method can be found in literature.¹⁰³



Scheme 2.2. Schematic of the microfabrication steps of an AZ master mold. Scheme reproduced from Reference 103.

d) Glass slide with microelectrodes

For electrical characterization of conductive wires, platinum (Pt) patterned microelectrodes were fabricated on top of glass coverslips (24×40 mm, No. 5, Menzel Gläser) by conventional photolithography and physical vapour deposition. A detailed description of the fabrication method is reported elsewhere.^{28,103}

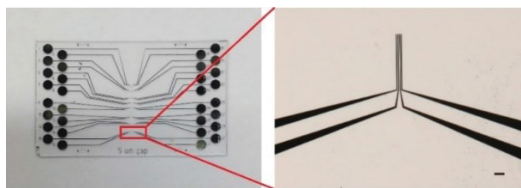


Figure 2.5. A photograph of a glass slide with microelectrodes (left, used in the experiments reported in Chapter 5.3 and Chapter 5.4. Details of the four-point microelectrodes under optical microscope are shown in the right image (Scale bar: 50 μm).

2.4.2 Soft lithography

Soft lithography refers to the technique that involves an elastomer as the mask, stamp, or mold.¹⁰⁴ It is a widely used to fabricate microfluidic devices. Nowadays, the most popular elastomeric material for microchips is the commercially available PDMS, because of its useful properties including low cost, low toxicity, high biocompatibility, chemical inertness, mechanical flexibility and durability, as well as the ease in fabrication. PDMS consists of two components, an oligomer (elastomer) base and a curing agent (Pt catalyst). In the oligomer base, there exist vinyl group-terminated siloxane oligomers and cross-linking oligomers (Figure 2.6). The curing agent is composed of Pt-based catalyst that can catalyse the cross-linking reaction. To produce a PDMS-based microchip, the two gels are mixed (Figure 2.6). In addition, the hardness of the PDMS microchip can be controlled by using different weight ratio of the components (PDMS oligomer: Curing agent, 5:1-20:1). If the ratio of curing agent is increased, higher cross-linking reaction will result in a harder PDMS microchip, while a lower ratio of curing agent will form softer microchip.^{103,105}

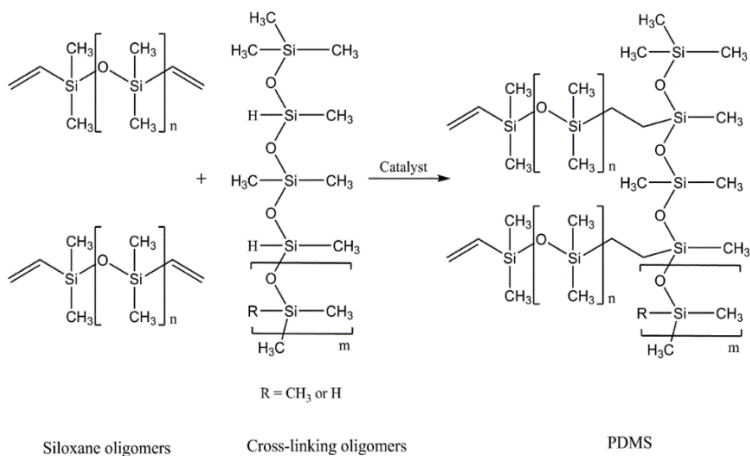


Figure 2.6. The formation of PDMS by catalytic cross-linking reaction. Catalytic formation of PDMS with the addition of the Si-H bond (cross-linking copolymer) to the vinyl groups (siloxane oligomer), forming Si-CH₂-CH₂-Si linkages. The multiple reaction sites on both the base and cross-linking oligomers allow for three dimensional cross-linking. Figure reproduced from Ref. 103.

2.4.3 Microchip fabrication

All microchips used in this work were fabricated by soft lithography, introduced in Chapter 2.4.2. The microchannel features imprinted in the PDMS layer need to be sealed with a glass slide to get the final microfluidic device. In most cases, a strong permanent bonding between the PDMS layer and glass slide is required, in order to use high pressure to pump liquid into the microchannel. Thus, an oxygen plasma is applied to activate the surfaces for bonding. However, when the structures formed inside the microchannel are positioned and needed for further characterization, a non-bonded microchip is used, where the PDMS layer and glass slide are hold together in a custom-made clamping device. The fabrication protocols of one layer and double layer PDMS microchips (Figure 2.7) are reported in the following.

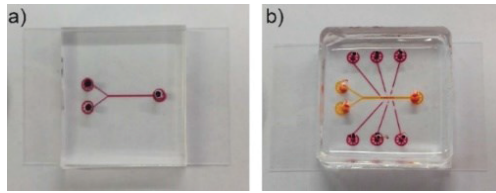


Figure 2.7. Photographs of two microchips used in this project. a) A one layer microchip filled with dark red food dye and b) A double-layer microchip filled with food dyes to show the different layers, top layer in dark red and bottom layer in orange.

a) Single layer microchip fabrication

For preparation of a microchip layer in this project, PDMS oligomer and curing agent were mixed at a ratio of 10:1, degassed, poured onto the wafer bearing the respective features and degassed again, then heated in oven at 80 °C for 3 h. After this, the layer was removed from the wafer and holes were punched with a biopsy puncher (1.5 mm diameter, Miltex, York PA). Afterwards, the PDMS layer and a cleaned glass slide (Thermo Scientific, Menzel-Gläser, Nr. 3) were treated in oxygen plasma, and then carefully aligned and bonded together. Finally, the bonded chip was heated at 90 °C for 30 min to confirm the permanent bonding.

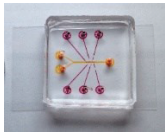
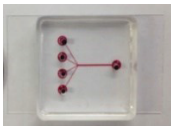
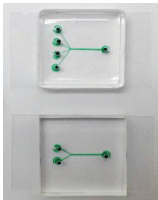
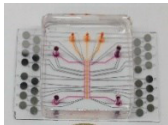
b) Double layer microchip fabrication

For the multilayer microfluidic chip, layers were prepared separately by casting PDMS from the respective master forms. Alignment, assembly and bonding of both layers resulted in the final device. For preparation of the control layer, PDMS oligomer and curing agent were mixed at a ratio of 10:1, degassed, poured onto the control layer wafer and degassed again, then heated in oven at 80°C for 3 h. After this, the layer was removed from the wafer and holes were punched with a biopsy puncher (1 mm diameter, Miltex, York PA). For the fluid layer, softer PDMS (mixing ratio elastomer: curing agent of 15:1) was spin-coated at 2000 rpm on the structured four-inch fluidic master mold wafer to create a 23 μm -high membrane, and then the wafer was heated at 80 °C for 1 h. Both layers were activated in oxygen plasma using a plasma cleaner (PDC-32G plasma cleaner, Harrick Plasma, power 18 W, time 45 s) and afterwards aligned under a Multizoom AZ100M microscope (Nikon Corporation, Switzerland). The assembly was cured for 2 h at 80°C to form a permanent bond between both

layers. Afterwards, the device was removed from the master form and access holes for the tubing (1.5 mm diameter, Miltex) were punched. The assembled chip and a clean glass slide (Thermo Scientific, Menzel-Gläser, Nr. 1) were treated in oxygen plasma, and then carefully aligned and bonded together. Finally, permanent bonding was achieved by heating the well-assembled chip was heated at 90 °C for 30 min.

Both single layer and double layer microchips were used in this project. Table 2.1 shows an overview of the microchips used in this work, as well as their applications. Detailed microchip features can be found in separate Chapters.

Table 2.1. An overview of the microdevices used in different Chapters of this work.

Chapter	Topic	Microdevices	Function
5.1	Label-free biosensors based on <i>in situ</i> formed and functionalized microwires in microfluidic devices		Synthesis of Au-TTF microwire; Development of sensors
5.2	Study of molecular self-organization in individual Au-TTF nano-/microwire by polarized confocal Raman spectroscopy		Synthesis of Au-TTF nano-/microwires
5.3	Conductive single nanowires formed and analysed on microfluidic devices		Synthesis of metal-TTF (and derivatives)
5.4	Localized synthesis of conductive Cu-TCNQ nanostructures in ultra-small microchambers for nanoelectronics		Synthesis of Cu-TCNQ; Conductivity measurement

3 Methods-2: Raman microspectroscopy

Raman spectroscopy is a non-destructive optical technique which can be applied to study the molecular vibrations of diverse materials on solid (such as metal and semiconductors) at interfaces of solid-liquid, in liquid, and in complicated bio-samples *etc.*¹⁰⁶⁻¹⁰⁸ Thus, in this project, Raman spectroscopy was the main optical technique used for monitoring vibrational changes of molecules absorbed on nanostructures (Chapter 5.1) in liquids and also the molecules inside nanostructures (Chapter 5.2). Following, an introduction of Raman scattering (including Stokes, anti-Stokes and resonance Raman scattering, Raman spectroscopy and fingerprint, Raman and Infrared (IR) spectroscopy), theoretical basis of Raman scattering (including normal modes, selection rules, Raman tensor) and confocal and polarized Raman microspectroscopy (principle and setup) is presented.

3.1 Raman scattering

3.1.1 Stokes, anti-Stokes and resonance Raman scattering

When an incident electromagnetic radiation encounters a molecule, it can be absorbed by the molecule if the energy of the incoming photon matches the energy difference between the ground state and the excited state of the molecule. However, in most cases the incoming radiation does not match any molecular transition. Alternatively, the photons are scattered from the molecule. Most photons are elastically scattered. They have the same energy as the incoming photons. This elastic scattering process is called Rayleigh scattering. In a few cases, photons are inelastically scattered and energy is exchanged between photons and molecules. This means that the molecule changes its vibrational state upon interaction with the incoming photon, resulting in changes in the energy or frequency of the scattered photons. This inelastic scattering effect is termed Raman scattering. Apart from scattering at vibrations also other elementary excitations may be involved, which however is not relevant here.

Raman scattering requires monochromatic irradiation for exciting molecular vibrations. After inelastic scattering, a portion of the incident photons is scattered inelastically. Thus, the energy of the scattered photons ($h\nu_R$) differs

from that of the incident photons ($h\nu_0$). According to the law of conservation of energy, the energy difference corresponds to the energy change of the molecule, and refers to the transition between two vibrational states.¹⁰⁹ If the molecule changes from a ground state to an excited vibrational state after scattering, this means the molecule absorbs energy from incoming photons and the scattered photons possess less energy than that of incident photon ($h\nu_R < h\nu_0$). This scattering is called Stokes Raman scattering. Conversely, when a molecule relaxed from an initial excited state to to ground state, the energy of the scattered photons is higher than incident photons ($h\nu_R > h\nu_0$). This scattering is known as anti-Stokes Raman scattering. For an anti-Stokes process to take place, the molecule must be in an excited vibrational state, which requires thermal excitation. According to the equilibrium on temperature (T) of Boltzmann factor: $\exp(-E/K_B T)$ (K_B is constant of distribution), the higher the energy of the vibration E is, the intensity of the scattering peaks becomes exponentially weaker. Thus, anti-Stokes Raman scattering is weaker than the Stokes scattering process.¹⁰⁶ The Jablonski diagrams in Figure 3.1 illustrates the energy changes in Rayleigh, non-resonance (Stokes and anti-Stokes) and resonance Raman scattering processes.

The initial excited state of a molecule in Raman scattering is also known as a virtual state. In quantum physics, a virtual state is short-lived, unobservable, intermediate quantum state. In a special case, if the virtual state coincides with a real electronic state of the molecule (for example excited state S_1 , Figure 3.1), the scattering process is resonant. Resonant Raman scattering has important implications for both the magnitude and the selection rules of the effect in Raman scattering.¹⁰⁶

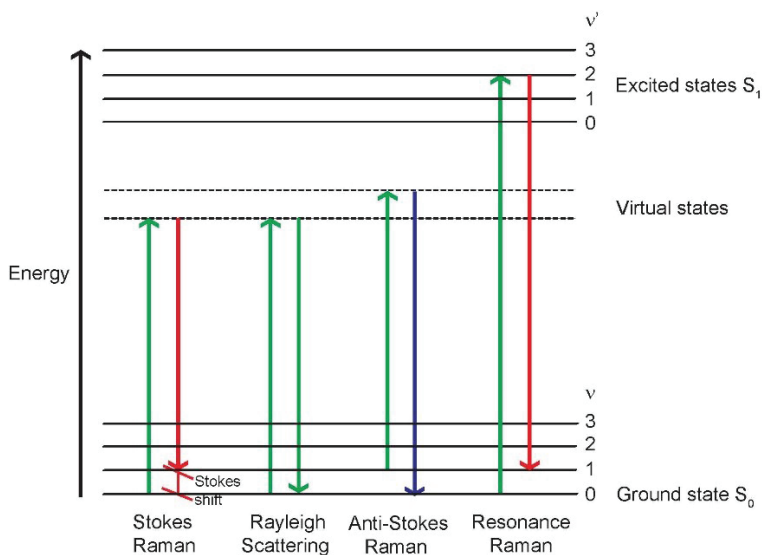


Figure 3.1. Simplified Jablonski diagrams of light scattering. Schematic illustration of Rayleigh scattering, non-resonance Raman scattering (Stokes and anti-Stokes) and resonance Raman scattering processes.

3.1.2 Raman spectroscopy and fingerprint

The energy lost by the photons in the scattering event is called the Raman shift and is defined in energy as $(h\nu_0 - h\nu_R)$. It is therefore positive for a Stokes and negative for an anti-Stokes process. Raman shifts are commonly expressed in wavenumbers (cm^{-1}), with the frequencies corresponding to particular vibrational modes of molecules. A Raman spectrum corresponds to the wavelength- (or energy) dependence of the Raman scattered intensity at a given incident wavelength.¹⁰⁶ It provides information by which molecules can be identified. As mentioned above, the Stokes Raman intensity is higher than anti-Stokes Raman intensity. So the normal Raman scattering refers to Stokes Raman scattering. The Raman shift in Stokes Raman scattering is called Stokes Raman shift, which is very useful to identify molecular vibrational states. Typically, the frequency range from 400 cm^{-1} to 1500 cm^{-1} is known as the fingerprint region for identifying molecules. Raman spectroscopy is the spectroscopic technique based on measurement and analysis of the signals arising from the Raman effect.

It is recognized as a non-invasive optical technique which can provide detailed molecular information on the measured samples.^{110,111} It enables the direct detection of molecules by analysing the fingerprints in their separate Raman spectrum. Thus, Raman spectroscopy has general and wide applications in various (bio-)chemistry fields including analytical chemistry, material science, biosciences, pharmaceutical studies, *etc.*¹⁰⁶

In thermodynamic equilibrium, the excited state is less populated than the ground state. Therefore, the rate of transitions from the ground state to the excited state (Stokes) will be higher than that in the opposite direction (anti-Stokes). Thus, the ratio of Raman intensities ($I_{\text{Stokes}}/I_{\text{anti-Stokes}}$) highly depends on the temperature, which is a useful tool for temperature-dependent measurements in solid-state physics. Figure 3.2 shows an example of the Raman spectrum of TCNQ. The peak positions of Stokes and anti-Stokes Raman scattering are symmetric around Rayleigh scattering ($\Delta\nu=0$) because they correspond to the energy changes between the same excited and ground resonant states. However, the Raman intensities are temperature dependent, with Stokes scattering peaks much stronger than anti-Stokes scattering peaks.

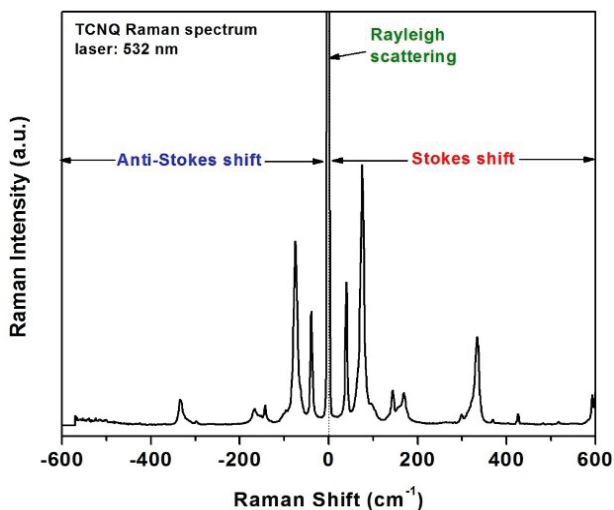


Figure 3.2. Raman spectrum of TCNQ under laser excitation of 532 nm. Rayleigh scattering ($\Delta\nu = 0$) in the middle, with symmetric spectrum of Stokes (red) and anti-Stokes (blue) shift. The dash line indicates the position where $\Delta\nu$ is 0.

3.1.3 Raman and Infrared spectroscopy

Molecular vibrations can be excited not only by the inelastic scattering of photons (Raman scattering), but also by the absorption of light quanta. When a polychromatic light irradiates molecules, if the light energy ($h\nu_0'$) matches the energy difference ($h\nu_k$) between the ground state ($h\nu_i$) and a vibrational state ($h\nu_j$) of the molecule, direct absorption of photons is achieved (Equation 3.1).

$$h\nu_0' \sim h\nu_k = h\nu_j - h\nu_i \quad (3.1)$$

As these energy differences are in the order of 0.5 and 0.005 eV, light with wavelengths longer than 2.5 μm (IR light) is sufficient to induce the vibrational transitions. Thus, vibrational spectroscopy that is based on the direct absorption of light quanta is defined as IR absorption.¹⁰⁹ The absorption of incoming light in the infrared region results in a spectrum that corresponds to specific vibrational modes in molecules measured. Raman and IR spectroscopy are both optical techniques based on the changes in molecular vibration, showing unique fingerprint of the molecule separately. The modes appearing in the Raman and IR spectra are different, however, the two techniques provide complementary information of the vibrational structure of molecules.¹⁰⁹ In this work, IR spectroscopy was also applied for the characterization of metal-organic compounds (see Chapters 5.3 and 5.4).

3.2 Theoretical basis of Raman scattering

3.2.1 Normal modes

In the Cartesian coordinate system, each atom in a molecule can be displaced in the x-, y- and z-directions, corresponding to three degrees of freedom.¹¹² A molecule of N atoms has in total 3N degrees of freedom. However, not all of them correspond to vibrational degrees of freedom. If all atoms are displaced in the x-, y-, and z-directions by the same increments, the entire molecule moves in a certain direction, representing one of the three translational degrees of freedom. The same with displacements of the atoms that correspond to rotation of the molecule: a nonlinear molecule has three rotational degrees of freedom, while a linear molecule has two. Thus, the remaining 3N-6 and 3N-5 degrees of freedom correspond to the vibrations of a nonlinear and a linear molecule, respectively. In molecules, movements of atoms create a vibrational motion, which is known as the normal mode of a molecule. Normal mode analysis shows the characteristics of a certain molecule in the frequencies and molecular properties.¹⁰⁹

3.2.2 Polarizability and Raman selection rules

In a Raman scattering process, the electron cloud of a molecule is distorted from its normal shape by the electric field vector of an incoming electromagnetic wave, which induces an electric dipole moment. The extent of the electron cloud distortion depends on its polarizability, α , which is defined to relate the induced dipole moment μ_{ind} to the electric field E causing it (Equation 3.2)

$$\mu_{ind} = \alpha \cdot E = \alpha \cdot E_0 \cos(2\pi\nu_0 t) \quad (3.2)$$

where E_0 is the amplitude and ν_0 is the frequency of the electric field component of the incoming magnetic wave that produces the dipole moment.¹¹³⁻¹¹⁵ The polarizability α is actually a tensor changing over time, and describes the response of the electron distribution to the movements of the nuclei that oscillate with the normal vibration. In the simplest case of a diatomic molecule (harmonic oscillator) vibrating with a frequency ν_k , the nuclear displacement Q_k is as follows (Equation 3.3):

$$Q_k = Q_0 \cos(2\pi\nu_k t) \quad (3.3)$$

where Q_0 is the amplitude (maximum displacement) of the molecular vibration. For small amplitudes of the molecular vibration, α can be approximated by a function of Q_k (Equation 3.4):

$$\alpha = \alpha_0 + \left(\frac{\partial \alpha}{\partial Q_k} \right)_0 Q_k \quad (3.4)$$

Here α_0 refers to the polarizability at equilibrium position, and $(\partial\alpha/\partial Q_k)_0$ refers to the derivative of polarizability α with respect to the change in Q_k , evaluated at the equilibrium position. Combining Equations. 3.2 and 3.4, the general expression for the induced dipole moment μ_{ind} can be written as follows (Equation 3.5):

$$\mu_{ind} = E_0 \left\{ \alpha_0 \cos(2\pi\nu_0 t) + \left(\frac{\partial \alpha}{\partial Q_k} \right)_0 Q_0 \cos[2\pi(\nu_0 + \nu_k)t] + \left(\frac{\partial \alpha}{\partial Q_k} \right)_0 Q_0 \cos[2\pi(\nu_0 - \nu_k)t] \right\} \quad (3.5)$$

Equation 3.5 includes three contributions to the scattered radiation appearing as separate terms with ν_0 for the Rayleigh scattering, while $(\nu_0 + \nu_k)$ for anti-Stokes

Raman scattering and $(\nu_0 - \nu_k)$ for Stokes Raman scattering. This equation implies that if the derivative $(\partial\alpha/\partial Q_k)$ is zero, that means the polarizability of molecule does not change during molecular vibration, then it is not Raman active. Thus, Raman scattering can be activated only in the presence of non-zero polarizability derivative with respect to the normal coordinate $(\partial\alpha/\partial Q_k \neq 0)$. This is also known as the gross selection rules for Raman scattering.^{109,115}

3.2.3 Raman tensor

Derived from Equation 3.5, $(\partial\alpha/\partial Q_k)_{0Q_k}$ is the Raman tensor. In general, Raman tensor is a second rank, three dimensional tensor.¹¹⁶ Considering E_i and E_s as the unit vectors of the polarization of the incoming and scattered light, respectively. The Raman scattering intensity I is described as follows (Equation 3.6):¹¹⁷

$$I \propto |E_i \cdot R \cdot E_s|^2 \quad (3.6)$$

where R is the Raman tensor. R is a symmetric tensor and has the same symmetry as the corresponding molecular vibration.¹¹⁶ In real experiment, under certain experimental conditions regarding the incoming and scattered polarization, whether a Raman-active molecular vibration can be observed or not is determined by the Raman scattering intensity (if the resonance Raman scattering is already taken into account). This is specific Raman selection rules. Thus, under different scattering geometries, the symmetry of the Raman tensor and the underlying molecular vibrations can be identified by Raman experiments. Results on Raman tensor calculation of molecules and the polarized Raman measurement are shown in Chapter 5.2.

3.3 Light polarization and depolarization ratio

Light travelling in free space or isotropic medium can be considered as transverse waves, with the electric field vector and magnetic field in directions perpendicular to the direction of wave propagation.¹¹⁸ By using a linear polarizer, the oscillation of these fields can be in a single direction which is termed linear polarization. Conventionally, the orientation of linearly polarized light is defined by the direction of the electric field vector, parallel or vertically polarized.

In Raman measurements, the scattered light is the sum of the parallel component and the perpendicular component. To obtain more information about the Raman

modes of molecules, polarized analysis can be performed by using the vibration and the 90 degree scattering configuration. In this way, the scattered light can be separated into two configurations, with one parallel to the incident polarization and the other one perpendicular to both the incident beam and the incident polarization. In Raman spectroscopy, a concept widely used to quantitative analysis of the sample polarization response is named depolarization ratio P .^{119,120} It is defined as follows (Equation 3.7).¹¹²

$$P = \frac{I_{xy}}{I_{xx}} = \frac{I_{\text{perpendicular}}}{I_{\text{parallel}}} = \frac{I_{\perp}}{I_{\parallel}} \quad (3.7)$$

Here, I_{xy} represents the Raman intensity at the perpendicular (crossed) laser configuration, I_{xx} represents the Raman intensity at the parallel laser configuration.

3.4 Confocal and polarized Raman microscopy: principles and setups

In this work, confocal Raman microscopy was exploited to focus on nano-/microstructures and get their Raman spectra (Chapters 5). In particular, this is beneficial to single wire analysis inside microchip (Chapter 5.1) as all the signals recorded only from the structure, due to the sub-micrometre scale resolution (focus diameter ~400 nm). Polarized confocal Raman measurement was also performed to study the molecular structures of single nano-/microwire (Chapter 5.2). In the following, the principles and experimental setups of confocal and polarized Raman microscopy are introduced.

3.4.1 Confocal Raman microspectroscopy

In the past decades, Raman spectroscopy has been greatly developed in scientific research and real applications, due to the great progress in instrumentation. A macro-Raman spectrometer includes some basic components: a monochromatic light source, i.e. a laser source to excite the samples, a sample area with collection optics, a light dispersing unit (spectrometer) and a detector recording the signal and passing the signal to a computer. In Raman measurements, strong Raleigh scattering needs to be avoided. Thus, modern instrumentation almost universally employ a notch filter to filter out the strong Raleigh scattering light. Also a sensitive CCD detector is used. A macro-Raman spectrometer has only a spatial resolution from 100 μm to 1 mm. To measure even small samples at micro and nanoscale, Raman

spectrometer equipped with a microscope to magnify its spatial resolution is required.

Micro-Raman spectroscopy is very useful to study the vibrational spectra characteristics of very small samples, especially, when combined with confocal microscopy. This can be more powerful and useful technique to study nanoscale samples. With a pinhole added to the conjugate plane of the detection beam path, out-of-focus light is filtered out. The focused laser beam can be calculated with the spot diameter d ($0.61 \lambda/\text{NA}$) (NA, numerical aperture) and focus depth l ($0.89 \lambda/\text{NA}^2$). For example, with a $100\times$ microscope (NA 0.90), a laser wavelength (λ) of 532 nm, the spatial resolution are calculate to be sub-micron range ($d \approx 0.36 \mu\text{m}$, $l \approx 0.58 \mu\text{m}$). Apart from the improved resolution in the lateral plane ($\lambda/2$, down to 200 nm), the advantages of confocal microscopy over conventional microscopy also lie in reduced background signal, and the possibility to perform two dimensional (2D) (surface) and three dimensional (3D) (with depth profiling) Raman mapping on ultra-small samples in order to understand the location and amount of different components. Figure 3.3 is a schematic view of a micro-Raman setup. A microscope objective is added to the system, with the illumination, scattering light collection passing through the microscope objective in a back-scattering mode.

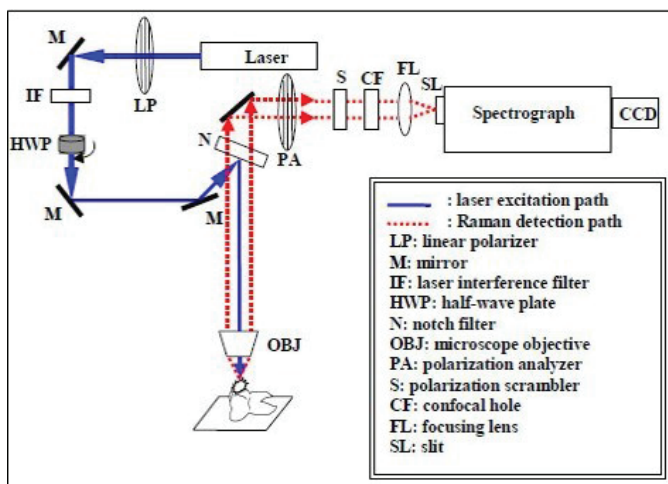


Figure 3.3. Components of a polarized confocal Raman microscope with back-scattering geometry (blue solid lines indicate the incoming light and red dash lines represent back

scattered light from the sample). Note the existence of linear polarizer (LP) after the laser excitation, the polarizer analyser (PA) on the scattered light beam path and the half-wave plate (HWP), which is used for the angular polarization measurement. Figure was adapted from Reference 121 with permission from OSA publishing.

In the present work, mainly confocal Raman microscopy is employed to study nano-/microstructures to obtain normal Raman spectra. In the attempt to achieve increased signal and higher sensitivity of a given sample, a surface-enhanced Raman scattering (SERS) substrate (e.g. Au, Ag) is required. There are a lot of reported work on the application of SERS labels to reach very high sensitivity and low limit of detection of chemical and biomolecules.^{122,123} However, this technique is not used in this work.

3.4.2 Polarized Raman microspectroscopy

During the last years, polarized Raman spectroscopy has been proved to be a very useful approach to determine the orientation of a molecular layer composed of small organic molecules in organic thin layers or single crystals.¹¹² Analysis of the dependence of the Raman scattering intensity upon the angular rotation of the sample around the substrate normal allows the determination of the molecular orientation. The molecular vibrational modes change during the rotation of the sample with a periodicity, suggesting a preferential molecular orientation. Combined with confocal microscopy, the polarized confocal Raman spectroscopy has been employed to study the composition of nano-/micrometre scaled substrate due to its high spatial resolution and non-destructive characteristics.¹²⁴⁻¹²⁶

Polarized Raman measurements are performed using a polarizer that allow passing light of a desired polarization while blocking waves of other polarizations.¹²⁷ To study the nano-/microstructures, a linear polarizer needs to be used to get linear polarized light. Then a polarization analyser inserted in the scattered light beam path between the sample and the spectrometer, allowing the Raman polarization to be selected. In a typical angular polarization experiment of wire structure, the angle between the long axis of the structure and the polarization direction of the incident laser is adjusted using a half-wave plate. A detailed schematic illustration of a polarized confocal Raman microscope can be seen in Figure 3.3.¹²¹

In Raman scattering experiment, Porto's notation is used to indicate the configuration of the scattering¹²⁸, and express the orientation of the crystal with respect to the polarization of the laser in both the excitation and analysing directions. For example, in a light configuration with a back scattering geometry, the direction of the propagation of the scattered light is in the opposite sense of the direction of the incident light, for example X(YZ) \bar{X} . For polarization measurement on samples, normally two configurations are used, parallel and crossed configurations, with the direction of polarized light in a parallel and orthogonal geometry, respectively.¹²⁴ Polarized Raman measurements on a single crystal and a single nanowire are discussed in Chapter 5.2 of this thesis.

3.4.5 *In situ* Raman measurements

For microfluidic-assisted reactions, a confocal Raman microscope allows to detect small samples in a micrometre-scaled microfluidic channel and to gain insight into the reaction occurring in microchips by combining the advantages of both Raman spectroscopy and microfluidics.¹²⁹ This method is known as *in situ* Raman analysis and exploited to obtain a fast signal readout and *in situ* monitoring of ultra-small samples, such as the Au-TTF nanostructures investigated in the present work. The binding of analytes can be identified by changes of the electrical conductivity/resistance (e.g. Chapter 5.3), the identification of the bound molecules on wire surface can be done by changes in Raman response (e.g. Chapter 5.1).

3.5 Instrumentation for Raman spectroscopy

a) Raman spectra of Au-TTF structures in open-donut microchip were recorded on a confocal Raman microscope (CRM 200, WITec GmbH, Germany) (neodymium-doped yttrium aluminium garnet, Nd:YAG laser, 532 nm) using an upright 100 \times objective (Nikon, Japan) with a NA of 0.90. The laser power was 1.4 mW, and the accumulation time was 2 s. In all the measurement, the signals were collected from large Au-TTF wires (diameter \sim 2 μ m) through a relatively small laser point (diameter \sim 400 nm). Raman spectra were recorded from six wires and averaged to represent the Raman results.

b) Raman spectra of metal-TTF nanowires were also obtained on the same Raman microscope as that in a) (λ = 532 nm, 50 \times objective, NA = 0.50). Since the wires are deposited on glass slide and directly applied for Raman measurement in air atmosphere, a lower laser power of 0.37 mW than that of

Au-TTF wires in liquid was used to avoid the heating effect. The accumulation time was 15 s.

c) Raman spectra of Cu-TCNQ were obtained on in-house assembled confocal Raman microscope equipped with a diode-pumped solid-state (DPSS) laser (Cobolt Samba, $\lambda = 532$ nm), a 50 \times Olympus objective (NA = 0.75) and a liquid N₂ cooled CCD as detector. The laser power was 0.4 mW, and the accumulation time was 60 s. A nano-piezo stage (Ratis, Nanoscan Technology) with a minimum scan step of 0.1 nm in the lateral directions was used to move samples during the measurement.

The polarized confocal Raman microscopy analysis of Au-TTF was also carried out with the same in-house assembled Raman microscope. The excitation wavelength generated by an Ar⁺ ion laser was fixed at $\lambda = 532$ nm and the ingoing polarization controlled using a half-wave plate. Focusing on the sample was done with a 50 \times objective (Olympus MPL, NA = 0.75, for TTF crystals) and a 100 \times objective (Zeiss EC Epiplan-NEOFLUAR, NA = 0.90, for Au-TTF). Different laser intensities were applied for TTF crystal and Au-TTF wire, in order to obtain the optimal Raman response. The laser intensity was about 15 μ W at the focal point for the analysis of TTF crystals with an acquisition time of 120 s per spectrum. For Au-TTF wires, a lower laser intensity (about 7 μ W) than the crystal and an acquisition time of 60 s per spectrum were applied to lower the heating effect on wire. The Raman signal was collected under a backscattering geometry. A polarizer served as an analyser just in front of the entrance slit of the spectrometer. Two polarizations were adopted in the measurement, by setting the polarization of the analyser on “0°” and “270°” for parallel and crossed polarization, respectively. A half-wave plate served to carry out the angular polarization experiments of wire structures. The angle of the polarized incident light was varied in the range of 0-360° by rotating the half-wave plate with the angle within 0-180°.

4 Methods-3: Sample preparation and characterization

In this chapter, the experimental procedure including microchip operation; sample preparation of Au-TTF, metal-TTF, TTF crystal and Cu-TCNQ; and the detailed characterization method and setups are introduced.

4.1 Microchip operation

In this work, both single layer and double layer microchips were used. For single layer microchip (used in Chapters 5.2 and 5.3), the reagents were loaded into plastic syringes and introduced into the chip through Teflon tubings using a syringe pump system (neMESYS module, Cetoni GmbH Korbüßen, Germany) that controlled the individual flow rates for the microchannels. The double layer microchip has a top (control) layer and a bottom (fluid) layer. Custom-made metal connectors and silicone tubing were used to supply N₂ gas into the control layer. Control channels were filled with water by pressurization before each experiment to get rid of bubbles. Regarding the fluid layer, reagents were supplied into microchannel via a syringe-pump system (NanoJet, ChemyxInc, Germany). For the project discussed in Chapter 5.1, the control layer was pressurized up to 3 bar for closing the donuts and immobilizing the wires, and then released to 2 bar in a functionalization step. For the project described in Chapter 5.4, the gas control channels was pressurized up to 3 bar for confining the microchamber, followed by a low pressure of 2 bar to allow the slow diffusion of solutions into microchamber. Detailed microchip operation procedures can be found in following chapters.

4.2 *In situ* synthesis, immobilization and functionalization of Au-TTF microwires

This part shows the experimental procedure related to the results in Chapter 5.1. *In situ* synthesis and immobilization of Au-TTF wires (Chapter 4.2.1), two functionalization methods applied to Au-TTF wires for biosensors (Chapter 4.2.2) and immunosensors (Chapter 4.2.3) are discussed here.

4.2.1 *In situ* synthesis and immobilization of Au-TTF microwires

Au-TTF wires were synthesized either by injecting the two solutions (TTF, 24 mM; HAuCl₄, 6 mM, both in acetonitrile (CH₃CN)) with a pipette into the microchip from either channel, or by diffusing HAuCl₄ solution (6 mM) into the microchannel filled with TTF solution (24 mM). In this project, the latter diffusion technique was mainly applied. After wire formation, the control layer was pressured to 3 bar by N₂ gas in order to trap the wires formed in the fluid layer. Non-trapped wires were washed away by the injected solvent. Afterwards, different solutions were supplied at low flow rates (2 to 10 μ L/min) into the microchannel, in order to avoid the flow forces to remove the structures. Also, air bubbles were carefully avoided to keep the biomolecules, particularly the antibodies, functional during the experiments. By using the microchips described in Chapter 5.1.1, the wires could be easily flushed away, just by releasing the pressure on the control layer and flushing with the solvent. Afterwards, new wires could be easily formed for further experiment by supplying new TTF and gold solutions into the channel. Thus, there was no need to recover the wires after an experiment, instead, they could be easily rebuilt.

4.2.2 Functionalization protocol for biosensing applications

Dopamine (DA) hydrochloride was dissolved in an ethanol/phosphate buffered saline (PBS) (1:1 solvent mixture (pH 7.2, PBS final concentration 10 mM) and diluted to various concentrations (5 μ M, 15 μ M, 25 μ M, 35 μ M, 50 μ M, 75 μ M and 100 μ M). The solvent mixture ethanol/PBS (1:1, pH 7.2) was used unless otherwise stated. Cysteamine (CEA) solution (10 mM) was firstly supplied into the channel (5 μ L/min for 15 min), then the flow was stopped for 15 min. After washing away excess CEA, glutaldehyde (GA) solution (5% v/v) was supplied into the channel (2 μ L/min for 20 min) and subsequently washed. Then, different concentrations of DA solutions were pumped into the channel (2 μ L/min for 20 min). After removal of excess DA and subsequent incubation with sodium cyanoborohydride (NaBH₃CN, 1 mM, 2 μ L/min for 15 min), the microchip was washed by PBS buffer (5 μ L/min for 5 min) and then directly used for Raman measurements.

In addition, the surface modification was proved by fluorescence microscopy. Generally, a lissamine rhodamine B sulfonylchloride solution (100 μ M, 5 μ L/min for 10 min) was used after CEA incubation. After removal of excess lissamine rhodamine B sulfonyl chloride by the solvent mixture (5 μ L/min, 15 min), fluorescence images were taken upon excitation with green light. On another chip, 6-aminofluorescein (100 μ M) and NaBH₃CN (1 mM) solutions

were used successively after supplying GA. Samples without the GA treatment were exposed to 6-aminofluorescein and NaBH_3CN solutions as a negative control. Blue light and appropriate optical filters were used for taking fluorescent images.

DL-Norepinephrine hydrochloride (NE), L-Epinephrine (EPI), Isoprenaline hydrochloride (ISP), L-Phenylalanine (Phe) and L-Tyrosine (Tyr) were dissolved in the solvent mixture to a concentration of 100 μM separately. The functionalization procedures are the same as those applied for DA.

4.2.3 Functionalization protocol for immunosensing applications

A dimethylsulfoxide (DMSO)/PBS 2:3 solvent mixture (PBS final concentration 10 mM) was prepared and the pH value was adjusted to 7.2. This solution was used as a solvent unless otherwise stated. Antigens (human IgG protein) was dissolved in the solvent mixture and diluted into 5 nM, 10 nM, 30 nM, 50 nM and 70 nM. 4-aminothiophenol (4-ATPh) (15 mM in CH_3CN) was supplied into the channel at a flow rate of 5 $\mu\text{L}/\text{min}$ for 15 min, then stopped the flow and kept reacting for another 15 min. At the same time, anti-human IgG antibody (20 $\mu\text{g}/\text{mL}$ in 10 mM PBS buffer, pH 7.4) was incubated inside a 1 mL tube with 1-Ethyl-3-(3-dimethyl-aminopropyl) carbodiimide (EDC, 100 mM in PBS) and N-Hydroxysuccinimide (NHS, 25 mM in DMSO) for 1 h. After washing off non-reacted 4-ATPh with CH_3CN (10 $\mu\text{L}/\text{min}$ for 10 min) and the solvent mixture (5 $\mu\text{L}/\text{min}$ for 10 min), structures inside donuts were incubated with the antibody solution for 30 min by pipette diffusion. Then, solvent mixture was used to wash non-bonded antibodies (5 $\mu\text{L}/\text{min}$ for 10 min). Followed by incubation with CEA (10 mM) as a blocking reagent, different concentrations of antigen (human IgG protein) solutions were supplied into the channel by pipette diffusion and incubated for 20 min. After washing away the excess antigen by PBS buffer (5 $\mu\text{L}/\text{min}$ for 10 min), the chip was applied for *in situ* Raman measurements.

As in the case of the biosensor, fluorescent microscopy served to prove the surface modifications. Lissamine rhodamine B (100 μM) was used after the incubation of 4-ATPh. Besides, FITC-labelled human IgG antibody (20 $\mu\text{g}/\text{mL}$ in PBS buffer, pH 7.4) was first incubated inside a 1 mL tube with EDC (100 mM, in PBS) and NHS (25 mM in DMSO) for 1 h, then supplying into the micro-channel by pipette diffusion for 30 min. After washing away surplus

FITC-labelled human IgG antibody with PBS buffer (5 $\mu\text{L}/\text{min}$ for 10 min), fluorescent images were taken under blue light excitation.

4.3 Synthesis of TTF crystal and Au-TTF nano-/microwires

This part shows the experimental procedure related to the results discussed in Chapter 5.2.

Formation of TTF crystal. Single TTF crystals were grown by recrystallization of commercially obtained TTF samples which were dissolved in hexane (saturated solution).^{130,131} TTF crystals formed bright orange needles, up to 2 cm long and about 0.25 mm² in cross section (Figure 4.1a). A single TTF crystal was selected under microscope for polarized Raman spectroscopy measurement at room temperature.

Formation of Au-TTF nano-/microwires. Different diameters of Au-TTF wires was synthesized on four-inlet microchips by controlling the flow rates of reactants²⁷ (see Figures 4.1b and 4.1c).

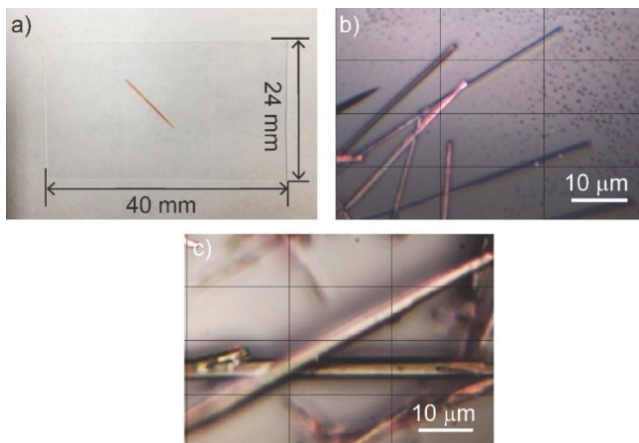


Figure 4.1. Images of TTF crystal and Au-TTF nano-/microwires. a) A picture of an orange TTF crystal (on a 24×40 mm glass slide). Images of Au-TTF wires under Raman microscope b) nanometre scaled, average diameter: 780 nm; c) micrometre scaled, average diameter: 4 μm . Various Au-TTF wires were synthesized on a four-inlet microchip. Scale bars: 10 μm .

4.4 Microfluidic synthesis of metal-TTF structures

The experimental procedures described in this chapter relate to the results in Chapter 5.3.

General method: The reactions between transition metal salts with TTF and its derivatives were performed on a single layer four-inlet microchip, where the inner channels are used for the precursor supply, and the outer channels for supply of pure solvent. The additional solvent streams focus the inner streams, and are referred to as sheath flow. The width of the microchannels for the inlets and main channel was 100 and 300 μm , respectively. In some cases, a two-inlet microchips was used as a comparison. Here, the inlet channels were 150 μm wide and the main channel had a width of 300 μm . The height of all the channels was 20 μm . The total length of the main reactor channel was 1 cm. For the microchannels of the four-inlet chip, a flow rate ratio of 10 was applied as for the synthesis of Au-TTF.²⁷ The two reactants were supplied through the middle channels at 50 $\mu\text{L}/\text{min}$. Two side streams of solvents were supplied through the side channels at 500 $\mu\text{L}/\text{min}$ (Figure 4.2).

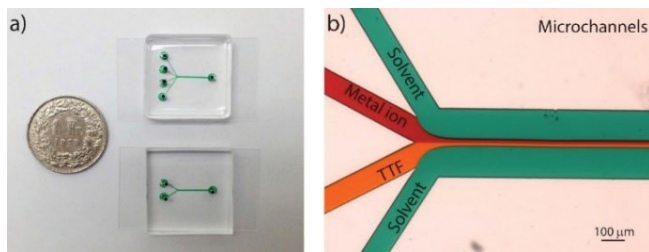


Figure 4.2. Photograph of microchips and optical image of microchannels. a) Photograph of the single layer four-inlet microchip (top) and two-inlet microchip (bottom) filled with green food dye (a one Swiss Franc is used for scale). b) Optical image of the microchannels of the four-inlet microchip filled with different food dyes. Metal ion solution in red, TTF (and its derivatives) solution in orange, side streams of solvents in green. Scale bar: 100 μm .

Solutions eluted from the microchips were collected and diluted 5 times with solvent (final concentration, approx. 0.06 mM) for UV-Vis measurements. The eluted structures were collected, filtered, washed by solvents and dried under

vacuum for FT-IR spectroscopy. In addition, the eluted structures from the chips were dropped on clean glass slides (Thermo Scientific, Menzel-Gläser, No. 3) and dried under N_2 gas. Then the glass slides with structures were gently rinsed with deionized (DI) water for 30 s and dried under a slow stream of N_2 gas before Raman analysis, SEM imaging and EDX measurements. In SEM and EDX experiments, the glass slide with samples were sputtered with Au/Pd (9/1) (or carbon for samples with gold) first and mounted on a sample holder for measurement.

In some cases, structures generated on a two-inlet chip was compared with those formed on the four-inlet chip. Here, only the metal salts and TTF derivative solutions were supplied at the flow rates of 100; 100 $\mu\text{L}/\text{min}$.

a. Synthesis of $(\text{TTF})_n\text{CuX}_2$ complexes: the two reactant solutions of CuX_2 ($X = \text{Cl}^-$, NO_3^-) (6 mM in CH_3CN) and TTF (24 mM in CH_3CN) were supplied from middle channels of the four-inlet chip, with the side channels used for CH_3CN . Structures were formed right after the injection of the solutions, elutes from the chips showed dark purple precipitates. An analogue method was used for the reactions in methanol (CH_3OH) by changing the solvents into CH_3OH .

b. Synthesis of $(\text{TTF})_n\text{FeX}_3$ complexes: the solutions of FeX_3 ($X = \text{Cl}^-$, NO_3^-) (6 mM in CH_3OH) and TTF (21 mM in CH_3OH) were injected from middle channels of the four-inlet chip, with side channels for CH_3OH . Structures were formed immediately, elutes from the outlet showed dark purple precipitates. An analogue method was used for the reactions in CH_3CN . As $\text{Fe}(\text{NO}_3)_3$ cannot fully dissolve in CH_3CN , a filtered solution was used for the reaction. So, here $\text{Fe}(\text{NO}_3)_3$ had a concentration of approx. 6 mM.

c. Synthesis of Cu-FTTF complexes: similar synthesis method to the synthesis of $(\text{TTF})_n\text{CuX}_2$ complexes were used by changing the organic ligand to FTTF (24 mM in CH_3CN). Here, only the reaction in CH_3CN was performed.

d. Synthesis of Fe-FTTF complexes: similar synthesis method to the synthesis of $(\text{TTF})_n\text{FeX}_3$ complexes were used by changing the organic ligand to FTTF (24 mM in CH_3OH). Here, only the reaction in CH_3OH was performed.

e. Synthesis of M-BEDT-TTF: the solutions of HAuCl_4 , CuX_2 ($X = \text{Cl}^-$, NO_3^-), FeX_3 ($X = \text{Cl}^-$, NO_3^-) (0.06 mM in CH_3OH) and BEDT-TTF (0.24 mM in tetrahydrofuran (THF)) were supplied into middle channel of the four-inlet chip, the solvent side streams were both CH_3OH .

4.5 In situ formation of Cu-TCNQ nano-/microstructures

The experimental procedures described here relate to the results discussed in Chapter 5.4.

Solution preparation. Copper sulphate (CuSO_4) and sodium citrate ($\text{C}_6\text{H}_5\text{O}_7\text{Na}_3$) powders were dissolved in DI water separately to form solutions of concentrations up to 0.5 M. ($\text{C}_6\text{H}_5\text{O}_7\text{Na}_3$ is used as an organic chelating agent that interacts with CuSO_4 and solubilizes Cu^{2+} ions present in solution, to form a copper-chelator complex.) A 1 M NaBH_4 solution was prepared using NaOH solution (pH=12) as solvent. A high pH value was used to stabilize NaBH_4 . TCNQ was dissolved in CH_3CN to get the solutions of 2 mM and 5 mM. Other concentrations of solutions were obtained by diluting the above-mentioned solutions using their separate solvents. In addition, to avoid air in the experiment, all the solutions were bubbled using Ar gas for 20 min before use.

Synthesis of Cu^0 layer and Cu-TCNQ. As illustrated in Figure 4.3 the formation of Cu^0 and Cu-TCNQ was achieved by the following steps:

- i) The middle control channel was pressed to 3 bar by N_2 gas to close the middle of the chamber, $\text{Cu}(\text{C}_6\text{H}_5\text{O}_7)_2^{4+}$ and NaBH_4 solutions were supplied from two inlets.
- ii) The two side gas channels was pressured to 3 bar to stop supplying solutions, then the middle gas channel was released to allow two solutions to mix. This led to the formation of Cu^0 .
- iii) DI water was supplied from the inlets. The left gas channel was released to 2 bar to allow water slowly diffusing into the chamber and wash Cu^0 .
- iv) CH_3CN was supplied (instead of water) from the left inlet to diffuse into the chamber and wash Cu^0 .
- v) TCNQ solution was supplied instead of water to diffuse into the microchamber and react with Cu^0 . Different morphology of structures were observed after the reaction (see Chapter 5.4.3 for details).
- vi) The solvent CH_3CN was introduced to wash off the TCNQ solution in the channel and microchambers.

Finally, the microchip was put in vacuum and allowed the solvent to evaporate. The resulted nano-/microstructures were obtained in the microchambers.

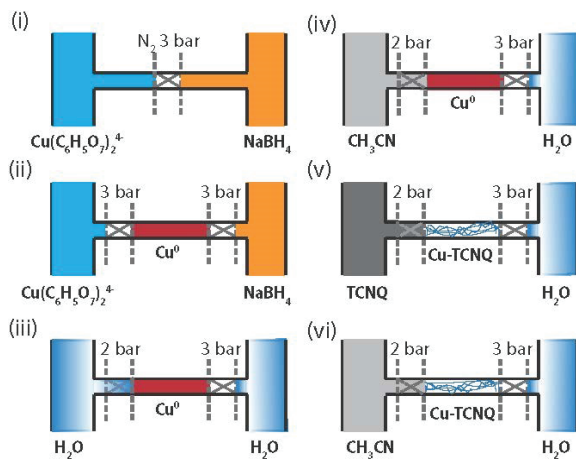


Figure 4.3. Schematic illustration of Cu-TCNQ wire formation in microchamber. Solid lines showed one of the sub-nanolitre microchambers, dashed lines showed the gas control channels.

The operation of gas control channels to enable the formation of Cu^0 and Cu-TCNQ is shown in Figure 4.4.

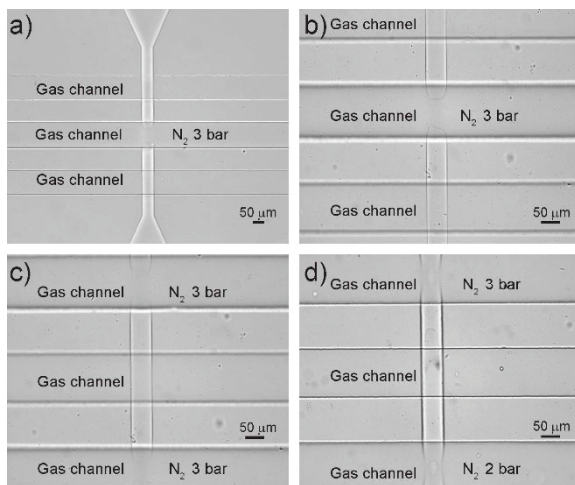


Figure 4.4. Optical images of a microchamber showing the operation of control layer. a)

The N₂ gas channel in the middle was pressured to 3 bar and totally close the chambers. b) Magnification image of that in a) which showing clearly the closing of microchamber. c) The image after releasing the middle gas channel and pressured the side gas channels to 3 bar to stop flows and allow the reaction in microchamber. Notice the totally closed chambers at the two side gas channels. d) The image after releasing a side gas channel from 3 bar to 2 bar to allow slow diffusing of solutions into microchambers. Notice the partially closed chamber under the gas channel with 2 bar N₂ gas pressure. Scale bars: 50 μm .

4.6 Sample characterization

4.6.1 Electrical characterization

TTF and TCNQ are organic semiconductors which can be used to form charge-transfer complexes with transition metal ions. These hybrid products show different electrical conductive behavior compared with that of pure organic molecules. In this work, electrical properties of TTF and TCNQ-based metal-organic charge-transfer complexes were measured by applying current/voltage sweeping between source and drain electrodes, with the main focus of understanding the non-linear electrical conductive response of these compounds.⁵

a) Label-free sensing application in nanoelectronics

Nano- and micrometre-sized conductive wires, integrated into devices and involving electronic transduction, could potentially be used as highly sensitive gas sensors e.g. for volatile organic compounds (VOC) or could be enriched with biological recognition capabilities via a proper functionalization and integration of small biomolecules, antibodies, enzymes, *etc.* The advantages over other sensing technologies such as electrochemical or fluorescent ones lie firstly on the capability of delivering a response that is label-free using a simple electronic readout setup, and secondly the scaled device at the nanometre level.

The sensing ability of Au-TTF wires was first proven by Cvetković and coworkers after direct exposure of the wires to polar and non-polar gases.²⁸ Au-TTF was proved to efficiently work as electrical sensing elements with the merits of an easy fabrication, a fast read-out, and nanometre-sized dimensions of the sensing devices. Other TTF-based metal-organic compounds are expected to have similar sensing properties, when formed using similar charge-transfer

techniques. A challenge in label-free sensing of nanodevices lies in the development of single wire devices, which enables the miniaturization of sensing elements. Much effort has been done in this project to synthesize and build single nanowire devices using TTF-based complexes. Detailed results and discussion on these aspects can be found in Chapter 5.3.

b) Conductivity measurement

The I - V curve measurements were performed to understand the electrical behaviour of metal-organic wire structures. For Au-TTF nano-/microstructures, the single wire conductivity was addressed by Dittrich group.²⁷ The source-drain current was measured while sweeping the applied source-drain voltage in a two-point configuration. The nonlinear I - V characteristics are an indication of a non-perfect contact interfaces, including small barriers, as the wires simply lay on the electrodes with no top-side metallization and subsequent annealing step performed. No gate effect was observed for the different devices, indicating the metallic behaviour of the Au-TTF charge-transfer structure.

To assess the conductivity of the other metal-TTF (derivatives) nanostructures, single wires were aligned on microelectrodes that were prefabricated on a glass slide by a home-built micro-manipulator. The conductivities of the aligned structures were obtained by carrying out four-point measurements. A current was applied through the source electrode pair (source high and source low), and the resulting potential on the sensing electrode pair (sense high and sense low) was monitored using a Keithley 2612A system source meter (Figures 4.5a and 4.5b). The electrical resistance of a single Au-TTF wire was determined by using the four-probe configuration program of Keithley 3706 system switch/multimeter (Figures 4.5c and 4.5d).

For Cu-TCNQ nano-/microstructures, the microchip was dried in vacuum after the formation of the nanostructures. Then, a four-point measurement method was applied. To investigate the electrical memory effect, a voltage sweep was applied on the source electrodes.

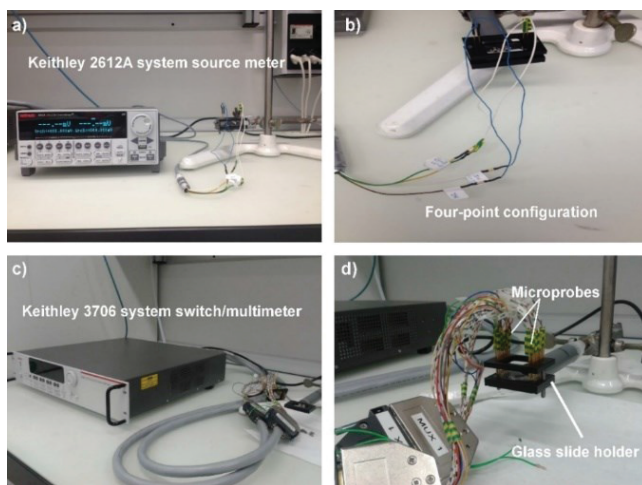


Figure 4.5. Photographs of conductivity measurement devices. a) Source meter for I - V curve measurements; b) Four-point measurement configuration (see Figure 5.24 right bottom for microelectrode configuration); c) Multimeter used for measurements of electrical resistance; d) 8 pairs of micro-probes aligned and connected to the microelectrodes on the glass slide.

4.6.2 Other characterization techniques

The UV-Vis spectra were recorded on a Genesys 10 UV scanning spectrophotometer (scanning capability from 190-1100 nm, Thermo Scientific) with disposable polystyrene (PS) semi-micro cuvettes (BRAND). Absorption spectra were obtained on a UV-Vis spectrophotometer (V-650, JASCO, Japan). IR spectra for metal-TTF and derivatives were obtained via a FT-IR Tensor 27 Infrared spectrophotometer (Bruker) equipped with a Bruker Golden Gate diamond ATR (Attenuated Total Reflection) cell. The IR transmission measurements of Cu-TCNQ were performed using TENSOR 37 (Bruker, Germany) FT-IR spectrometer with a DTGS detector. The resolution of spectra was 4 cm^{-1} . Elemental analysis was performed by the micro-laboratory group at the Laboratory of Organic Chemistry, ETH Zürich. SEM images and the energy dispersive X-ray spectroscopy-scanning electron microscopy (EDX-SEM) spectra were obtained using a FEI Quanta 200 FEG at the Scientific Centre for Optical and Electron Microscopy (ScopeM), ETH Zürich. Coloured and polarized images were recorded using a stereo microscope (AZ-100M, Nikon)

equipped with a digital camera (Digital sight DS-Fi1, Nikon). Fluorescent and other optical images were recorded on an inverted microscope (IX71, Olympus) equipped with a digital camera (UK1117, ABS) and standard filters.

4.7 Methods for data analysis

4.7.1 Data analysis of fluorescent images, Raman, IR spectra and $I-V$ curves

Fluorescent images were recorded, false-coloured and background-corrected using the Image J software. Raman spectra reported in Chapters 5.1 and 5.3 were recorded using WiTec Project software and analysed with Origin Pro 9.1 software (Academic, OriginLab Corporation). The implemented peak analyser tool of Origin Pro 9.1 served to get background-corrected spectra, peak position and intensity values.

Raman spectra reported in Chapters 5.2 and 5.4 were recorded using Nspec software (NanoScan Technology, GmbH). IR spectra were acquired using the OPUS software (21 CFR Part 11 compliant). The Raman and IR spectra of TCNQ and Cu-TCNQ were analysed with Origin Pro 9.1 (Academic, OriginLab Corporation). Conductivity data were recorded by TSP Express Software Tool and analysed with Origin Pro 9.1 software.

4.7.2 DFT calculations

In this work, the DFT calculations were used to obtain the exact values of Raman tensor of TTF molecules (neutral and TTF cation). The calculations carried out using the B3LYP level of theory supplemented with the standard 6-31+G (d,p) basis set and the Gaussian 09 program package.¹³² The geometry optimization and harmonic Raman frequencies of the different normal modes of neutral TTF (C_{2v} point group) and TTF cation (D_{2h} point group) in gas phase were calculated using DFT calculations. In order to get the Raman tensor element, the quadrupole moment was taken into account using the polar keyword in DFT calculations. The global minima on the potential energy surface were confirmed by the real harmonic vibrational wavenumbers calculated for both neutral TTF (C_{2v} point group) and TTF cation (D_{2h} point group). In the studies reported recently, DFT calculations with B3LYP method¹³³⁻¹³⁷ provided useful results for understanding the observed phenomenon (e.g. self-association and hydrogen

bonding in molecules, molecular vibration). The results on DFT calculation in this work are discussed in Chapter 5.2.

4.7.3 Single TTF crystal analysis

Crystal data were obtained from the Cambridge Structural Database (reference code BDTOL 10) and analysed by Mercury 3.6 software, which was downloaded from the Cambridge Crystallographic Data Centre. Calculations of molecular planes and angle measurements were carried out using the “Calculate planes” and “Picking mode: Measure Angles” tools implemented in the software.

5 Results and discussion

The results of four subprojects are discussed in this chapter. Chapter 5.1 describes the label-free biosensing application of *in situ* synthesized and functionalized Au-TTF microwires in a microchip. Chapter 5.2 illustrates the study on the molecular structure of TTF crystal and Au-TTF nano-/microwires by polarized confocal Raman spectroscopy. Chapter 5.3 shows the various products formed from different transition metal salts with TTF and its derivatives. In the last part (Chapter 5.4), the investigation of TCNQ-based metal-organic complexes is described.

5.1 Label-free biosensors based on *in situ* formed and functionalized microwires in microfluidic devices

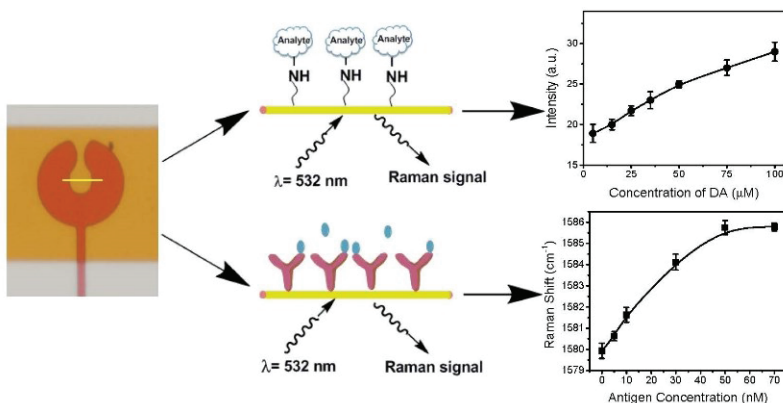


Figure 5.1 Graphic abstract of the sensing mechanism for the *in situ* label-free sensor in this work. An Au-TTF wire was formed and trapped by the open-donut feature, then two different surface modification procedures were done for two kinds of biosensors. The upper one is a surface modified Au-TTF with the ability to bind analytes with amino group e.g. dopamine. The lower one is a surface modified Au-TTF with antibody to detect respective antigens, e.g. human immunoglobulin G (IgG). Both sensing elements

achieved quantitatively measurement of biomolecules. Results on this work has been published in the peer-reviewed journal *Analyst* (2015, 140, 7896-7901. RSC publishing).

Label-free sensing of small molecules and proteins is of high interest for chemical gas and pH sensing, medical diagnostics, and pharmaceutical and biological applications. Novel tools for biosensing have been developed over the last years. Among them 1D nanostructures, i.e. fibres, wires and tubes have shown to be very promising and to work as sensing elements in an operating device. Although experimentally difficult to realize, it is indeed an intriguing outlook that only a single nanostructure is needed for the building of extraordinary small and portable instruments. In particular, when combined with microfluidic techniques, 1D nanostructure sensors can reveal their full potential for the detection of biological processes and multiplexing for parallel analyses of different target compounds. Microfluidic devices allow the formation, alignment, positioning and immobilization of nano- and micrometresized fibres, while at the same time the fluidic channels can be used as delivery systems to supply analytes to the sensing structures.¹³⁸ One of the intriguing prospects is that the integrated synthesis of the 1D structures and the final use in sensing applications on a single microfluidic device, rendering any nano-/microstructure manual handling or micromanipulation unnecessary.^{28,139,140}

In the past years, various materials have been utilized to form 1D structures for sensing purposes. For example, crystalline metal oxide nanowires like ZnO or SnO₂ are formed¹⁴¹ and used as capable building elements for conduct metric gas sensors. More difficult is the creation of a sensor for biomolecules which are dissolved in aqueous solution because special care is required for immobilization of the wires. Si-nanowire, which can be prepared as *p*- or *n*-type material and configured as field effect transistor based sensor device has been utilized to detect biomolecules such as DNA and proteins.¹⁴² In this context, semiconducting SWNTs should be also mentioned as they also have been successfully implemented into a device for sensing (bio)molecules in solution.^{143,144} Alternatively, hybrid systems created from metal salts and organic compounds have attracted a lot of attention, because of their tunable properties and applications in building nanodevices.¹⁴⁵ Au-TTF is a conductive metal-organic hybrid structure and can be formed in a controlled way by using microfluidic-based technology.²⁷ Dittrich group reported recently on the use of the wires for sensing of water based on conductivity,²⁸ and the sensing of vapours of polar organic solvents was also observed. In addition, the same group also showed the enhancement of the TTF Raman signal on Au-TTF wires.⁵¹

Based on these results, the possibility to use Au-TTF wires as sensing elements was proposed, with conductivity measurements for fast and online readout, and Raman spectroscopy for further identification of the detected molecules. However, to broaden the use of the wires for detection of a wide range of analytes, several challenges have to be solved including a method to position and functionalize the wires.

In this project, the realization of on-chip functionalization of single or few Au-TTF wires with different molecules¹⁴⁶ that have the ability to interact with gold are shown. These wires have diameters of a few hundred nanometres up to a few micrometres. To demonstrate that the integrated system is versatile for biological analysis, selective label-free sensing of catecholamines or human IgG by applying different modification approaches (Figure 5.1) are shown. The first one enables the direct sensing of catecholamines by confocal Raman spectroscopy and is based on wire functionalization by CEA and GA. The second one enables indirect sensing¹⁴⁷ by using the Raman tag 4-ATPh.¹⁴⁸ Here, an immunoassay is employed, where the antibody is bound to 4-ATPh and captures the target molecules (human IgG). To the best of knowledge, this is the first attempt to demonstrate the covalent binding of molecules on Au-TTF wire. In addition, the experimental method presented here can be proposed as a general means for the functionalization of 1D nano- and microstructures by single- or multi-step reactions.

5.1.1 Microchip and synthesis of Au-TTF microwires

The microdevice used is based on the previously reported microchip design of Dittrich group.²⁹ It consists of two layers made of PDMS, a fluid layer and a control layer that are separated by a 20 μm thin and flexible PDMS membrane. The control layer has several round shaped, donut-like features that have different diameters (50-250 μm) with an opening of 25 μm (Figures 5.2a and 5.2b). The two layers were first aligned and then bonded to a clean glass slide to form the final device (Figure 5.2c). The multi-layered microfluidic chip combines the ability to synthesize structures inside the fluid layer channel and to immobilize them by pressurizing the control layer to 3 bar with N_2 via the gas inlets. There are two advantages in using this design, firstly, the structures trapped inside the donuts are not exposed to the shear forces of the fluid flow, and secondly, fluids can diffuse into the donut traps through the openings, which enables the reaction between structures and solutions. In addition, extra fluids

can also be easily washed off solvents. As shown in Figure 5.2d, the fluid channel was filled with orange food dye to visualize the above-mentioned features of this microchip design. After pressurized the control layer, the food dye was flushed off by PBS buffer solution at a flow rate of $5\ \mu\text{L}/\text{min}$ in two minutes, which proved the efficiency in using this chip design for fluid change.

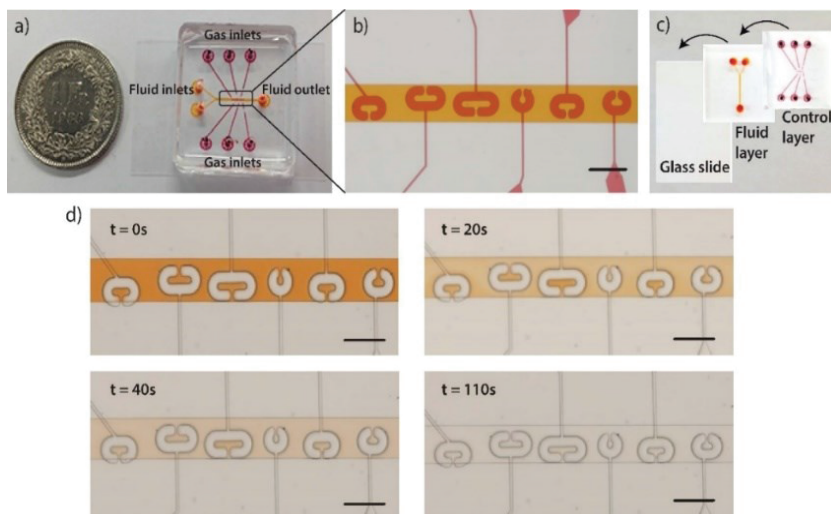


Figure 5.2. The open-donut microchip and its features. a) A photograph of the microdevice with two layers, the control layer filled with dark red dyes and the fluid layer filled with orange dyes. A one Swiss Franc was used for scale. b) A micrograph of the fluid channel and open-donut features. Scale bar: $300\ \mu\text{m}$. c) Schematic of the fabrication of the multilayer chip. d) The optical pictures of a bonded chip filled with food dye after washing with PBS buffer at $5\ \mu\text{L}/\text{min}$ in 110 s. Scale bars: $300\ \mu\text{m}$.

In the synthesis of Au-TTF wires, dissolved TTF in CH_3CN (24 mM) was added into the device and afterwards, HAuCl_4 (6 mM in CH_3CN) was introduced into the channel through the inlet reservoirs. The slow diffusion enabled the electron transfer between the two reactants and the direct formation of Au-TTF wires in the microchannel, which were easily monitored on an optical microscope (Figures 5.3 and 5.4a). By applying N_2 through gas inlets, the wires formed inside the pneumatic cages could be

trapped easily for further functionalization (Figure 5.4b). The morphology and composition of Au-TTF wires formed with this diffusion technique were demonstrated by SEM (Figure 5.4c) and EDX-SEM (Figures 5.4d and 5.4e). The EDX spectrum in Figure 5.4e clearly indicates the presence of Au and S in the Au-TTF wire, compared to that of the glass slide (Figure 5.4d). The formed wires were about 2 μm in diameter and varied in length from tens to several hundred micrometres. Thus, different traps in the control layer were used to immobilize different lengths of wires. A similar chip with eight small diameter traps (50-100 μm) was also used in our experiment. In the case of a diffusion formation of Au-TTF microwires, as observed in this work, an increased number of traps with smaller diameter can effectively trap more wires (Figure 5.5).

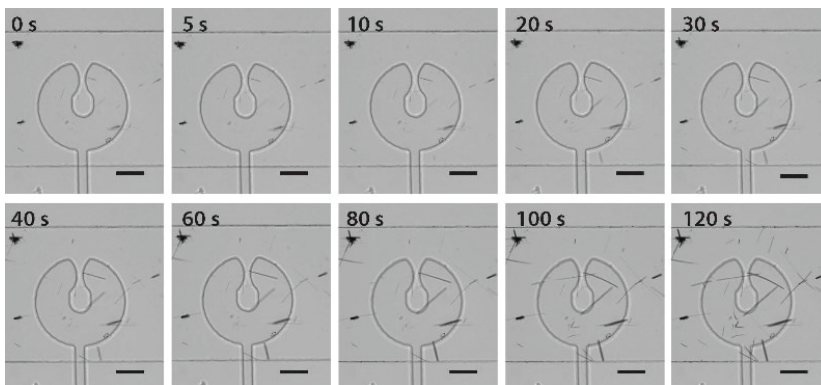


Figure 5.3. Images of Au-TTF wire formation. Time sequence of micrographs under optical microscope during the diffusion-based formation of Au-TTF microwires. Scale bars: 50 μm .

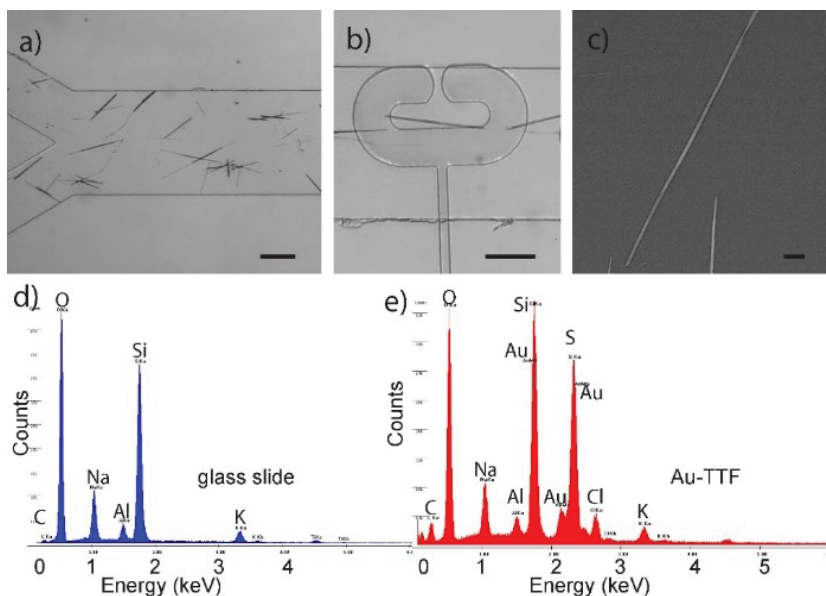


Figure 5.4. Characterization of Au-TTF wires. a) Optical microscope images of Au-TTF wires formed inside a chip by diffusion. (Scale bar: 100 μm). b) A wire formed inside the open-donut (Scale bar: 100 μm). c) SEM image of Au-TTF wires synthesized by solution diffusion on a non-bonded chip. In this case the long wire is approx. 2 μm in width and 110 μm in length. Scale bar: 10 μm . EDX spectra of d) the glass slide and e) an Au-TTF wire.

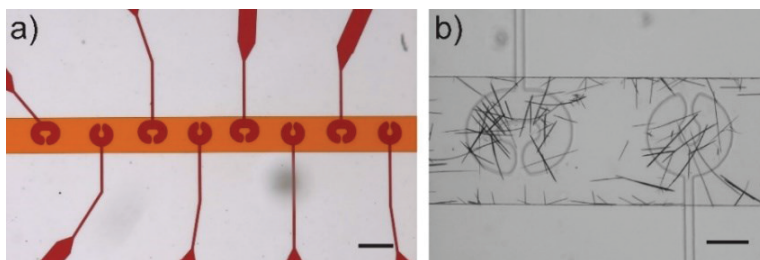


Figure 5.5. A second microchip design for wire formation. a) A micrograph of the micro-channel and 8 open-donuts with diameters of 50 μm and 100 μm in an alternated way.

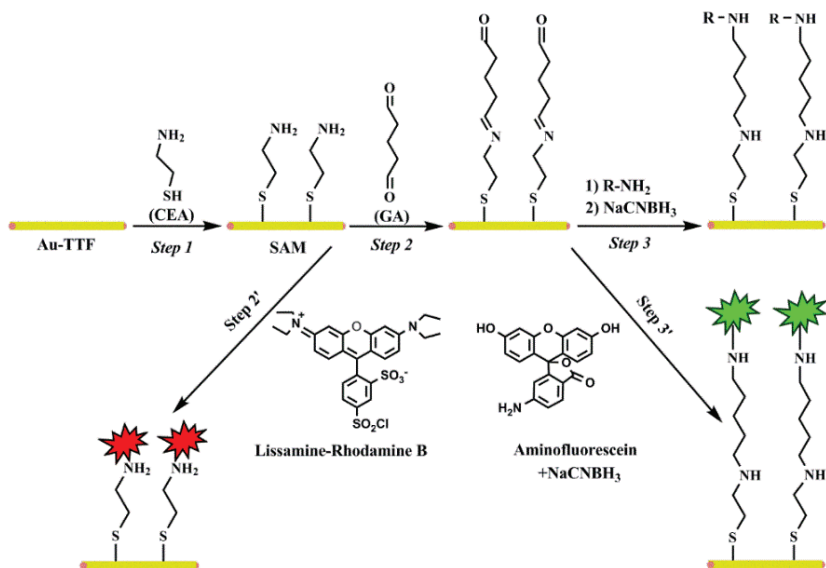
Scale bar: 300 μm . b) An optical image showing the bundles of wires trapped inside the microchips. Scale bar: 100 μm .

5.1.2 Label-free biosensing of catecholamines

Due to the presence of Au^0 on Au-TTF wires, further modification can be achieved by using molecules that have the ability to interact with gold. The surface functionalization protocols applied for sensing aims are reported here. Firstly, bioamines e.g. catecholamines, which play vital role in human body and bioprocess.¹⁴⁹ To investigate the possibility in using Au-TTF wires as sensing elements for label-free detection of catecholamines, a surface modification of the wires was applied and demonstrated.

a) Functionalization of Au-TTF wires for biosensing

The functionalization of Au-TTF as biosensors for catecholamines is indicated in Scheme 5.1 (*Step 1-Step 3*). First of all, CEA was used to form a self-assembled monolayer (SAM) on wire surface by Au-S bond (*Step 1*), then GA was bond to CEA by the reaction between carboxylic and amine group to form a Schiff base (*Step 2*).¹⁵⁰ Afterwards, the aldehyde terminal group of GA was exploited for the detection of biomolecules with amine group and Raman activity (*Step 3, 1*). Finally, NaCNBH_3 (*Step 3, 2*) was used to reduce Schiff bases to more stable second amine.¹⁵¹ Using this method, catecholamines could be covalently bonded to the wire surface and directly monitored by their Raman signals by a label-free fast readout. The selectivity of this method depends on the analytes themselves which can be differentiated by their own typical Raman peaks.



Scheme 5.1. Functionalization on Au-TTF wire for the sensing of amines (RNH₂). Step 1: Formation of SAM of CEA on Au-TTF wire surface; Step 2: Binding of GA to amino group; Step 3: 1) Binding of bioanalytes with amino group RNH₂ and 2) following treatment with NaCNBH₃. Reaction schemes for the binding of lissamine-Rhodamine B to amino group (step 2') and amino fluorescein to aldehyde group (step 3'). This protocol can be used for detecting other chemical or biomolecules with amino group, the detection of bioamines (e.g. catecholamines) is the focus of this work.

To confirm the formation of the SAM of CEA and the following GA bonding, fluorescent probes that reacted with the terminal groups of the substrates were added after each step. As shown in Scheme 5.1 the reaction mechanisms (*Step 2'*), the amino-active fluorescent dye Lissamine Rhodamine B sulfonylechloride was utilized after *Step 1*. The binding of fluorescent dye molecules to amino group exhibits its fluorescence, and proves that CEA formed a SAM on the wire surface. Similarly, 6-aminofluorescein which is aldehyde-active was used after *Step 2*. The successful wire modification with GA can be demonstrated by the fluorescence from amino fluorescein (*Step 3'*).

Based on this method, the wires were firstly trapped on different chips (Figures 5.6a and 5.6b). Dark images were taken before supplying fluorescent dyes into microchips, even under laser excitation (Figures 5.6c and 5.6d). However, after using fluorophores separately, the fluorescent wires (Figure 5.6e) indicated the reaction between the amino groups and Lissamine Rhodamine B sulfonylchloride, which proved the formation of SAM of CEA on the wire surface. Similarly, the fluorescent wires in Figure 5.6f confirmed the reaction between the aldehyde group and 6-aminofluorescein, and demonstrated the successful binding of GA. In addition, to explain the important role of GA, a control experiment without GA was performed and showed no fluorescence even after the incubation with 6-aminofluorescein (Figure 5.7).

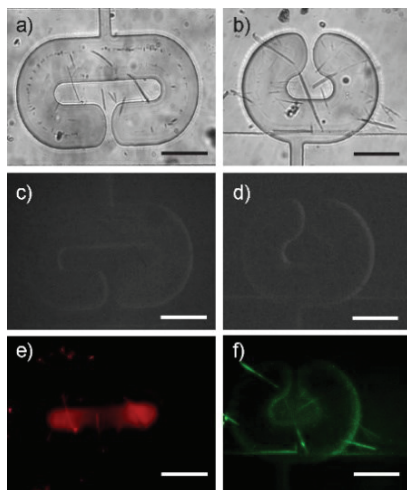


Figure 5.6. Fluorescent images of wires after surface modification for biosensors. a) and b) Bright field images of nanowires immobilized by different donuts. c) and d) Fluorescent images after incubation with CEA (10 mM) separately, before supply of the fluorophores. Scale bars: 100 μm . False-coloured fluorescent images of trapped wires after reaction with e) 10 mM CEA, 100 μM Lissamine Rhodamine B sulfonylchloride (green laser excitation) and f) 10 mM CEA, 5% GA, 100 μM 6-aminofluorescein and 1 mM NaCNBH_3 (blue laser excitation) separately. Scale bars: 100 μm .

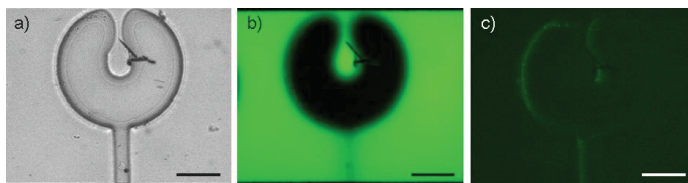


Figure 5.7. Control experiment without GA solution. a) Bright field image of nanowire immobilized by donut. b) False-coloured fluorescent image after incubation with CEA (10 mM) and 6-aminofluorescein (100 μM). c) False-coloured fluorescent image after supplying of NaCNBH_3 (1 mM) and washing with PBS. Blue light excitation was used for fluorescent images. Scale bars: 100 μm .

b) Direct sensing of catecholamines

In this part, direct sensing means that Raman signals come from the analytes. After demonstrating the feasibility of the first protocol, catecholamines including the well-known neurotransmitter DA,¹⁵² as well as NE, EPI and ISP (molecular structures in Appendix) were detected separately by the above-mentioned direct sensing protocol. Micro-Raman spectroscopy was performed to get signals from every single wire. It has been reported that Au-TTF wire has a typical Raman peak at around 1426 cm^{-1} (C=C stretching).⁵¹ Compared to the spectra of the single Au-TTF wire, two additional Raman peaks appeared at 1268 cm^{-1} (C-O stretching) and 1476 cm^{-1} (phenyl C=C stretching) after using DA (Figure 5.8a), which clearly demonstrated the binding of DA to the modified wire.¹⁵³ Another important neurotransmitter is NE, which has a structure similar to DA. In the spectrum of NE, typical peaks at 1268 cm^{-1} (C-O stretching) and 1479 cm^{-1} (phenyl C=C stretching) were observed. The spectrum is $0\text{--}3\text{ cm}^{-1}$ shifted with respect to the corresponding bands in DA and has a slightly lower intensity (Figure 5.8a). The other two catecholamines, EPI and ISP, only showed very weak Raman peaks (Figure 5.8a), which may due to their own weak Raman intensities.¹⁵⁴ To prove the selectivity of the system, aromatic amino acids that are related to the formation of neurotransmitters in bioprocess, Phe and Tyr (Figure 5.8b), were also measured using the same method applied to catecholamines. However, Phe and Tyr exhibited totally different Raman bands with respect to those of DA (Figure 5.8a). Thus, using the proposed technique, on the basis of the observed Raman bands, catecholamines can be distinguished from other bioamines in the wavenumber range of $1200\text{ cm}^{-1}\text{--}1700\text{ cm}^{-1}$.

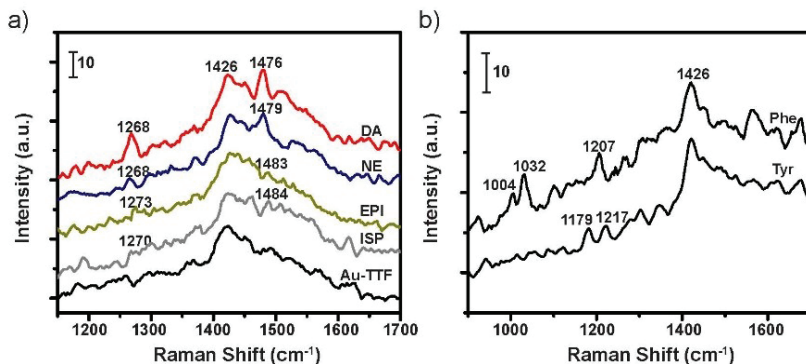


Figure 5.8. Raman spectra of various bioamines on functionalized Au-TTF wires. a) Comparison of the Raman spectra of single Au-TTF wire and after separate reaction with 100 μM different catecholamines: NE (1268 cm^{-1} , C-O stretching and 1479 cm^{-1} , phenyl C=C stretching), EPI (1273 cm^{-1} , C-O stretching and 1483 cm^{-1} , phenyl C=C stretching) and ISP (1270 cm^{-1} , C-O stretching and 1484 cm^{-1} , phenyl C=C stretching). b) Raman spectra of Au-TTF wires after reaction with 100 μM aromatic amino acids including Phe (1004 cm^{-1} , ring breathing; 1032 cm^{-1} , in plane ring bending and 1207 cm^{-1} , C₆H₅-C stretching) and Tyr (1179 cm^{-1} , in plane C-H bending and 1217 cm^{-1} , benzene ring stretching) separately. In this project, the functionalization of Au-TTF is on focus, thus, only typical Raman peaks are shown here. For detailed Raman spectra analysis of Au-TTF, see the results discussed in Chapter 5.2.

Moreover, a quantitative analysis was carried out using dopamine. Although DA has a weak Raman signal,¹⁵⁵ changes in the Raman intensities with an increasing concentration ranging from 5 μM to 100 μM (Figure 5.9a) were observed. The signal intensities at 1476 cm^{-1} (phenyl C=C stretching) was plotted against the DA concentration and used for the quantification of DA. A baseline-corrected peak intensities at 1476 cm^{-1} are shown in Figure 5.10. It is evident in Figure 5.9b, increasing Raman intensities were detected with the increment of micromolar concentrations of DA. A linear response of the Raman intensities and DA with respect to the concentration of 5 to 50 μM was obtained (Figure 5.9b inset). In addition, a detection limit of ~ 5 μM was achieved via this approach, and resulted lower than a recently reported Raman-based method (~ 100 μM).¹⁵⁵

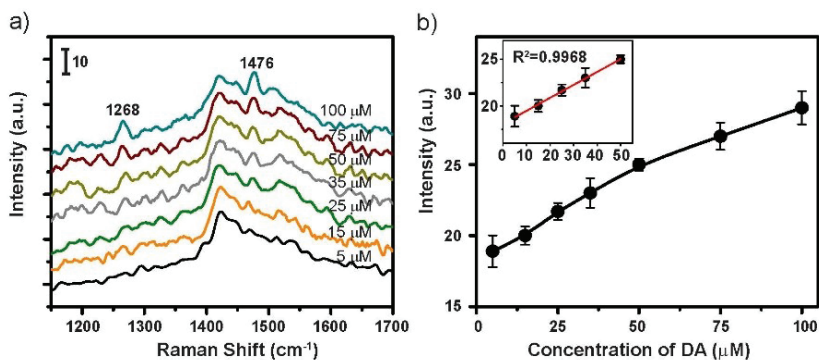


Figure 5.9. Quantitative Raman measurement of DA based on the functionalized wire for biosensor. a) Representative Raman spectra of the biosensor for increasing concentrations of DA from 5 μM -100 μM . b) Raman intensity at around 1476 cm^{-1} for different concentrations of DA after data correction. The inset figure shows the linear relationship in the concentration of 5-50 μM (coefficient of determination: $R^2=0.9968$). Error bars indicate standard deviations from six measurements.

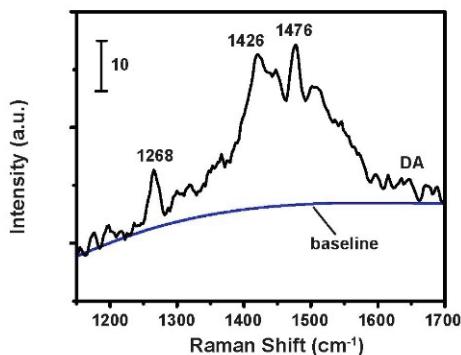
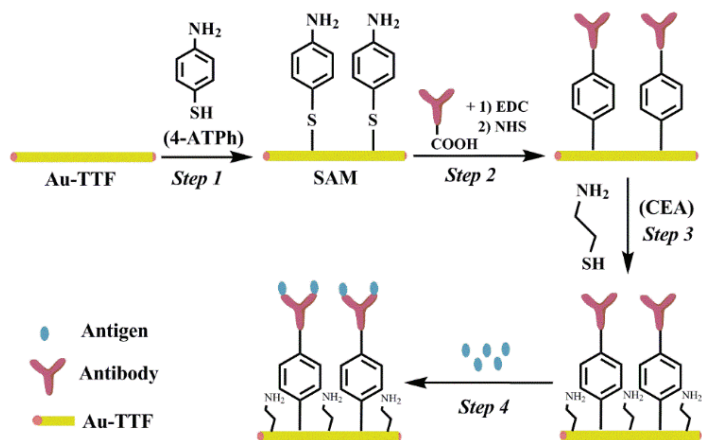


Figure 5.10. Data analysis method of Raman spectrum. The Raman spectrum of Au-TTF wire after reaction with 100 μM DA (black) and the modelled baseline by Origin Pro 9.1 software (blue).

5.1.3 Label-free immunosensors for detection of human IgG

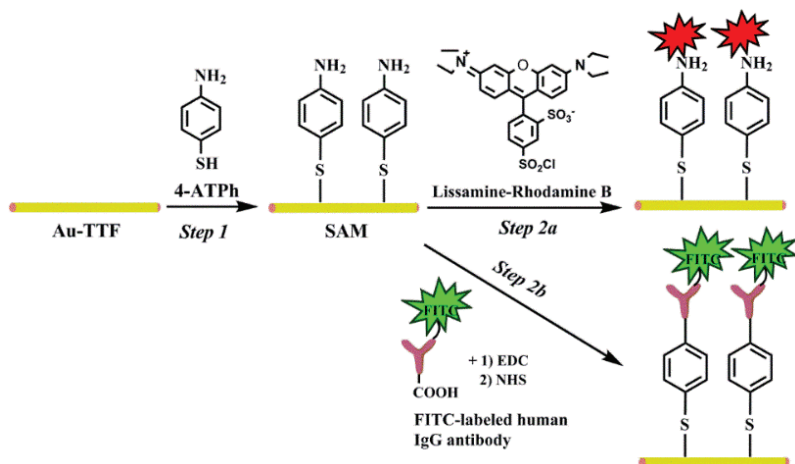
a) Functionalization of Au-TTF wire for immunosensing purposes

Evaluation of such microfluidic integrated Au-TTF wire systems for sensitive label-free immunoassay was done by using another surface modification protocol and testing how human IgG as molecular targets. In this approach, the Raman reporter molecule, 4-ATPh served as a linker between the wire and the capture antibody. Reported studies have proved that 4-ATPh acts as a nano-mechanical stress sensor and can be employed as an indicator of the antigen-antibody binding events.¹⁴⁸ As the Raman signal changes originated from the Raman reporter 4-ATPh while not the analysed antigens themselves, this method is also known as an indirect sensing method. The sensing mechanism is based on the deformation of the stretching mode of the benzene ring of 4-ATPh upon binding of antibodies and antigens. This can result in a change of Raman frequencies of the Raman reporter molecule.^{148,156} Thus, Raman shifts of 4-ATPh correspond to different concentrations of antigens binding to antibodies. Scheme 5.2 shows the procedure for the functionalization of the wire. Firstly, the SAM of 4-ATPh was formed on the wire surface (Scheme 5.2, *Step 1*). Immobilization of the capturing antibody (anti-human IgG) was realized in two steps: firstly, activating the carboxyl terminal of the antibody with EDC/NHS, a wide used method for activating the carboxyl group,¹⁵⁷ and secondly by the reaction of the antibodies with the amino group of 4-ATPh to form an amide bond (Scheme 5.2, *Step 2*). To improve the specific binding of antigens, CEA was used as the blocking reagent (Scheme 5.2, *Step 3*). Finally, human IgG was applied as antigens (Scheme 5.2, *Step 4*).



Scheme 5.2. Functionalization of Au-TTF wire for immunoassay. Step 1: SAM of 4-ATPh; Step 2: Immobilization of the capturing antibody (anti-human IgG) by using EDC/NHS. Step 3: Blocking unreacted wire surface by CEA and Step 4: Antigen (human IgG) binding.

As in the label-free sensing of catecholamines (Figure 5.6), fluorescently tagged compounds were used to test the surface modification. Lissamine Rhodamine B was used to prove the binding of 4-ATPh to the wire (Scheme 5.3, *Step 2a*), while the covalently bond of FITC-labelled anti-human IgG antibody to show the attachment of other antibodies (Scheme 5.3, *Step 2b*). After the immobilization and functionalization of the wires separately (Figures 5.11a and 5.11b), the dark images were obtained before fluorophores were supplied (Figures 5.11c and 5.11d). Then fluorescent images were recorded after introducing fluorophores, which clearly demonstrated the reaction between Lissamine Rhodamine B and the SAM of 4-ATPh (Figure 5.11e), as well as the successful binding of pre-treated FITC-labelled anti-human IgG antibody to 4-ATPh (Figure 5.11f).



Scheme 5.3. Reaction mechanisms for binding of fluorophores to the SAM of 4-ATPh: for lissamine Rhodamine B (Step 2a), and for the binding of FITC-labelled antibody after pre-treatment with EDC/NHS (Step 2b).

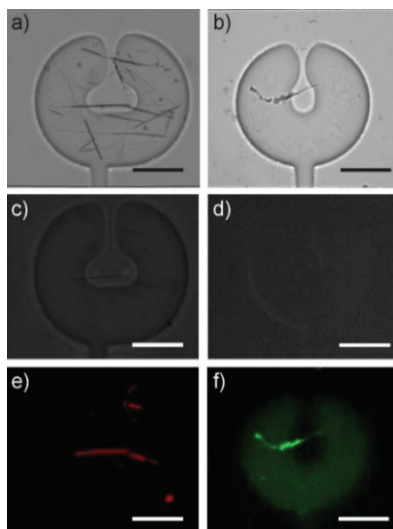


Figure 5.11. Fluorescent images of wires after the surface modification as immunosensor. a) and b) Bright field images of the trapped wires inside the donuts, c)

Fluorescent image after reaction with 4-ATPh (15 mM) but without Lissamine Rhodamine B sulfonylchloride (green light excitation), d) Fluorescent image after reaction with 4-ATPh (15 mM), but without FITC-labelled human IgG (blue light excitation). Fluorescent images of trapped wires after reaction with e) 15 mM 4-ATPh and 100 μ M Lissamine rhodamine B sulfonylchloride; and f) 15 mM 4-ATPh and 20 μ g/mL FITC-labelled human IgG antibody (pre-treated by EDC/NHS). Scale bars: 100 μ m.

b) Indirect Sensing of human IgG

In this part, indirect sensing means that the Raman signals originates not from the analyte but a Raman reporter molecule. On the basis of the proposed immune-sensor approach, Raman spectroscopy was applied to the label-free indirect immunoassay of human IgG. Figure 5.12a shows the Raman spectra of pure solid 4-ATPh, Au-TTF and the modified Au-TTF/4-ATPh. Pure 4-ATPh crystal showed typical bands at 390 cm^{-1} (CS bending), 470 cm^{-1} (CCC bending), 1092 cm^{-1} (CS stretching) and 1597 cm^{-1} (benzene ring stretching) (curve i), all of the bands belonging to a_1 modes.^{158,159} Au-TTF wire showed its characteristic Raman peaks at 506 cm^{-1} (in plane ring bending) and 1426 cm^{-1} (C=C stretching) (curve ii). Compared to the Raman spectrum of pure 4-ATPh (curve i), the one from the Au-TTF modified with 4-ATPh (curve iii) showed differences such as the absence of the peak at 470 cm^{-1} and the peak shift from 1092 cm^{-1} to 1080 cm^{-1} , as well as the shift from 1597 cm^{-1} to 1581 cm^{-1} . This indicated the formation of the SAM of 4-ATPh on Au-TTF wire.¹⁵⁸ Spectra of the antibody-conjugated wire (Au-TTF/4-ATPh/anti-human IgG) incubated with different concentrations of antigen (0 nM to 70 nM) are shown in Figure 5.12b. The typical Raman peak around 1580 cm^{-1} (which corresponds to the benzene ring stretching of 4-ATPh molecule) was responsive to the supplying of antigens after their selective binding to antibodies.¹⁵⁶ As shown in the magnified spectra in Figure 5.12c, the Raman frequencies of the sensor shifted to higher wavenumbers for about 5.7 cm^{-1} with the increasing concentration of human IgG ranging from 0 to 70 nM, in agreement with the previously reported works.^{148,156} Figure 5.12d showed the calibration curve of the immunoassay with a plateau at larger concentrations. This indicated the saturation of the antigen-antibody complex. A good linear correlation of Raman shift with antigen concentrations was shown in the range below 50 nM (Figure 5.12d, inset). This approach demonstrated its high sensitivity and a low detection range (5 nM).

In these experiment, due to the larger diameter of the wires (approx. 2 μ m, Figure 5.4c) than that of the confocal Raman laser point (approx. 400 nm), the

Raman signals were collected from the single wires. In addition, the reasonable small error bars of Raman signals obtained from different structures indicated the reproducibility of the two protocols proposed in this project (Figures 5.8b and 5.12d).

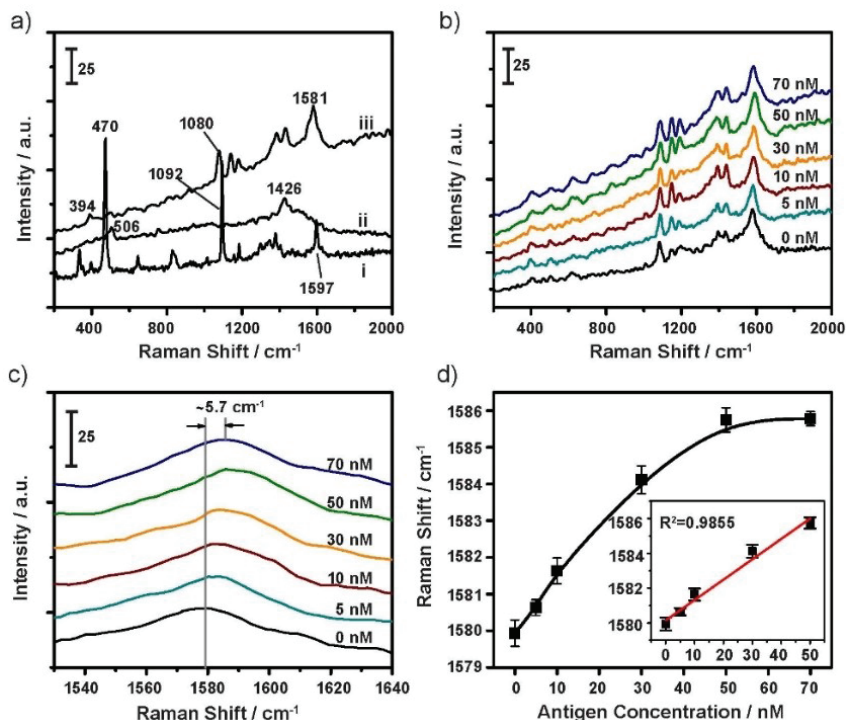


Figure 5.12. Raman measurement data of functionalized wire for immunosensor. a) Raman spectra of pure 4-ATPh (curve i), Au-TTF wire (curve ii) and Au-TTF/4-ATPh (curve iii). b) Representative Raman spectra of the immunosensor in the presence of increasing concentrations of human IgG from 0 nM to 70 nM. c) Magnification of Raman peaks at around 1580 cm^{-1} (benzene ring stretching) of those in b). d) Corresponding Raman shifts to different antigen concentrations. The inset figure shows the linear relationship within the concentration range of 0 - 50 nM (coefficient of determination, $R^2 = 0.9855$). Error bars indicate standard deviations from six measurements.

After proving the functionalization and sensing application of Au-TTF wires, the growth mechanism of Au-TTF wire is of great interest since Au-TTF can form wire structures with a different diameter. Thus, the molecular assembly in a single wire structure needs to be further addressed. In the following chapter, the structural analysis of Au-TTF wires via non-destructive polarized Raman spectroscopy is discussed in detail.

5.2 Study of molecular self-organization in TTF crystals and individual Au-TTF nano-/microwires by polarized confocal Raman spectroscopy

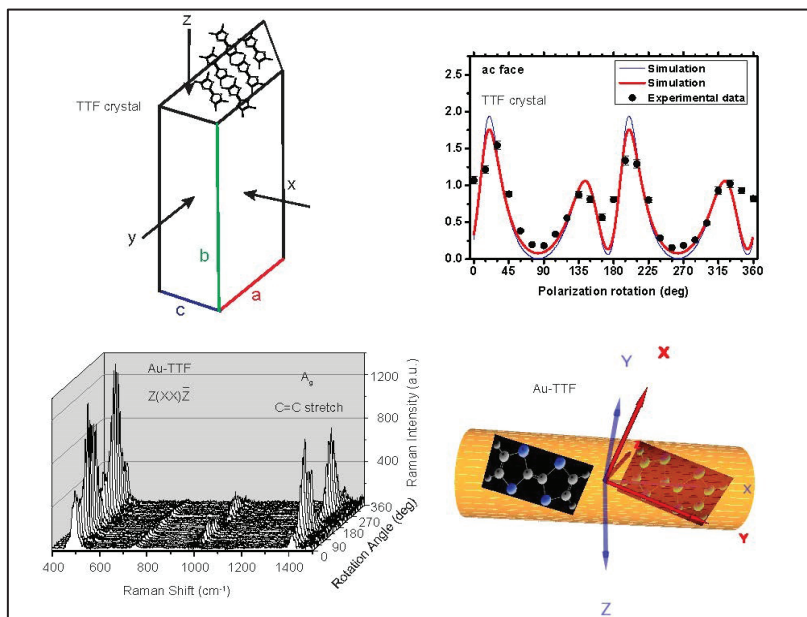


Figure 5.13. Graphic abstract of the polarization Raman measurement of TTF crystal and Au-TTF wire. The molecular ordering of TTF in a single crystal is studied by rotational polarization Raman spectroscopy. The same analysis was applied to a single Au-TTF nanowire. The tilted stacking of TTF molecules along the wire growth direction was demonstrated as shown in the 3D model.

In this work, the molecular orientation in a single TTF crystal and an Au-TTF nanowire was firstly studied via polarized confocal Raman spectroscopy, by taking into account the rotational polarization dependence of the molecular vibrational modes (Figure 5.13). To determine molecular ordering in a crystalline assembly, the Euler's angles of the molecules need to be determined using polarized Raman spectroscopy and known Raman tensors of TTF molecule. Upon rotation of incoming laser on different faces of the crystal, the

Raman intensity of molecular vibrational modes changed with a certain periodicity, suggesting a preferential molecular orientation in the crystal. Based on the DFT calculations of the Raman tensor and the simulation of depolarization ratio, the molecular assembly in a single TTF crystal was confirmed, in accordance with the single crystal X-ray diffraction data. Thus, the efficiency of the proposed method to study TTF-based materials was proved.

Afterwards, the same technique was applied to investigate the self-organization of TTF molecules and TTF cations in single Au-TTF charge-transfer nanowires. Polarization-dependent spectra of single Au-TTF nano-/microwire clearly proved that TTF molecules are assembled in a certain orientation in the wire structure. The stacking way of TTF units inside a single wire was modelled based on the simulated depolarization ratio data. Finally, the tilt stacking of TTF units along the wire growth direction was obtained.

5.2.1 DFT calculations of Raman tensor

Optimized molecular structures of TTF and TTF⁺ are shown in Figure 5.14. The optimization of TTF molecule forms the non-planar structures in such a way that the symmetry of TTF drops to C_{2v} point group. The optimization of TTF⁺ radical shows that TTF⁺ forms a planar structure having D_{2h} point group of symmetry. It is more likely that the torsional changes are produced by the four sulphur atoms presents in TTF molecule. The DFT calculation results showed that neutral TTF has a boat-like structure with C_{2v} symmetry, while the radical cation has a planar D_{2h} symmetry (Figure 5.14), which is both in accordance with reported work.¹⁶⁰

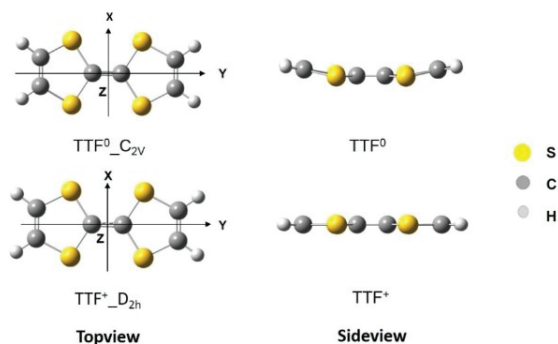


Figure 5.14. DFT modelling of TTF and TTF cation.

Molecular vibrations can be described by the sum of normal internal vibrations of atoms. It is possible to classify the normal vibrations by applying the group theory.¹⁶¹ Each normal vibration will have a symmetry corresponding to one of the irreducible representations of the molecular point group. If a molecule has a centre of inversion, the vibrations that are centrosymmetric show Raman active properties, which are usually labelled with the subscript *g*. The symmetry of a given vibrational mode is reflected in its corresponding Raman tensor.¹¹² The Raman tensors for C_{2v} (TTF neutral) and D_{2h} (TTF cation) are show in Table 5.1, the two point groups are isomeric. The Raman tensor values calculated for both TTF and TTF⁺ are depicted in Table 5.2 (detailed calculation method see Chapter 4.7.2).

Table 5.1. Raman tensors for the symmetry classes of the C_{2v} and D_{2h} point groups*

Point group C_{2v}		Symmetry class			
		A_{1g}	A_{2g}	B_{1g}	B_{2g}
TTF		$\begin{pmatrix} a & 0 & 0 \\ 0 & b & 0 \\ 0 & 0 & c \end{pmatrix}$	$\begin{pmatrix} 0 & d & 0 \\ d & 0 & 0 \\ 0 & 0 & 0 \end{pmatrix}$	$\begin{pmatrix} 0 & 0 & e \\ 0 & 0 & 0 \\ e & 0 & 0 \end{pmatrix}$	$\begin{pmatrix} 0 & 0 & 0 \\ 0 & 0 & f \\ 0 & f & 0 \end{pmatrix}$
Point group D_{2h}		Symmetry class			
		A_{1g}	B_{1g}	B_{2g}	B_{3g}
TTF ⁺		$\begin{pmatrix} a & 0 & 0 \\ 0 & b & 0 \\ 0 & 0 & c \end{pmatrix}$	$\begin{pmatrix} 0 & d & 0 \\ d & 0 & 0 \\ 0 & 0 & d \end{pmatrix}$	$\begin{pmatrix} 0 & 0 & e \\ 0 & 0 & 0 \\ e & 0 & 0 \end{pmatrix}$	$\begin{pmatrix} 0 & 0 & 0 \\ 0 & 0 & f \\ 0 & f & 0 \end{pmatrix}$

* Raman tensors of point group are from Bilbao Crystallographic Server.

Table 5.2. Calculated Raman tensor values

Molecule	Point group	Traceless Quadrupole moment (field-independent basis, Debye-Ang)*					
		XX (a)	YY (b)	ZZ (c)	XY (d)	XZ (e)	YZ (f)
TTF	C_{2v}	-5.0235	16.8375	-11.8140	0.0000	0.0000	0.0000
TTF ⁺	D_{2h}	-24.3185	-7.8936	32.2121	0.0000	0.0000	0.0000

*XYZ coordinates of the molecules refers to Figure 5.14.

5.2.2 Polarized confocal Raman spectra of single TTF crystals

a) X-ray crystal structure of single TTF crystals

TTF appears in two polymorphs, one is the orange crystal with monoclinic form which is named α -TTF, the other one is the yellow crystal with triclinic form, known as β -TTF. The single crystal structure of α -TTF has been extensively studied at room temperature by Cooper *et al.* in early 1970s^{162,163} It has been reported that at low temperature (about 190 K), the monoclinic α -TTF crystal undergoes a reversible second-order phase transition to β -TTF.¹³⁰ This project is focused on the study of the orange monoclinic TTF crystal at room temperature. TTF (refers to α -TTF, so as in the following text) shows a based-centred monoclinic lattice, with two molecules per unit cell, as can be seen from X-ray diffraction data (Figure 5.15).^{6,164} The view from ab face and bc face indicated that there is an angle between the two molecule planes (49.45°) (Figure 5.15).

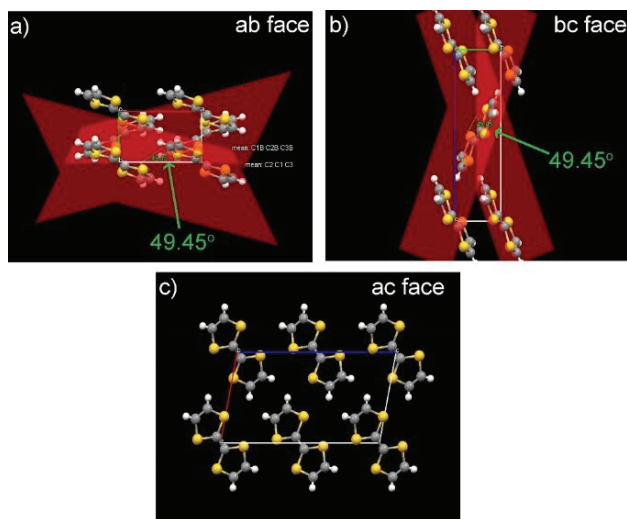


Figure 5.15. The view from three faces of crystalline TTF and the calculated angle between two TTF molecules in a unit cell of TTF crystal. a) b) c) Views of TTF crystal (Cambridge Structural Database, reference code: BDTOLE10) from three faces of the unit cell (ab, bc, ac separately) in Mercury 3.6 software. Angle between molecular planes were calculated to be 49.45°. The structure was reported in Reference 163.

Following, in order to prove the efficiency in using our method to study TTF-based structures, the polarized Raman measurement on TTF crystal and simulation of depolarization ratio were carried out. Afterwards, the calculated angle between two molecules in TTF crystal will be compared to the data obtained from the reported work.

b) Raman spectrum of single TTF crystals

The TTF crystal structure with the definition of abc faces and xyz configuration for incoming laser is shown in Figure 5.16a. The Raman analysis was carried out at different faces with the laser beam in the backscattering configuration. The polarization of the laser light was selected by using a polarizer under parallel and perpendicular configurations. A full spectrum of TTF crystal from bc face at room temperature showed the assignments of typical Raman peaks (Figure 5.16b), with the peaks at 315 cm^{-1} , 471 cm^{-1} , 1089 cm^{-1} and 1516 cm^{-1} belonging to A_g vibration, while the peak at 58 cm^{-1} belonging to B_g vibration.^{6,165} In this work, only the A_g modes were investigated at room temperature. A detailed work in studying B_g mode at low temperature (80 K) was reported in literature.⁶

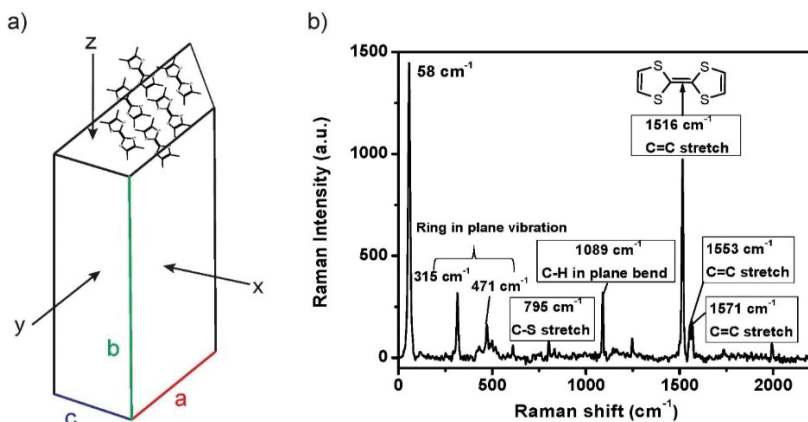
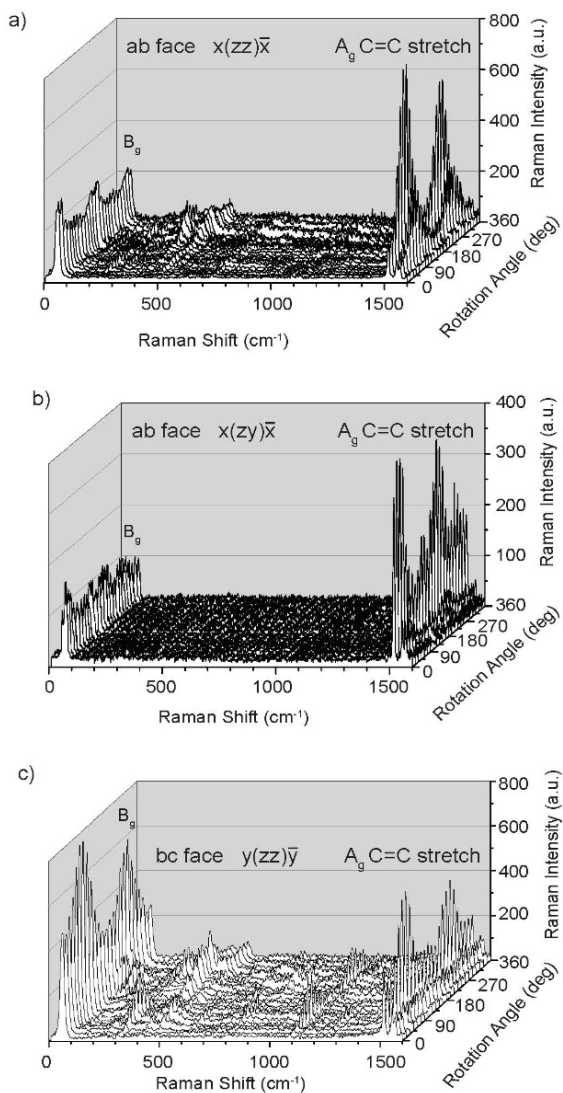


Figure 5.16. Sketch of TTF crystal and a Raman spectrum. a) A sketch of TTF crystal with the definition of abc faces and xyz configuration for incoming laser. b) A full spectrum of TTF crystal from bc face.

c) Polarized Raman spectra of ac, bc and ab faces of TTF crystal

With the aim to study the molecular orientation of TTF molecules in a single crystal, polarization-dependent Raman spectra measurements were carried out. The rotational polarization dependence of the molecular vibrational modes was studied upon rotating the incoming laser polarization with steps of 15° . Two polarized configurations, parallel and crossed, were used. As indicated in Figure 5.17, the Porto notations (see Chapter 3.4.2) of three faces of TTF crystal, $x(zz)\bar{x}$ (Figure 5.17a) and $x(zy)\bar{x}$ (Figure 5.17b) represent the parallel/crossed polarization at ab face, while $y(zz)\bar{y}$ (Figure 5.17c) and $y(zx)\bar{y}$ (Figure 5.17d) representing those for bc face, and $z(xx)\bar{z}$ (Figure 5.17e) and $z(xy)\bar{z}$ (Figure 5.17f) for ac face. Upon the rotation of incoming laser, the Raman intensity of molecular A_g vibrational modes changed with a periodicity under both parallel and crossed configurations, suggesting a preferential molecular orientation in the crystal. Typically, the central C=C stretching A_g mode at $\sim 1516\text{ cm}^{-1}$ can be used for both qualitative and quantitative analysis. As seen from Figure 5.17, the Raman intensities of A_g modes of the crystal varied with a period of 180° in the parallel polarization (Figures 5.17a, 5.17c and 5.17e), while with a period of 90° in the crossed polarized configuration (Figures 5.17b, 5.17d and 5.17f). The highest Raman signal in the parallel polarization was obtained when incoming laser was perpendicular (rotation angle 90°) to the starting axis in the corresponding faces.



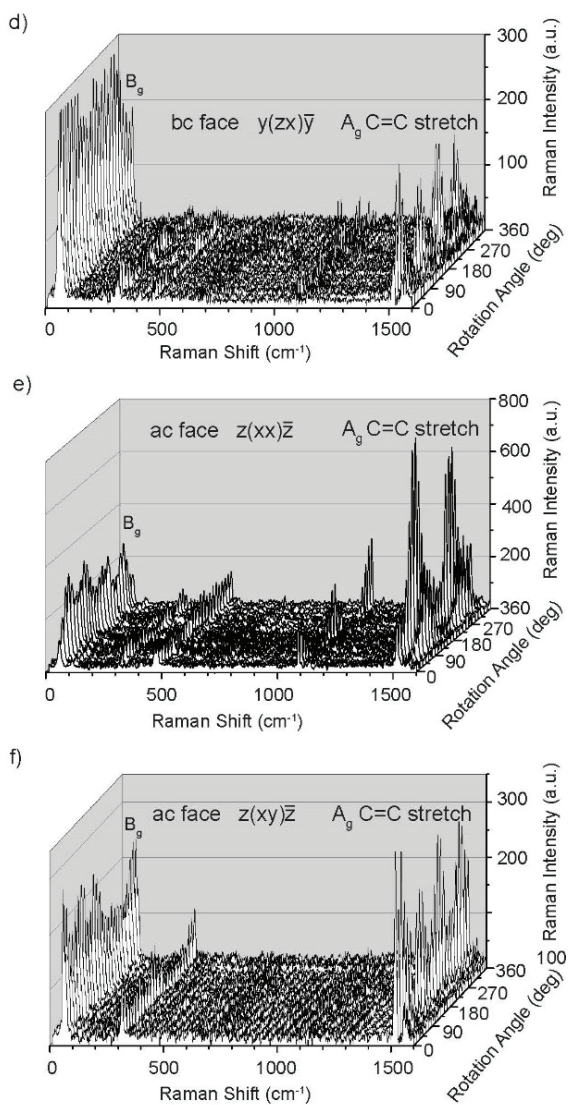


Figure 5.17. Angular variations of Raman spectra from different faces of TTF crystal under parallel and crossed polarization configurations. a) and b) Angular polarization Raman spectra of ab face under parallel and crossed polarization respectively. c) and d)

Those spectra of bc face. e) and f) Those spectra of ac faces. The abc axes of the crystal and xyz configuration of incoming laser refer to Figure 5.16a, \bar{x} , \bar{y} , \bar{z} indicate the direction of backscattered light. For ab and bc faces, angle 0° is always defined along z axis, while for ac face angle 0 is defined along \bar{x} axis.

d) Simulation of depolarization ratio

To describe the translational movement of a molecule, three coordinates are employed. Furthermore, if the molecule is non-linear, three additional coordinates as the Euler's angles (typically denoted as α , β , γ , or φ , θ , ψ) are necessary to define the orientation of the molecule in space. When molecules building a crystal, the total number of normal coordinates is related to the number of molecules in the unit cell. For TTF crystal, there are two molecules in the monoclinic unit cell (see Figure 5.15). Thus, a two molecule system is adapted for the simulation of depolarization ratio.

In addition, it is noteworthy that the depolarization ratio is nearly zero, when assuming the scattered light is totally polarized. This is an ideal situation. However, taking the real experimental values into consideration, the intensities of scattered light in parallel and perpendicular need to be expressed with a constant factor (or depolarization error) D . Thus, the depolarization ratio P is expressed as in Equation 5.1¹¹²:

$$P = \frac{(1-D)I_{xy} + D \cdot I_{xx}}{D \cdot I_{xy} + (1-D)I_{xx}} \quad (5.1)$$

In ideal situation, when $D = 0$, P can be described as $P = I_{xx} / I_{xy}$ (Equation 3.7, Chapter 3.1.3).

The constant factor D is ~ 0.12 when fitting for the three faces. It has been reported that the depolarization ratio is useful in analysing the polarization response of a substrate.¹⁶¹ The experiment and simulated data of depolarization ratio of the 1516 cm^{-1} mode (C=C stretching) under angular variation of three faces (ab, bc, ac) of the crystal are shown in Figure 5.18. Symbols represent the experimental data. The blue line is the ideal depolarization ratio simulation ($D = 0$) and the red line is the simulated depolarization ratio with a constant factor D . A high correlation of experimental data with simulated results from three different faces of the crystal was observed.

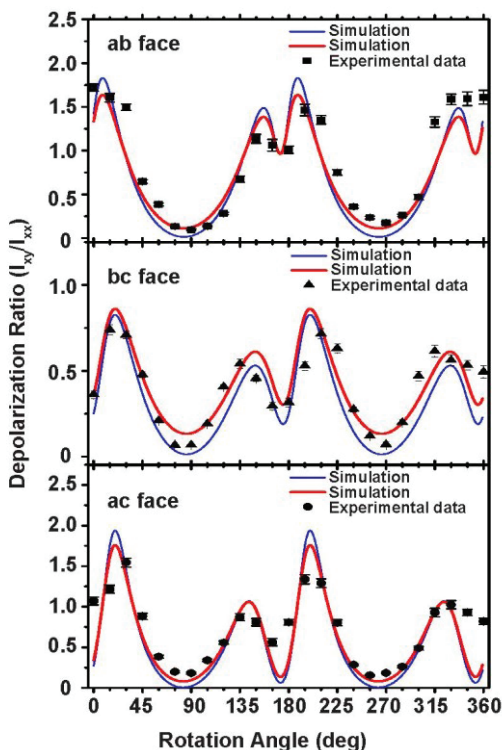


Figure 5.18. Simulated depolarization ratio of TTF crystal. Experimental (symbols) and simulated (lines) depolarization ratio of assignment at $\sim 1516\text{ cm}^{-1}$ obtained upon rotation with certain angles around the normal of three faces of TTF crystal. Blue line is the ideal simulation, red line is the simulation with depolarization error. abc axes of the crystal as in Figure 5.16a.

Based on the simulation of depolarization ratio, the angle between the two molecules in the crystal were obtained. The angles simulated from different faces were 49.4° (from ac face), 48° (from bc face), 49.2° (from ab face). All the angles obtained from simulated results (Figure 5.18) were in the range of $49.45^\circ \pm 1.5^\circ$, indicating a good correlation of the simulated data with the experimental data (49.45° , Figure 5.15). Thus, the proposed method was proven to be efficient to model the molecular orientation of TTF-based materials.

5.2.3 Polarized confocal Raman spectra of single Au-TTF nanowires

a) Polarized Raman spectra of Au-TTF nanowires

After proving the efficiency of the proposed method on TTF crystal, the same method was applied to the analysis of single Au-TTF nano-/microwires. Firstly, the spectra of a single Au-TTF wire under parallel and crossed polarization configurations were obtained. The typical peaks for the partially charged TTF shifted from those of neutral TTF molecules (Figure 5.16b), showing typical Raman peaks at 504 cm^{-1} (in-plane vibration), 1011 cm^{-1} (C-H in-plane bend) and 1415 cm^{-1} (C=C stretch) (Figure 5.19). A comparison of the Raman assignments of TTF, TTF^{n+} ($0 < n < 1$) and TTF^+ is shown in Table 5.3. In addition, the different spectra from two parallel polarizations ($Z(\text{YY})\bar{Z}$ and $Z(\text{XX})\bar{Z}$, Figure 5.19) indicate that TTF molecules are assembled in a certain orientation in the wire.

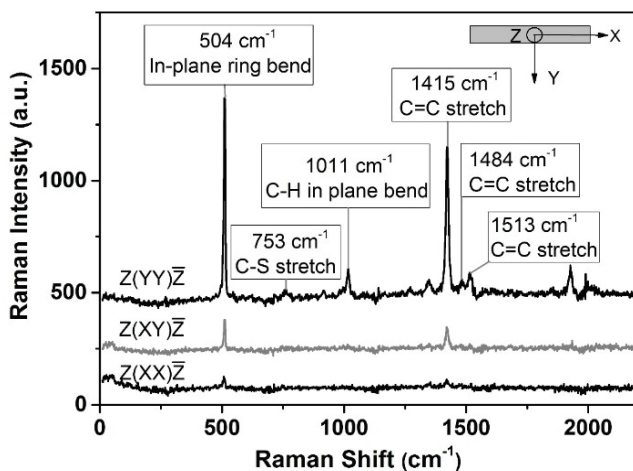


Figure 5.19. Raman spectra of single Au-TTF wire under parallel (black curves) and crossed (grey curve) polarization configurations. The full spectrum of under $Z(\text{YY})\bar{Z}$ configuration shows the typical assignments. Figure inset indicates the XYZ direction on a single wire. \bar{Z} indicates the direction of backscattered light.

Table 5.3. Raman assignments of TTF, TTFⁿ⁺ (0<n<1) and TTF⁺

Vibrational modes (A _g symmetry)*	TTF	TTF ⁿ⁺ (0<n<1)	TTF ⁺ *
<i>v</i> ₂ C=C stretch	1560 cm ⁻¹	1513 cm ⁻¹	1510 cm ⁻¹
<i>v</i> ₂ C=C stretch	1548 cm ⁻¹	1484 cm ⁻¹	1481 cm ⁻¹
<i>v</i> ₃ C=C stretch (ring-ring)	1516 cm ⁻¹	1415 cm ⁻¹	1416 cm ⁻¹
<i>v</i> ₄ C-H in plane	1089 cm ⁻¹	1011 cm ⁻¹	1088 cm ⁻¹
<i>v</i> ₅ C-S stretch	795 cm ⁻¹	753 cm ⁻¹	758 cm ⁻¹
<i>v</i> ₆ In-plane ring bend	471 cm ⁻¹	504 cm ⁻¹	506 cm ⁻¹

* The symmetry species numbers, frequencies of TTF⁺ see Reference 10. Raman shifts for TTF⁰ and TTFⁿ⁺ (0<n<1) are the results from this work.

b) Angular polarization Raman spectra of Au-TTF nanowire

Following, the angular based polarization Raman spectra of Au-TTF were obtained upon rotation of incoming laser every step of 15°. As shown in Figure 5.20, the Raman intensities of A_g modes (504 cm⁻¹ and 1415 cm⁻¹) varied with a period of 180° in parallel polarization (Z(XX)Z̄, Figure 5.20a), and 90° in crossed polarization configuration (Z(XY)Z̄, Figure 5.20b). The highest Raman signal in parallel polarization was obtained when incoming laser was nearly perpendicular (rotation angle 90°) to the long axis of the wire.

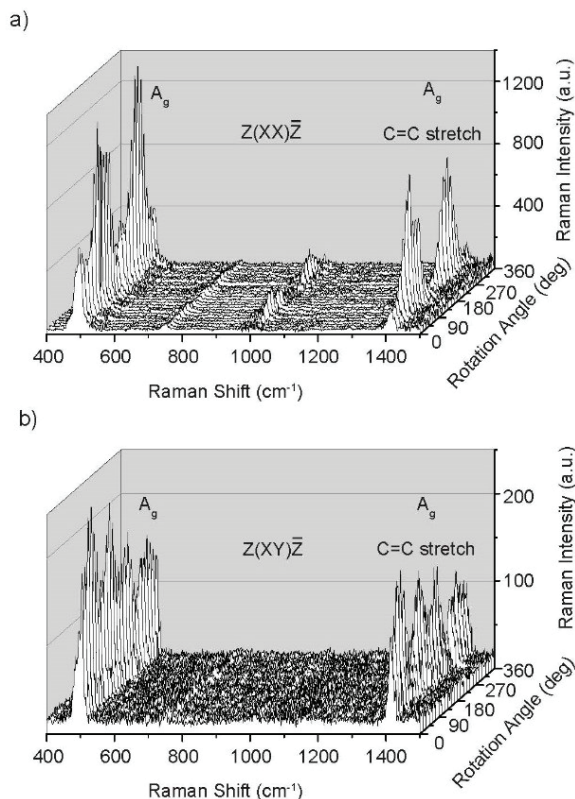


Figure 5.20. Angular variation of Raman spectra of single Au-TTF nanowire under parallel and crossed polarization configurations. The XYZ configurations refer to Figure 5.19, \bar{Z} indicate the direction of backscattered light of Z. The 0° angle is defined along the X axis of wire.

c) Simulation of depolarization ratio

To study the depolarization ratio of Au-TTF nanowire, six different wires with the diameter of ~ 700 nm were randomly chosen for polarized Raman measurement. The simulation method for TTF crystals was applied to simulate also Au-TTF nanowires. The simulated values of depolarization ratio of 1516 cm^{-1} peak under angular variation are shown in Figure 5.21. Symbols represent

the experimental data. The blue line is the ideal depolarization ratio simulation ($D = 0$), and the red line is the simulated depolarization ratio of that with a constant factor D . Here, a D value of ~ 0.1 was applied for all the fitting curves.

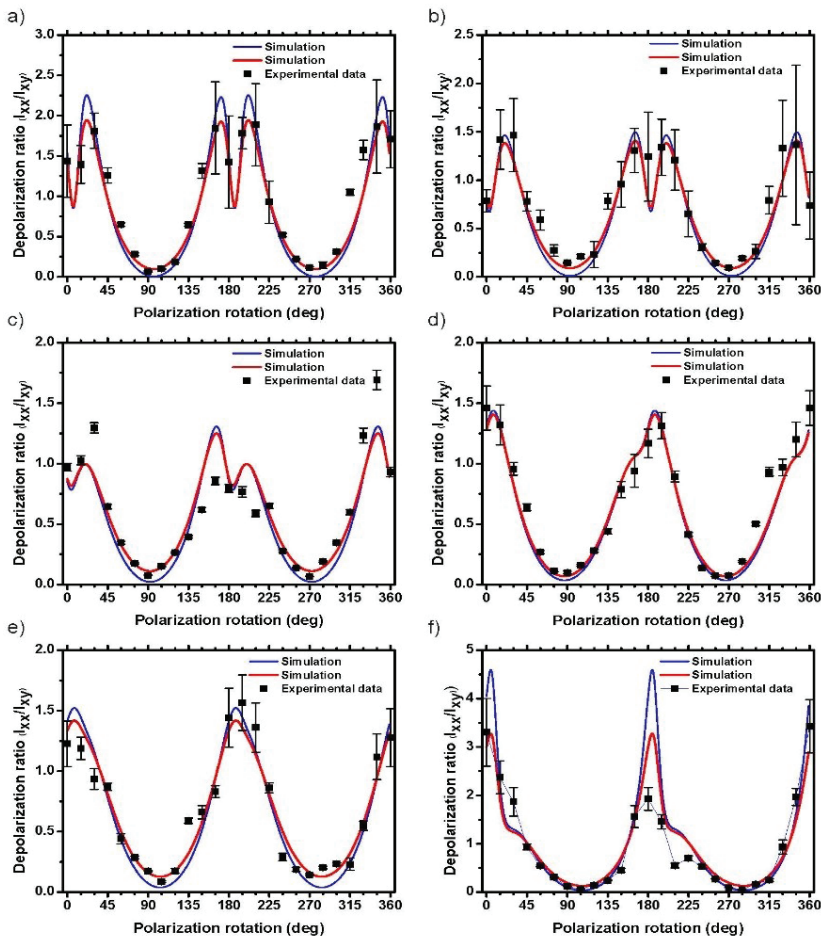


Figure 5.21. Simulated depolarization ratio of six Au-TTF nanowires. Experimental (symbols) and simulated (lines) depolarization ratio of assignment at $\sim 1415 \text{ cm}^{-1}$ obtained upon rotation with certain angles around X axis of Au-TTF wire (Figure 5.19). The blue line is the ideal simulation, while the red line is the simulation with depolarization constant factor.

For the simulation of depolarization ratio of Au-TTF nanowires, a two-molecule system was needed. This resulted in a good fitting with the experiment results. Thus, this suggests two different molecular orientation exist in a single nanowire. The angle between the two molecules was calculated as $126 \pm 0.7^\circ$. With this angle, all the simulated curves (Figure 5.21, red line) showed high correlation with experimental data (Figure 5.21, black solid square). However, the angular based depolarization ratio of the six nanowires showed different variations (Figure 5.21, experimental data). Since all these data can be simulated using the angle of $126 \pm 0.7^\circ$, the difference in experimental data can be explained by the rotation of the wires when they were randomly deposited on the glass slide for measurement.

d) Molecular orientation of TTF⁰ and TTF⁺ in single nanowire

The 3D model was obtained from the simulation, with molecules rotated according to the Euler angles. As indicated in Figure 5.22, the yellow cylinder indicates Au-TTF nanowire with the two molecules inside the wire structure. Blue XYZ coordinates refers to the wire coordinates (the same as that shown in Figure 5.19 inset), where the blue X is the wire growth direction and the Red XYZ is the molecule coordinates, which in accordance with the ones used in the DFT calculations (Figure 5.14). A partially charged TTF molecule A is positioned according to the Euler angle (α, β, γ) derived from the simulation, then a second molecule B is defined with the angle of $126 \pm 0.7^\circ$ to the molecular plane of A.

It can be seen from the 3D model that the two molecules are oriented along the wire growth direction, with an obvious tilt angle with respect to the long axis of the wire. Similar molecular orientation results were obtained from the six different wires, which proved the reproducibility of the method and similar properties of the two substrates. The above-mentioned results give the direct evidence to explain the growth of Au-TTF wire: firstly, the molecules are assembled along the long axis of the wire and this enables the stacking of charged TTF molecules and the growth of wire in length; and secondly, with the tilt angle of the molecules to the long X axis (blue axis), TTF molecules can be stacked along Y (blue axis) and Z (blue axis) directions. This results in the different diameter of Au-TTF wires from nanometre to several micrometres (see Chapter 4.4 and References 27,28,100).

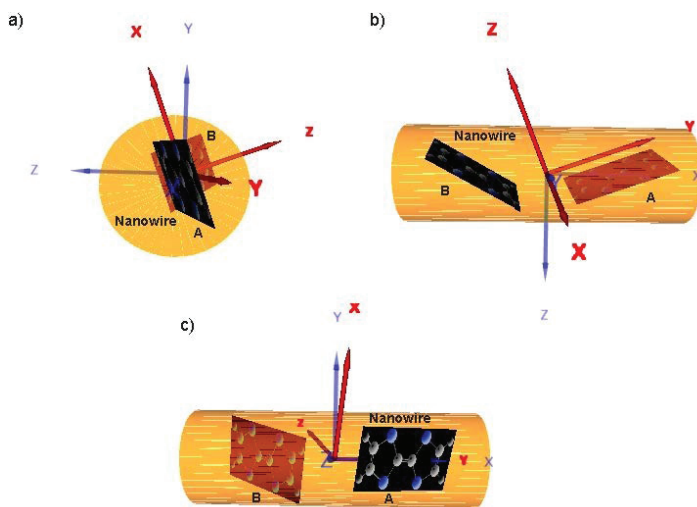


Figure 5.22. The 3D models of Au-TTF wire showing rotation of molecules. Blue XYZ coordinates refers to the wire coordinates, while red XYZ coordinates showing the molecule coordinates.

To conclude, the molecular orientation in an individual Au-TTF nanowire was determined and used to understand the growth mechanism of Au-TTF wires. It was deduced that the orientation of TTF molecules in a charge-transfer nanowire could influence the properties of the wire, e.g. absorbing molecules on the surface. In the following chapter, the microfluidic-assisted synthesis based on different metal-organic complexes using transition metal ions and TTF derivatives is of interest.

5.3 Conductive single nanowires formed and analysed on microfluidic devices

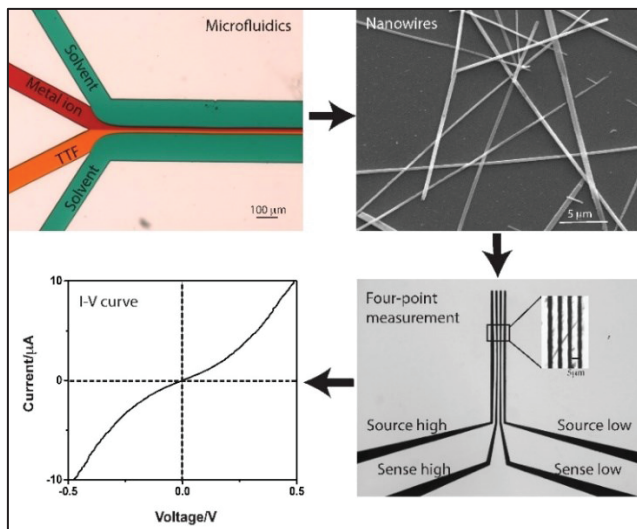


Figure 5.23. Graphic abstract of the synthesis and analysis of metal-TTF (derivatives). Nanostructures were firstly synthesized by microfluidic-based method with side streams, then the obtained structures were well characterized. For those which formed nano-/microwires, a single wire was aligned on microelectrodes for the conductivity measurement. Results on this work has been published in the peer-reviewed journal *Journal of Material Chemistry C* (2016, 4, 9235-9244, RSC publishing).

Single nanowire devices are the key materials in nanoelectronics and nanosensors.^{55,166,167} An increasing research interest has been focused on controlling the morphology and size distribution of nanostructures. In this project, the synthesis of various TTF-based nanowires is discussed.

As discussed in Chapter 1.2, TTF can react with transition metal ions to form charge-transfer complexes.¹⁶⁸⁻¹⁷⁰ In previous work, the charge-transfer between transition metal ions (Cu(II), Fe(III), Ru(III), Rh(III) *etc.*) and TTF derivatives has been studied, as well as the conductivity of their powder products.^{12,13,171} In addition, the formation of fibre structures formed from Au¹⁷² and Pb¹⁷³ with TTF and its derivative has been

reported. In TTF-based charge-transfer complexes, the mixed-valence state of TTF composed of neutral molecules and cation radicals has been proved.^{13,24} The common feature in all these structures is the stacking of the TTF units, with metal units coordinated to the sulphur atoms in the stacks.^{12,24,174} The morphology of these complexes is affected by metals, different TTF derivatives, as well as the experimental variables e.g. solvents, *etc.*

For the above mentioned TTF-based compounds (Cu-TTF, Fe-TTF, *etc.*), a systematic study is missing, in which the reaction products of the various combinations of metal precursors and TTF derivatives are thoroughly characterized. This detailed study on these parameters will be useful for the development of advanced single nanowire devices. In addition, nano-/microwires derived from metal-TTF charge-transfer compounds like Au-TTF, have been proved to act as sensing elements by fast electronic²⁸ or optical¹⁰⁰ readout. Thus, for further application purposes, it is of great importance to sort out the metal-TTF (and derivatives) which can easily form quasi-1D single wire structures under certain experimental conditions.

In this work, the microfluidic-guided synthesis of a series of TTF-based metal-organic structures by using variable transition metal ions and TTF derivatives in different solvents was carried out (Figure 5.23). The aim is to explore single nanowires with good conducting behaviour for novel advanced nanodevices. Transition metal ions and organic ligands which have TTF redox-active moieties were used. These reactions were performed on a microfluidic device,^{27,58,175} where the precursors reacted at the interface of two laminar streams. The so formed structures were characterized by SEM and optical microscopy, and the obtained fibres were further analysed by UV-Vis absorption, IR and Raman spectroscopy, elemental analysis, EDX and conductivity measurements. In addition, the effects of substitute groups of TTF derivatives on wire formation and conductive properties were compared and discussed.

5.3.1 Microfluidic guided synthesis of charge-transfer complexes

In this work, the microfluidic-guided synthesis of a series of TTF-based metal-organic structures on a four-inlet microchip by using variable transition metal ions and TTF derivatives is described. The aim is to explore the single nanowires with good conductivity behaviour for further

developing advanced nanodevices. Generally, metal ions (including Au(III), Cu(I), Cu(II), Fe(II), Fe(III), Co(II), Ni(II), Mn(II), Zn(II)) and TTF-based organic ligands (including TTF, FTTF, TET-TTF, TCE-TTF and BEDT-TTF), structures shown in Figure 5.24) were applied to the reaction. The two reactants were supplied from two middle channels, while solvents were introduced from side channels (at flow rate of 500;50;50;500 $\mu\text{L}/\text{min}$ for the four channels) (see Chapter 4.4 for experimental details). An overview of the metal salts, solvents, the morphologies of metal-TTF (and derivatives) obtained from bulk synthesis and microchips, as well as the single wire conductivity is given in Table 5.4. In the following, the major findings on the reaction of TTF with various metals, particularly Cu(II) and Fe(III) salts, are discussed. Finally, the results for the TTF derivatives are presented.

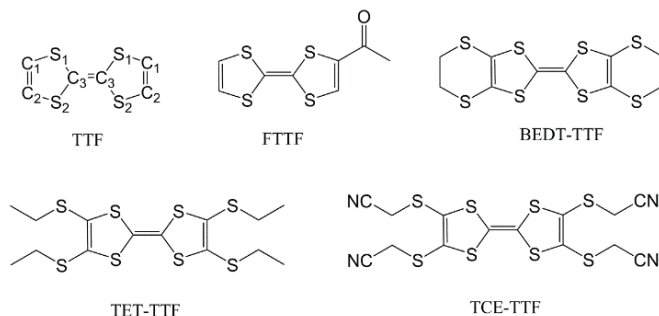


Figure 5.24. Chemical structures of TTF derivatives. The labelling of elements of TTF molecules refers to Reference 164.

Table 5.4. An overview of the main experimental parameters, morphology, conductivity and characterization of metal-TTF (and derivatives) complexes

σ refers to the conductivities of the specific measured single wires (see Figure 5.34 inset) at room temperature.

† Bulk results from this work; diameters of wires formed by microfluidics depend on the applied method; wire formed by diffusion ($\sim 2 \mu\text{m}$) conductivity was calculated from a previous work (Reference 28).

* For BEDT-TTF a two-solvent protocol was used, with metal salts in CH_3OH and BEDT-TTF in THF.

** n.a. not available

“-” means no result shown here.

5 Results and discussion

Metal salts	No.	Solvent	Compound Formula	Properties		$\sigma^{\#}$ S cm ⁻¹	Characterization of structures	Ref.
				diameter bulk [μm]	diameter μfluidic [μm]			
I. Tetrathiafulvalene (TTF)								
HAuCl ₄ †	1	CH ₃ CN	(TTFCl _{0.78})Au _{0.12}	0.41-4.43	0.2-2.0	0.021	SEM/ EDX-SEM/ UV-Vis/ IR/ EA (see Ref.)	24,27, 28,51, 100
CuCl ₂	2a	CH ₃ CN	(TTF) ₇ (CuCl ₂) ₃	0.75 ± 0.39 Fig. 5.25e_2a	0.31 ± 0.15 Fig. 5.25e_2a	1.13 Fig. 5.35a	SEM (Figs. 5.25b-d)/ EDX-SEM (Fig. 5.25f)/ UV-Vis (Fig. 5.31a)/ IR (Fig. 5.32)/ Raman (Fig. 5.33)/ EA (Table 5.5)	10,13, 171
	2b	CH ₃ OH	(TTF) ₂ CuCl ₂	0.91 ± 0.43 Fig. 5.25e_2b	0.69 ± 0.25 Fig. 5.25e_2b	0.34 Fig. 5.35b	SEM (Figs. 5.26a-b)/ EDX-SEM (Fig. 5.29a)/ UV-Vis (Fig. 5.31b)/ IR (Table 5.7)/ Raman (Fig. 5.33)/ EA (Table 5.5)	10,13, 171
Cu(NO ₃) ₂	3a	CH ₃ CN	(TTF) ₄ Cu(NO ₃) ₃	1.35 ± 0.67 Fig. 5.25e_3a	0.68 ± 0.27 Fig. 5.25e_3a	0.31 Fig. 5.35c	SEM (Figs. 5.26c-d)/ EDX-SEM (Figs. 5.29b)/ UV-Vis (Fig. 5.31b)/ IR (Fig. 5.32)/ Raman (Fig. 5.33)/ EA (Table 5.5)	10, 171
	3b	CH ₃ OH	(TTF) ₄ Cu(NO ₃) ₂	1.53 ± 0.41 Fig. 5.25e_3b	0.55 ± 0.22 Fig. 5.25e_3b	0.15 Fig. 5.35d	SEM (Figs. 5.26e-f)/ EDX- SEM (Fig. 5.29c)/ UV-Vis (Fig. 5.31b)/ IR (Table 5.7)/ Raman (Fig. 5.33)/ EA (Table 5.5)	10, 171
FeCl ₃	4a	CH ₃ CN	(TTF) ₅ FeCl ₃	3.82 ± 0.71 Fig. 5.25e_4a	0.93 ± 0.09 Fig. 5.25e_4a	0.11 Fig. 5.35e	SEM (Figs. 5.27a-b)/ EDX- SEM (Fig. 5.30a)/ UV-Vis (Fig. 5.31c)/ IR (Table 5.7)/ Raman (Fig. 5.33)/ EA (Table 5.5)	This work
	4b	CH ₃ OH	(TTF) ₅ FeCl ₃	1.35 ± 0.28 Fig.	0.32 ± 0.05 Fig.	0.40 Fig.	SEM (Figs. 5.27c-d)/ EDX-SEM (Fig.	12

5.3 Conductive single nanowires formed and analysed on microfluidic devices

				5.25e_4b	5.25e_4b	5.35f	5.30b)/ UV-Vis (Fig. 5.31c)/ IR (Table 5.7)/ Raman (Fig. 5.33)/ EA (Table 5.5)	
Fe(NO ₃) ₃	5a	CH ₃ CN	(TTF) ₃ Fe(NO ₃) ₃	6.05 ± 1.25 Fig. 5.25e_5a	0.83 ± 0.36 Fig. 5.25e_5a	0.35 Fig. 5.35g	SEM (Figs. 5.27e-f)/ EDX-SEM (Fig. 5.30c)/ UV-Vis (Fig. 5.31c)/ IR (Table 5.7)/ Raman (Fig. 5.33)/ EA (Table 5.5)	This work
	5b	CH ₃ OH	(TTF) ₃ Fe(NO ₃) ₃	1.51 ± 0.61 Fig. 5.25e_5b	0.82 ± 0.21 Fig. 5.25e_5b	0.53 Fig. 5.35h	SEM (Figs. 5.27g-h)/ EDX-SEM (Fig. 5.30d)/ UV-Vis (Fig. 5.31c)/ IR (Table 5.7)/ Raman (Fig. 5.33)/ EA (Table 5.5)	This work
Cu(I)Cl	6	CH ₃ CN	—	—	No structure Fig. 5.28a	—	UV-Vis Figs. 5.31e-f	This work
FeCl ₂	7	CH ₃ OH	—	Needles Fig. 5.28b	Needles Fig. 5.28c	—	UV-Vis Figs. 5.31e-f	This work
CoCl ₂	8	CH ₃ CN	—	—	No structure Fig. 5.28d	—	UV-Vis Figs. 5.31e-f	This work
Co(NO ₃) ₂	9	CH ₃ CN	—	Flake Fig. 5.28e	Particles (Fig. 5.28f)	—	UV-Vis Figs. 5.31e-f	This work
MnCl ₂	10	CH ₃ OH	—	—	Particles Fig. 5.28g	—	UV-Vis Figs. 5.31e-f	This work
NiCl ₂	11	CH ₃ OH	—	Particles Fig. 5.28h	Particles Fig. 5.28i	—	UV-Vis Figs. 5.31e-f	This work
Ni(NO ₃) ₂	12	CH ₃ CN	—	Particles Fig. 5.28j	Particles/ needles Fig. 5.28k	—	UV-Vis Figs. 5.31e-f	This work
ZnCl ₂	13	CH ₃ CN	—	Particles Fig. 5.28l	Particles Fig. 5.28m	—	UV-Vis Figs. 5.31e-f	This work
Zn(NO ₃) ₂	14	CH ₃ CN	—	Rods Fig. 5.28n	Needles Fig. 5.28o	—	UV-Vis Figs. 5.31e-f	This work
II. 2-formyl-tetrathiafulvalene (FTTF)								

5 Results and discussion

HAuCl ₄	15	CH ₃ CN	(FTTF) ₃ AuCl ₃	Dendrites Fig. 5.37a	0.26 ± 0.14 Fig. 5.37c	0.66 Fig. 5.41c	EDX-SEM (Fig. 5.40a)/ UV-Vis (Fig. 5.36a)/ IR (Fig. 5.39a)/ EA (Table 5.8)	This work
CuCl ₂	16	CH ₃ CN	(FTTF) ₂ CuCl ₂	Dendrites Fig. 5.37d	0.20 ± 0.08 Fig. 5.37f	0.84 Fig. 5.41d	EDX-SEM (Fig. 5.40b)/ UV-Vis (Fig. 5.36a)/ IR (Fig. 5.39b)/ EA (Table 5.8)	This work
Cu(NO ₃) ₂	17	CH ₃ CN	—	Clusters Fig. 5.38a	Particles Fig. 5.38c	—	UV-Vis Fig. 5.36a	This work
Fe(NO ₃) ₃	18	CH ₃ OH	—	Clusters Fig. 5.38d	Particles Fig. 5.38f	—	UV-Vis Fig. 5.36b	This work
FeCl ₃	19	CH ₃ OH	—	Dendrites Fig. 5.38g	Dendrites Fig. 5.38i	—	UV-Vis Fig. 5.36b	This work
FeCl ₂	20	CH ₃ OH	—	FTTF Dendrites Fig. 5.38j	Dendrites Fig. 5.38k	—	UV-Vis Fig. 5.36c	This work
ZnCl ₂	21	CH ₃ CN	—	FTTF Crystals Fig. 5.38l	Particles Fig. 5.38m	—	UV-Vis Fig. 5.36c	This work
Zn(NO ₃) ₂	22	CH ₃ CN	—	FTTF Crystals Fig. 5.38n	Particles Fig. 5.38o	—	UV-Vis Fig. 5.36c	This work
III. Bis(ethylenedithio)tetrathiafulvalene (BEDT-TTF)*								
HAuCl ₄	23	CH ₃ OH -THF	—	1.73 ± 0.61 Fig. 5.44a	0.56 ± 0.12 Fig. 5.45a	6.3×10 ⁻³ Fig. 5.47a	SEM (5.46a)/ UV-Vis (Fig. 5.43a)/ EDX-SEM (Fig. 5.48b)	172
CuCl ₂	24	CH ₃ OH -THF	(BEDTTTF) _{1.5} Cu Cl ₂	1.79 ± 0.31 Fig. 5.44b	0.59 ± 0.14 Fig. 5.46a	n.a.** Fig. 5.46b	SEM (5.47a)/ UV-Vis (Fig. 5.43b)	174, 176, 177
Cu(NO ₃) ₂	25	CH ₃ OH -THF	—	3.16 ± 0.82 Fig. 5.44c	2.11 ± 0.53 Fig. 5.45b	4.8×10 ⁻³ Fig. 5.47b	SEM (5.46b)/ UV-Vis (Fig. 5.43b)/ EDX-SEM (Fig. 5.48c)	This work

FeCl ₃	26	CH ₃ OH -THF	—	1.68 ± 0.95 Fig. 5.44d	0.50 ± 0.12 Fig. 5.46c	n.a.** Fig. 5.46d	SEM (5.47c)/ UV- Vis (Fig. 5.43c)	This work
Fe(NO ₃) ₃	27	CH ₃ OH -THF	—	1.29 ± 0.59 Fig. 5.44e	0.47 ± 0.11 Fig. 5.45c	1.2×10 ⁻² Fig. 5.47c	SEM (5.46c)/ UV- Vis (Fig. 5.43c)/ EDX-SEM (Fig. 5.48d)	This work
IV. Tetrakis(ethylthio)tetrathiafulvalene (TET-TTF)								
HAuCl ₄	28	CH ₃ CN	—	Crystals Fig. 5.42a	—	—	—	This work
CuCl ₂	29	CH ₃ CN	—	Crystals Fig. 5.42b	—	—	—	This work
V. 2,3,6,7-Tetrakis(2-cyanoethylthio) tetrathiafulvalene (TCE-TTF)								
HAuCl ₄	30	CH ₃ CN	—	Crystals Fig. 5.42c	—	—	—	This work

5.3.2 Metal-TTF complexes

a) Synthesis and analysis by optical microscopy and SEM

Figure 5.25a shows exemplary the reaction of CuCl₂ and TTF carried out on a microdevice by supplying the two reactant solutions through channels B and C both at flow rates of 50 µL/min. The solvent, here CH₃CN, was supplied through channels A and D. The solvent streams with a flow rate of 500 µL/min focused the inner streams to a narrow reaction zone.²⁷ The reaction to (TTF)₇(CuCl₂)₃ (**2a**) occurred immediately as can be seen by the black product in Figure 5.25a. The structures were flushed out of the channel and observed by SEM (Figure 5.25b). For comparison, the reaction in a two-inlet microchip, i.e. without sheath flows (Figure 5.25c), and a standard glass flask (Figure 5.25d) was also carried out. As can be seen from the SEM images (Figure 5.25b), the reaction in the four-inlet microdevice yielded the longest fibres with a smaller diameter than those obtained by the other approaches (Figures 5.25c and 5.25d). The four-inlet microfluidic chip is preferred in the following because it provides a defined interface between the two laminar flowing precursor streams and confines the reaction zone by use of the sheath flow. The wires assemble in this reaction zone

in direction of the flow. Furthermore, this chip design has the benefits that the wires are flushed out immediately and do not block the channel. Once outside, they are immediately diluted and do not react further.

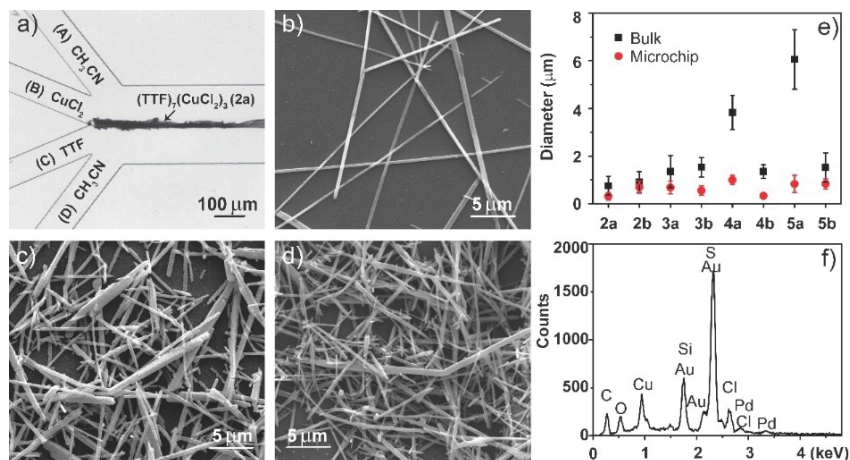


Figure 5.25. Synthesis of wires, exemplary for $(\text{TTF})_7(\text{CuCl}_2)_3$ (**2a**). a) Optical micrograph of the four inlet microchip. Wire bundles are formed at the interface of the CuCl_2 (channel B, flow rate $50 \mu\text{L}/\text{min}$) and TTF solutions (channel C, flow rate $50 \mu\text{L}/\text{min}$) in CH_3CN . The solvent was also used as sheath flow, supplied from channel A and D, at flow rates of $500 \mu\text{L}/\text{min}$. b) SEM image of wire structures obtained on the four-inlet microchip. c) and d) are SEM images of wire structures obtained by two-inlet chip (flow rates of $100;100 \mu\text{L}/\text{min}$) and bulk synthesis. e) is the comparison of the diameters (μm) of wires obtained from different M-TTF complexes synthesized in bulk (black square) and on four-inlet microchips (red dot). The average diameter and standard deviation were obtained from ten different wires for each complex. For the compounds in the horizontal axis (**2a**, **2b**, **3a**, **3b**, **4a**, **4b**, **5a**, **5b**), refer to numbers in Table 5.4 (column 2). f) EDX-SEM spectrum of **2a**.

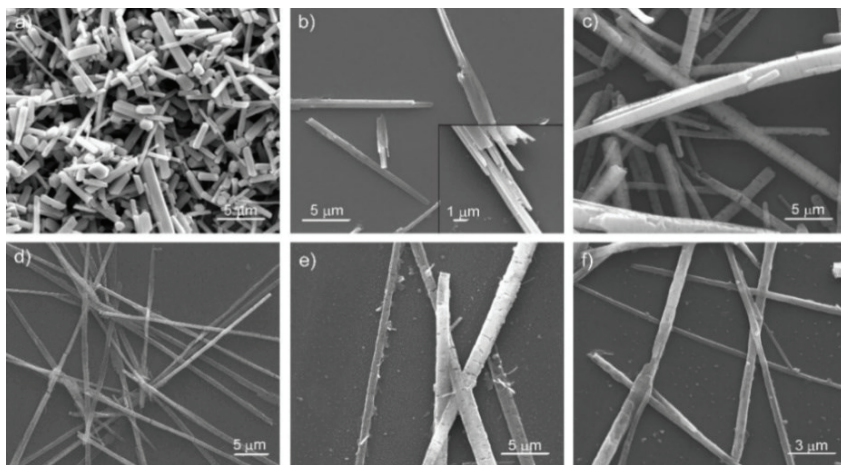


Figure 5.26. SEM images of $(\text{TTF})_2\text{CuCl}_2$ (**2b**), $(\text{TTF})_4\text{Cu}(\text{NO}_3)_2$ (**3a**) and $(\text{TTF})_4\text{Cu}(\text{NO}_3)_2$ (**3b**). **2b** generated a) by bulk synthesis and b) on four-inlet microchip. (Figure b inset is a magnified image of the end of a needle structure showing bundles of wires). c) and d) SEM images of **3a** generated by bulk synthesis and on microchip in CH_3CN . e) and f) SEM images of **3b** generated by bulk synthesis and on microchip. The numbers of compounds are in accordance with the numbers in Table 5.4.

The morphology of structures obtained from the reaction of TTF with $\text{Cu}(\text{II})$ and $\text{Fe}(\text{III})$ salts was studied (**2b**, **3a**, **3b**, **4a**, **4b**, **5a**, **5b**), which showed clearly differences between bulk synthesis and four-inlet microchips (Figure 5.25e, SEM images in Figures 5.26 and 5.27). All the wires resulted from the four-inlet microchip are in nanometre range and smaller than from the bulk synthesis, confirming that microfluidic synthesis is an advanced tool to control the formation of nanostructures.

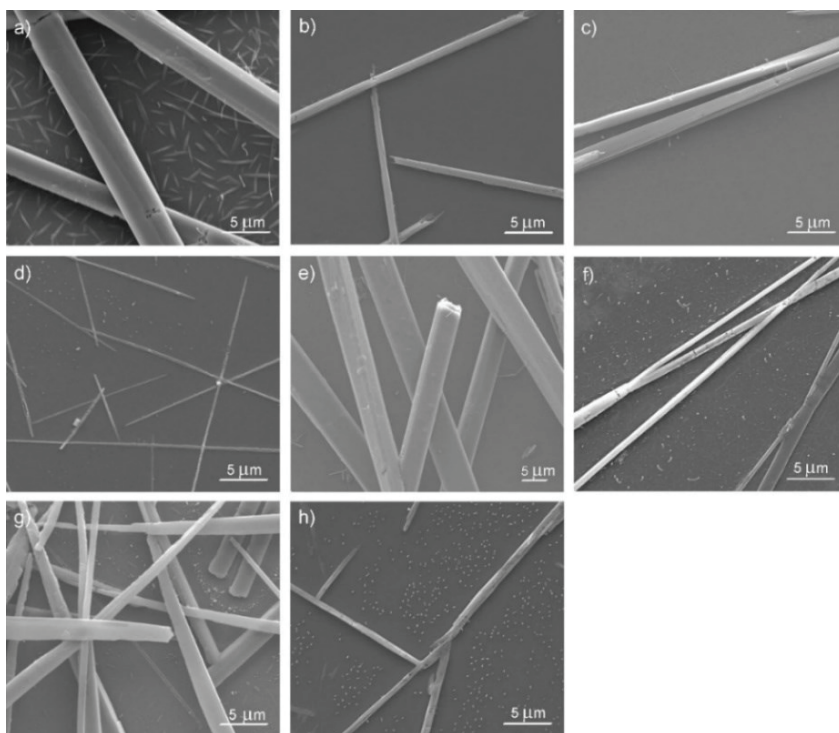


Figure 5.27. SEM images of $(\text{TTF})_5\text{FeCl}_3$ (**4a**), $(\text{TTF})_5\text{FeCl}_3$ (**4b**), $(\text{TTF})_5\text{Fe}(\text{NO}_3)_3$ (**5a**) and $(\text{TTF})_5\text{Fe}(\text{NO}_3)_3$ (**5b**). a) and b): **4a** formed in bulk synthesis and on four-inlet microchip. c) and d): **4b** formed in bulk and on microchip. e) and f): **5a** generated by bulk synthesis and on microchip. g) and h): **5b** generated by bulk synthesis and on microchip. The numbers of compounds are in accordance with the numbering in Table 5.4.

In addition, the products of reactions between TTF and other metal salts including CuCl (**6**), FeCl_2 (**7**), CoCl_2 (**8**), $\text{Co}(\text{NO}_3)_2$ (**9**), MnCl_2 (**10**), NiCl_2 (**11**), $\text{Ni}(\text{NO}_3)_2$ (**12**), ZnCl_2 (**13**) and $\text{Zn}(\text{NO}_3)_2$ (**14**) were investigated by optical microscopy. Here, the products showed various morphologies (e.g. particles, crystals, mixtures of particles and needles, *etc.*), while not uniform 1D nano-/microstructures (Figure 5.28).

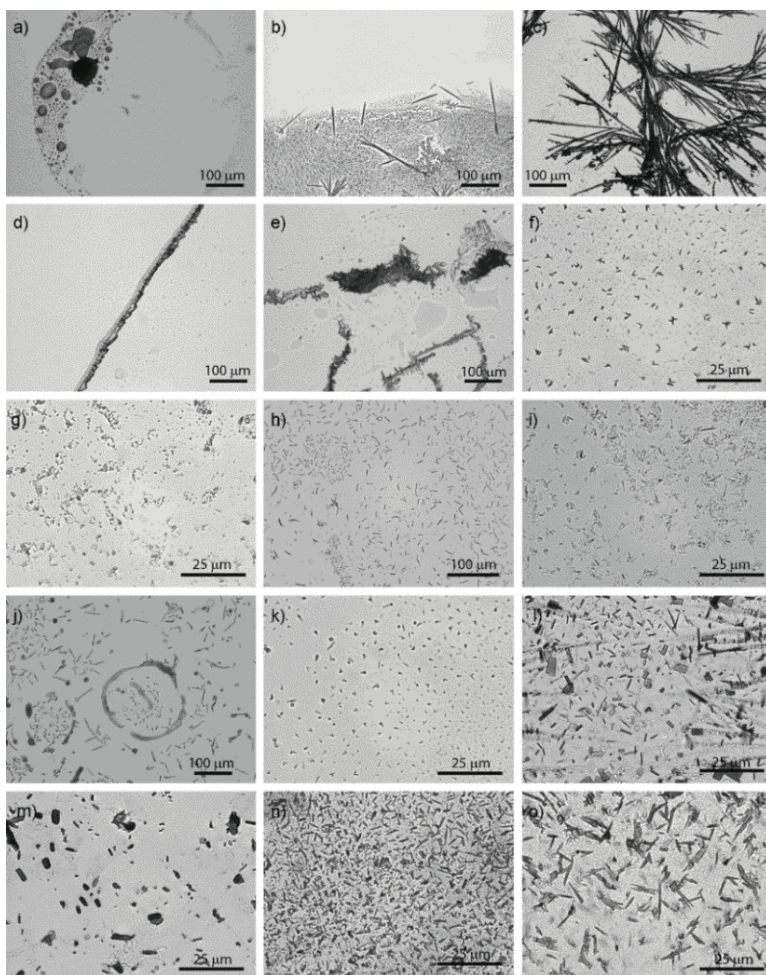


Figure 5.28. Optical images of products derived from compounds **6**, **7**, **8**, **9**, **10**, **11**, **12**, **13**, **14**. a) CuCl-TTF (**6**) formed on four-inlet microchip, no obvious structures; FeCl₂-TTF (**7**) formed b) in bulk, mixture of needle and small particles, and c) on two-inlet microchip, large branches of orange crystals; d) CoCl₂-TTF (**8**) on four-inlet microchip, no obvious structures; Co(NO₃)₂ (**9**) formed e) in bulk, flakes and f) on four-inlet microchip, particles; g) MnCl₂-TTF (**10**) on four-inlet microchip, particles; NiCl₂-TTF (**11**) formed h) in bulk, mixture of small rods segments and particles, and i) on microchip, particles; Ni(NO₃)₂-TTF (**12**) formed j) in bulk,

mixture of small rods and particles, and k) on four-inlet microchip, particles; $\text{ZnCl}_2\text{-TTF}$ (**13**) formed l) in bulk, mixture of crystals, rods and particles, and m) on two-inlet microchip, large particles; $\text{Zn}(\text{NO}_3)_2\text{-TTF}$ (**14**) formed n) in bulk, cluster of small rods and particles, and o) on two-inlet microchip, needles and crystals. The numbers of compounds are in accordance with the numbering in Table 5.4.

b) EDX and elemental (CHN) analysis

To determine the elemental composition of the nanowires obtained from microchips, EDX spectroscopy was performed. The spectrum of **2a** (Figure 5.25f) clearly showed C, Cu, S, Cl elements, indicating that the nanowires are composed of CuCl_2 and TTF ($\text{C}_6\text{H}_4\text{S}_4$). The results for the other Cu(II) salts are depicted in Figure 5.29, which proved the composition of CuCl_2 and TTF for **2b** (Figure 5.29a), as well as the composition of $\text{Cu}(\text{NO}_3)_2$ and TTF for **3a** (Figure 5.29b) and **3b** (Figure 5.29c). The EDX spectra of Fe(III) salts are shown in Figure 5.30, which also proved the composition of FeCl_3 and TTF for **3a** (Figure 5.30a) and **3b** (Figure 5.30b), and the composition of $\text{Fe}(\text{NO}_3)_3$ and TTF for **3c** (Figure 5.30c) and **3d** (Figure 5.30d).

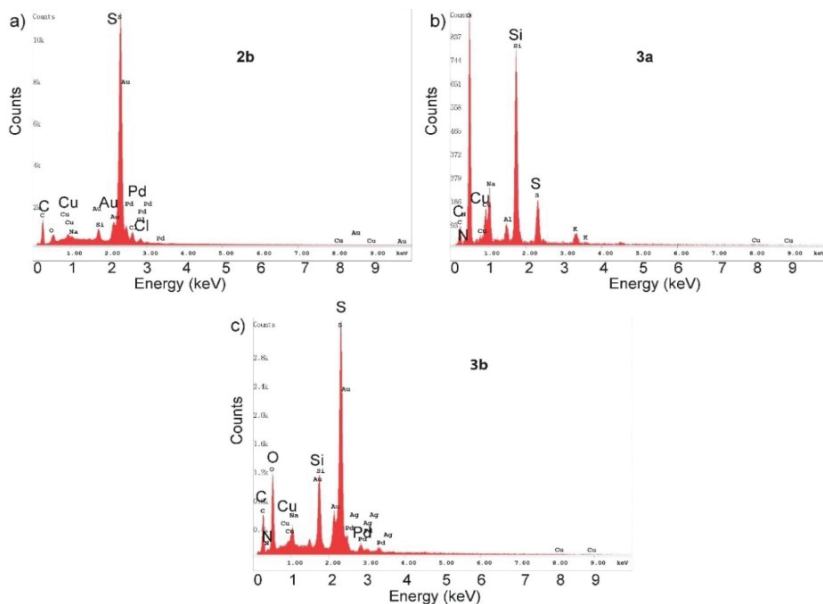


Figure 5.29. EDX-SEM spectra of $(\text{TTF})_2\text{CuCl}_2$ (**2b**), $(\text{TTF})_4\text{Cu}(\text{NO}_3)_2$ (**3a**) and $(\text{TTF})_4\text{Cu}(\text{NO}_3)_2$ (**3b**). Note the existence of Cu and Cl in a) and the existence of N and Cu in c) and d). The small peaks of N was due to its low percentage in the complexes.

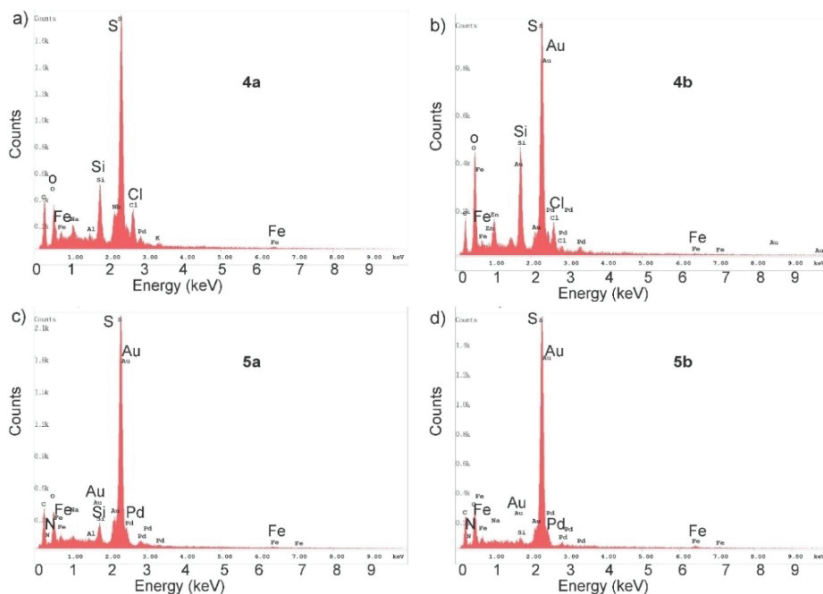


Figure 5.30. EDX-SEM spectra of $(\text{TTF})_5\text{FeCl}_3$ (**4a**), $(\text{TTF})_5\text{FeCl}_3$ (**4b**), $(\text{TTF})_5\text{Fe}(\text{NO}_3)_3$ (**5a**) and $(\text{TTF})_5\text{Fe}(\text{NO}_3)_3$ (**5b**). Note the existence of Fe and Cl in a) and b), the existence of N and Fe in c) and d). The small peaks of N was due to its low percentage in the complexes.

To get the formula of the above-mentioned TTF-based compounds, elemental analysis (CHN) was performed. The results are summarized in Table 5.5, which confirmed the chemical composition of the nanostructures of **2a**, **2b**, **3a**, **3b**, **4a**, **4b**, **5a** and **5b**, quantitatively. The compound formula are in accordance with reported work for bulk synthesized compounds obtained using the same metal salts and solvents.

Table 5.5. Elemental analysis of compounds **2a**, **2b**, **3a**, **3b**, **4a**, **4b**, **5a** and **5b**

Metal salts	Solvent	No.	Anal. % found (calculated)			Compound Formula
			C	H	N	
CuCl ₂	CH ₃ CN		28.21	1.53		(TTF) ₇ (CuCl ₂) ₃
		2a	(27.51)	(1.54)		
CuCl ₂	CH ₃ OH		27.20	1.57		(TTF) ₂ CuCl ₂
		2b	(26.54)	(1.48)		
Cu(NO ₃) ₂	CH ₃ CN		28.98	1.77	3.50	(TTF) ₄ Cu(NO ₃) ₂
		3a	(28.68)	(1.60)	(2.79)	
Cu(NO ₃) ₂	CH ₃ OH		26.88	1.58	2.88	(TTF) ₄ Cu(NO ₃) ₂
		3b	(28.68)	(1.60)	(2.79)	
FeCl ₃	CH ₃ CN		30.91	2.23		(TTF) ₅ FeCl ₃
		4a	(30.43)	(1.70)		
FeCl ₃	CH ₃ OH		29.99	2.00		(TTF) ₅ FeCl ₃
		4b	(30.43)	(1.70)		
Fe(NO ₃) ₃	CH ₃ CN		28.77	1.81	3.52	(TTF) ₅ Fe(NO ₃) ₃
		5a	(28.52)	(1.60)	(3.32)	
Fe(NO ₃) ₃	CH ₃ OH		28.54	1.81	3.37	(TTF) ₅ Fe(NO ₃) ₃
		5b	(28.52)	(1.60)	(3.32)	

c) UV-Vis spectroscopy

The eluted solution from the chips after reaction were diluted and directly applied for UV-Vis investigations. Three conclusions can be drawn from the UV-Vis spectra analysis. Firstly, the electron transfer between metal ions and TTF happened after reaction: as indicated in Figure 5.31a, TTF has a weak absorbance at 436 nm, while CuCl₂ only shows negligible absorption signal. In comparison, the spectrum of eluted solution of **2a** exhibits an intense band at 436 nm and a new absorption band at 580 nm, which indicates the existence of TTF radical cation, due to the electron transfer from TTF to Cu²⁺.^{26,171} Secondly, there is an influence from solvents on the electron transfer reaction. The absorption spectra of the complexes (**2b**, **3a**, **3b**, **4a**, **4b**, **5a**, **5b**) at 580 nm are summarized in Figure 5.31b, which indicating the electron transfer between TTF and Cu(II), as well as that of TTF and Fe(III) (Figure 5.31c). No interferences on absorption from metal ions (Figure 5.31d). However, the differences in absorption intensities clearly shows that Cu(II) is more powerful oxidizing agent in CH₃CN than in CH₃OH (Figures 5.31a and Figure 5.31b, A_{2a}>A_{3a}>A_{2b}>A_{3b}), while Fe(III) showing higher oxidative ability in

CH_3OH than in CH_3CN (Figure 5.31c, $A_{5b} > A_{5a} > A_{4b} > A_{4a}$). This is in accordance with reported work.^{10,178}

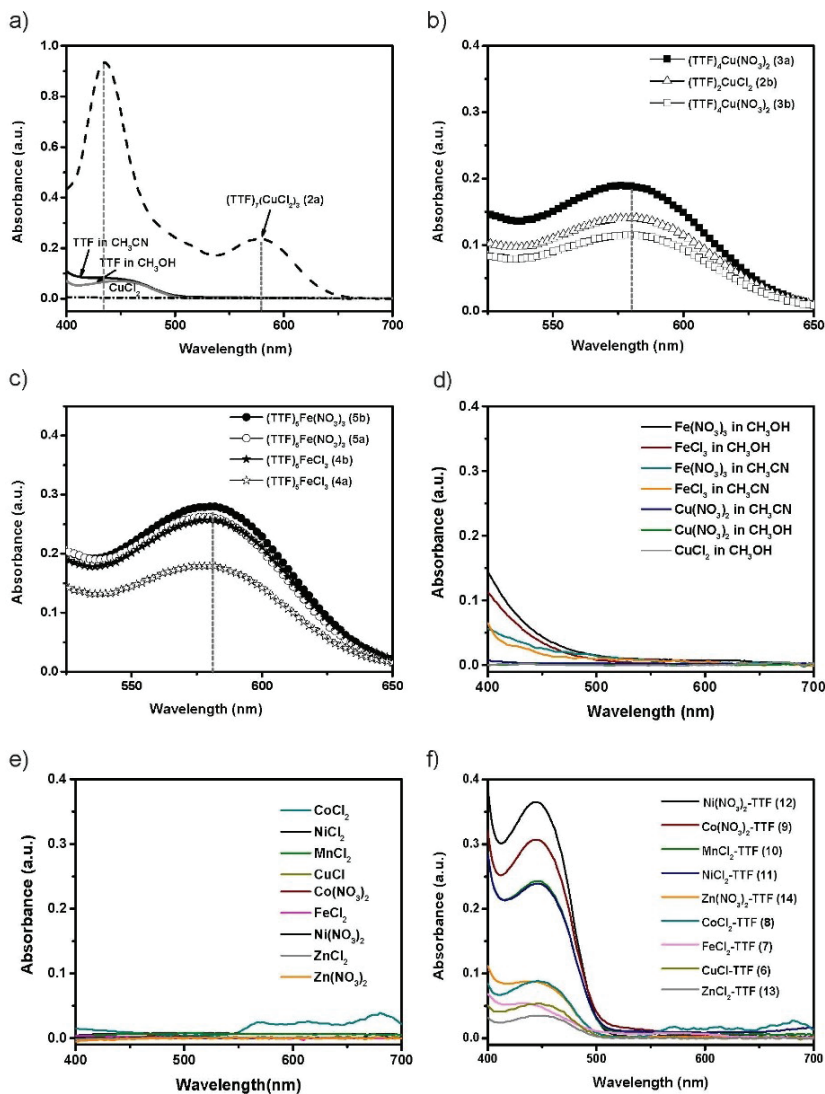


Figure 5.31. UV-Vis absorption spectra of solutions of 2a, 2b, 3a, 3b, 4a, 4b, 5a, 5b, 6,

7, 8, 9, 10, 11, 12, 13 and 14. a) CuCl_2 in CH_3CN (0.06 mM), TTF in CH_3CN and CH_3OH (both are 0.24 mM) and the solution after the reaction of CuCl_2 and TTF in CH_3CN . A new absorption band at 580 nm ($A = 0.237$) appeared after formation of the complex **2a**. Dash lines indicated the position of 436 nm and 580 nm. The absorption band at 580 nm of different charge-transfer complexes in different solvents: b) **3a** ($A = 0.189$), **2b** ($A = 0.141$) and **3b** ($A = 0.115$); c) **5b** ($A = 0.28$), **4b** ($A = 0.257$), **5a** ($A = 0.262$) and **4a** ($A = 0.179$); d) Fe(III) and Cu(II) salts in CH_3CN and CH_3OH ; e) metal salts of Cu(I), Fe(II), Co(II), Mn(II), Ni(II), Zn(II); f) solution after the reaction of TTF and metal ions in e). **6, 7, 8, 9, 10, 11, 12, 13, 14.** The final concentrations of all metal salts were 0.06 mM. The elutes of microreactions were diluted to approx. 0.06 mM. Dash lines in Figures b) and c) indicated the position of 580 nm. The numbering of compounds are in accordance with the numbers in Table 5.4.

Thirdly, the influence of various metals ions and different oxidize state of the same metal ions on the electron transfer was understood. For the precursors of Cu(I), Fe(II), Co(II), Mn(II), Ni(II), Zn(II) ions and the products after their reactions with TTF, only negligible absorptions were observed at 580 nm (Figures 5.31e and 5.31f). Following, a comparison of the spectra from different oxidised states of the same metal was performed. In contrast to the spectra of solutions resulted from Cu(II) and TTF (**2a**, **2b**, Figures 5.31a and 5.31b), the spectrum of Cu(I) and TTF exhibits no obvious absorbance at 580 nm (**6**, Figure 5.31f). Similar results were observed for the spectra of solutions from Fe(III) and TTF (**4a**, **4b**, Figure 5.31c), and that of Fe(II) and TTF (**7**, Figure 5.31f). Thus, only higher oxidised state of Cu(II) and Fe(III) can lead to the electron transfer from TTF to corresponding metal ions in the experimental conditions applied in this work.

d) IR spectroscopy

The IR spectra were obtained for the M-TTF complexes which formed wire structures. Table 5.6 shows the typical IR vibrations of neutral TTF and TTF cation.

Table 5.6. IR assignments of TTF⁰ and TTF⁺*

Vibrational modes*	TTF ⁰	TTF ⁺
ν_{23} CCH bend	1254 cm ⁻¹	1237 cm ⁻¹
ν_{15} CCH bend	1090 cm ⁻¹	1072 cm ⁻¹
ν_{16} C-S stretch	781 cm ⁻¹	836 cm ⁻¹
ν_{25} ring SCC bend	794 cm ⁻¹	825 cm ⁻¹
ν_{17} C-S stretch	734 cm ⁻¹	751 cm ⁻¹

* The symmetry species numbers (ν_{23} , ν_{15} , ν_{16} , ν_{25} , ν_{17}) see literature.¹⁷⁹

As shown in the IR spectrum of **2a** (Figure 5.32, **2a**), modes at 1242 cm⁻¹ (ν_{23} , CCH bend), 1082 cm⁻¹ (ν_{15} , CCH bend), 814 cm⁻¹ (ν_{16} , CS stretch), 804 cm⁻¹ (ν_{25} , SCC bend), 740 cm⁻¹ (ν_{17} , CS stretch) are all between the IR vibrations for TTF⁰ molecules and TTF⁺ cations (Table 5.6). Such IR spectrum indicates the mixed-valence state of this TTF-based material in the neutral and cation radical states.^{13,179} Similar TTF bands were also observed for **3a** at 1245 cm⁻¹ (ν_{23} , CCH bend), 817 cm⁻¹ (ν_{16} , CS stretch) and 733 cm⁻¹ (ν_{17} , CS stretch) (Figure 5.32). The observed peak at 1312 cm⁻¹ indicated the existence of nitrate.^{10,180} which formed anion columns in the resulted structures. In addition, the mixed-valence state of neutral and TTF cations in other TTF-based complexes (**2b**, **3a**, **3b**, **4a**, **4b**, **5a**, **5b**) was also confirmed by their IR spectral modes (Table 5.7). Thus, similar structures were formed for these M-TTF wires, with a backbone scaffold of TTF neutral and cation radicals stabilized with counter ions forming the 1D nanowires. To further prove the TTF components in the nanostructures, confocal Raman measurements were performed. Raman peaks at around 500 cm⁻¹ and 1420 cm⁻¹ (Figure 5.33) were observed, similarly to the spectra of Au-TTF (**1**) in previous works.^{51,100} The difference between **1** and the complexes (**2b**, **3a**, **3b**, **4a**, **4b**, **5a**, **5b**) is that in the former structure Au(III) ions were reduced to Au⁰,²⁴ while in the latter structures, metal ions existed as low oxidized Cu(I) and Fe(II) when excess TTF was used. The common features of these donor-acceptor complexes structures are firstly the mix-valence state of TTF stacking, and secondly the coordinated metal (Au⁰)²⁴ and metal ion (Cu(I) and Fe(II)) to the sulphur atoms in the TTF stacks.¹²

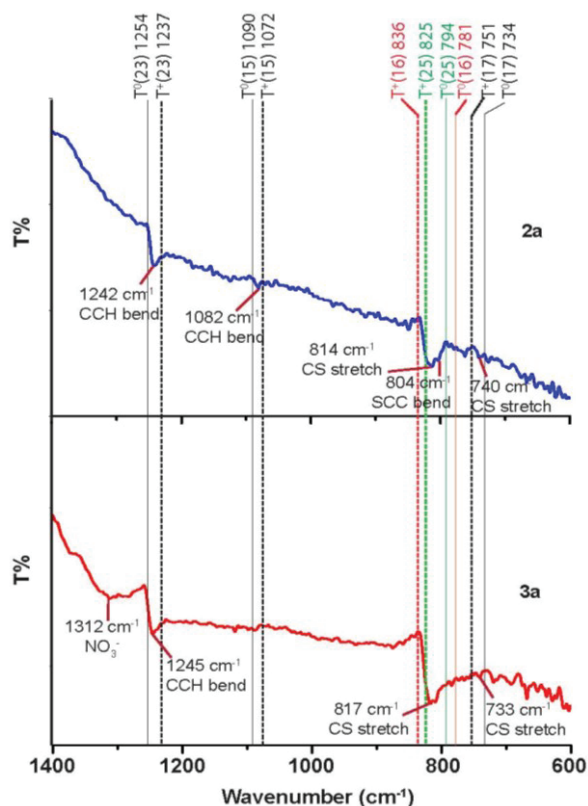


Figure 5.32. IR spectra of compounds (TTF)₇(CuCl₂)₃ (**2a**) and (TTF)₄Cu(NO₃)₂ (**3a**). In the spectrum of **2a**, characteristic vibration modes at 1242 cm⁻¹ (ν_{23} , CCH bend), 1082 cm⁻¹ (ν_{15} , CCH bend), 814 cm⁻¹ (ν_{16} , CS stretch), 804 cm⁻¹ (ν_{25} , SCC bend), 740 cm⁻¹ (ν_{17} , CS stretch) are shown. In the spectrum of **3a**, typical bands were observed at 1245 cm⁻¹ (ν_{23} , CCH bend), 817 cm⁻¹ (ν_{16} , CS stretch) and 733 cm⁻¹ (ν_{17} , CS stretch), the peak at 1312 cm⁻¹ indicates the presence of nitrate (NO₃⁻). Products were obtained on four-inlet microchips. The wavenumbers of the different vibrational bands are shown for TTF⁰ (T⁰, solid line) and its cation TTF⁺ (T⁺, dash line). The numbering of all the IR vibrational modes is given in reported work.^{13,179}

Table 5.7. IR assignments of other M-TTF compounds **2b**, **3b**, **4a**, **4b**, **5a** and **5b**

Comp- ound	IR spectra* (cm ⁻¹)					
	NO ₃ ⁻	<i>ν</i> ₂₃ , CCH bend	<i>ν</i> ₁₅ , CCH bend	<i>ν</i> ₁₆ , CS stretch	<i>ν</i> ₂₅ , SCC bend	<i>ν</i> ₁₇ , CS stretch
2b		1245	1078	814	803	
3b	1319	1247		820		
4a		1243	1076	823	800	743
4b		1236	1076	823		
5a	1318	1243		827		
5b	1314	1247		818		

Notes: Compounds were obtained on four-inlet chips. The numbers of compounds are in accordance with the numbers in Table 5.4.

*The numbering of the vibrational modes is given in literature.^{13,179} The IR spectra information of nitrate is given in literature.¹⁸⁰

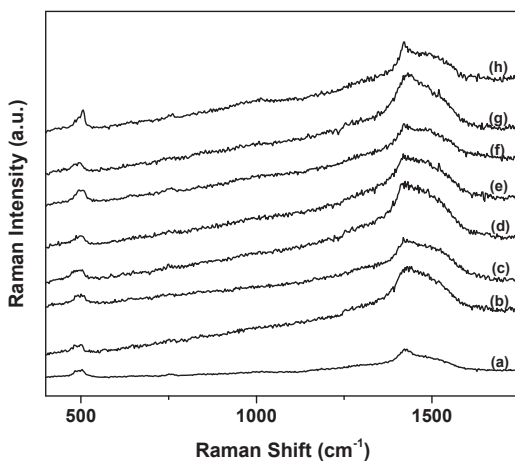


Figure 5.33. Raman spectra of compounds **2a**, **2b**, **3a**, **3b**, **5a**, **5b**, **4a**, and **4b** at 532 nm excitation. (a) **2a** (b) **2b**, (c) **3a**, (d) **3b**, (e) **5a**, (f) **5b** (g) **4a**, (h) **4b**. The Raman peaks at around 500 cm⁻¹ and 1420 cm⁻¹.

e) Electrical properties

It has been reported that partially charged TTF salts exhibit higher electrical conductivity than simple salts at room temperature.¹⁷⁹ Thus, nanowires obtained from M-TTF were used to address conductivity via four-point probe measurements by aligning a single nanowire on pre-fabricated microelectrodes. I - V curves of these complexes were obtained by measuring the source-drain voltage, while sweeping the applied source-drain current at room temperature. As shown in Figure 5.34, the I - V curves for **2b**, **3a**, **3b**, **4a**, **4b**, **5a** and **5b** are non-linear. It can be assumed as an indication of the non-perfect contact, as the nanowires were simply aligned on the microelectrodes, without topside metallization. A similar conductive behaviour of **1** was observed in previous work.²⁸ Different voltage ranges were observed for different nanowires with various diameters and lengths when the same current was applied. Thus, a comparison of the linear conductance of all the I - V curves in Figure 5.34 was made and shown in Figure 5.35. The results indicated that all the nanowires exhibited high electrical conductivities from 10^{-1} to 10 S cm⁻¹ at room temperature (Figure 5.35). In particular, **2a** showed the highest conductivity ($\sigma = 1.13$ S cm⁻¹), followed by **5b** ($\sigma = 0.53$ S cm⁻¹) and **4b** ($\sigma = 0.40$ S cm⁻¹).

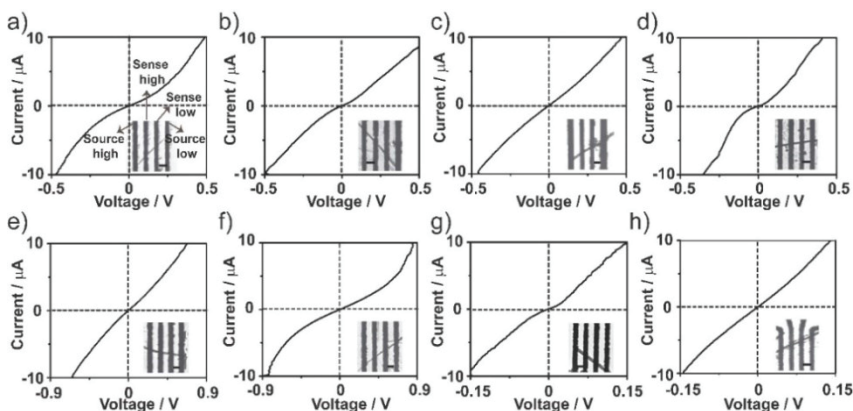


Figure 5.34. Representative I - V curves of single nanowires of M-TTF complexes. The curves were obtained by four-point measurements (the two outer microelectrodes represent source high and source low, while the two inner electrodes represent sense high

and sense low). a) $(\text{TTF})_7(\text{CuCl}_2)_3$ in CH_3CN (**2a**), b) $(\text{TTF})_2\text{CuCl}_2$ in CH_3OH (**2b**), $(\text{TTF})_4\text{Cu}(\text{NO}_3)_2$ in c) CH_3CN (**3a**) and in d) CH_3OH (**3b**), $(\text{TTF})_5\text{FeCl}_3$ in e) CH_3CN (**4a**) and in f) CH_3OH (**4b**), $(\text{TTF})_5\text{Fe}(\text{NO}_3)_3$ in g) CH_3CN (**5a**) and in h) CH_3OH (**5b**). Figure insets show the alignment of single nanowires on the four microelectrodes, all the electrodes connected to the source meter. The gaps between electrodes (scale bars) are 5 μm .

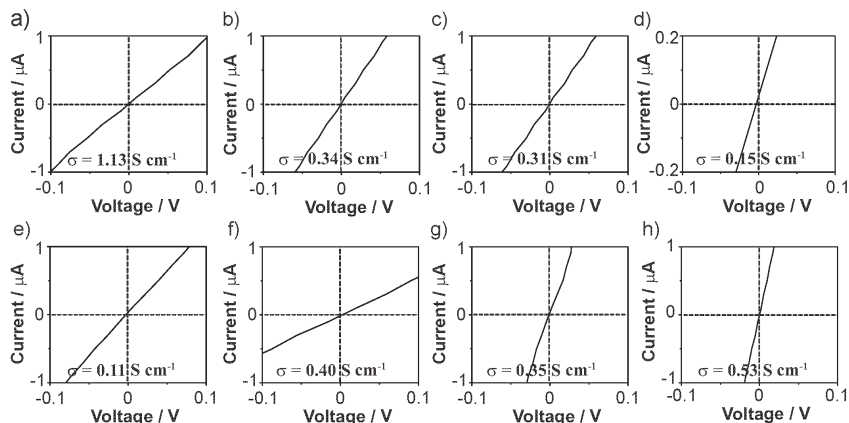


Figure 5.35. Linear range of the I - V curves in Figure 5.34 with the electrical conductivities of single nanowires of **2a**, **2b**, **3a**, **3b**, **4a**, **4b**, **5a** and **5b**. a) **2a**, $\sigma = 1.13 \text{ S cm}^{-1}$, b) **2b**, $\sigma = 0.34 \text{ S cm}^{-1}$; c) **3a**, $\sigma = 0.31 \text{ S cm}^{-1}$; d) **3b**, $\sigma = 0.15 \text{ S cm}^{-1}$ (here the I - V curve showed linearity between $-0.02 \mu\text{A}$ and $0.02 \mu\text{A}$); e) **4a**, $\sigma = 0.11 \text{ S cm}^{-1}$; f) **4b**, $\sigma = 0.40 \text{ S cm}^{-1}$; g) **5a**, $\sigma = 0.35 \text{ S cm}^{-1}$; h) **5b**, $\sigma = 0.53 \text{ S cm}^{-1}$. σ refers to the conductivity at room temperature.

Thus, with the so proposed characterization technique, it was possible to measure the conductivities of single nanowires, for which the non-linear curve were caused by contact effects between the wire and microelectrodes, while the linear parts of I - V curves show typical ohmic behaviour (Figure 5.35). In addition, the electron transfer of TTF to metal ions and conductive behaviour of induced fibres were influenced by the solvent used in the system.

5.3.3 Metal-FTTF complexes

Further studies on the reaction between transition metal salts and commercially available TTF derivatives were conducted. FTTF, consisting of an aldehyde functional group at the C₁ substitution of TTF unit, was further explored. The reactions of FTTF with HAuCl₄, Cu(II) and Zn(II) salts were performed in CH₃CN, while the reaction with Fe(III) salts in CH₃OH.

a) UV-Vis spectroscopy

In the UV-Vis spectral analysis of M-FTTF (Figure 5.36), compared to pure FTTF (Figures 5.36a and 5.36b), all the spectra for compounds **15**, **16**, **17**, **18** and **19** exhibited the absorption at 437 nm and 580 nm, suggesting a charge-transfer between these metal ions and FTTF. However, in the reaction of Zn(II), Fe(II) with FTTF (Figure 5.36c, **20**, **21**, **22**), no peaks at 437 nm or 580 nm were observed.

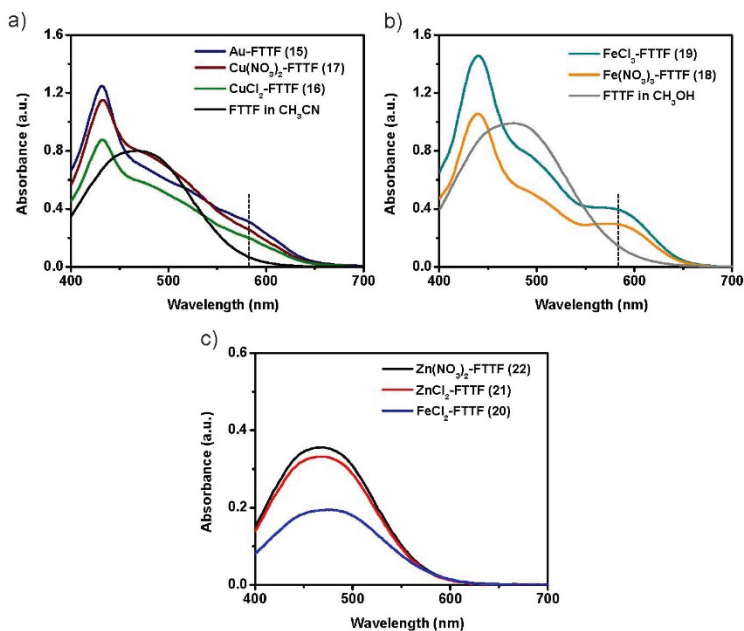


Figure 5.36. UV-Vis absorption spectra of the solutions of M-FTTF. a) **15**, **17**, **16** and pure FTTF in CH₃CN, b) **19**, **18** and pure FTTF in CH₃OH. c) **22**, **21** and **20**. Final concentrations for FTTF were 0.24 mM and for other solutions about 0.06 mM. The dash lines in Figures a) and c) indicates the position of 580 nm.

b) Morphologies

Various morphologies were observed for the products of M-FTTF obtained from bulk synthesis and microchips. The reaction of FTTF with HAuCl_4 and CuCl_2 yielded large dendrites in bulk synthesis (Figures 5.37a and 5.37d), however, 1D wire structures were obtained on both two-inlet and four-inlet microchips for the compounds **15** (Figures 5.37b and 5.37c) and **16** (Figures 5.37e and 5.37f).

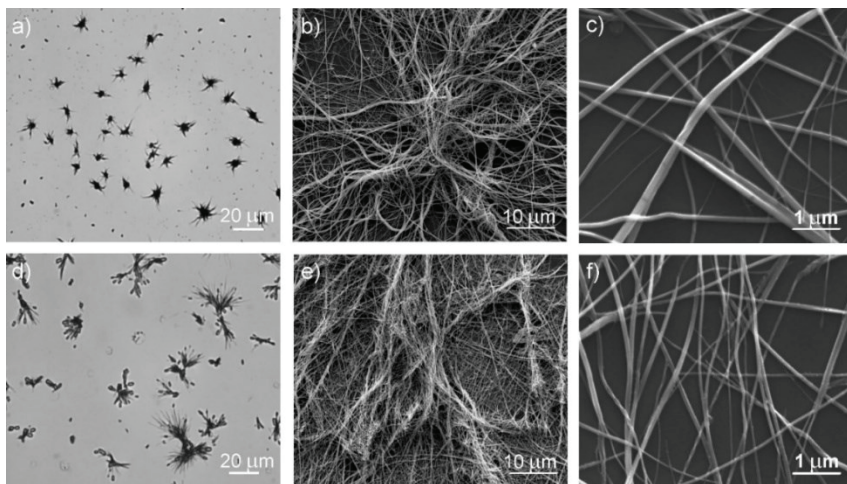


Figure 5.37. Optical and SEM images of M-FTTF generated by bulk synthesis and on microchip. a) optical image of Au-FTTF by bulk synthesis, only dendrites structures. SEM images of Au-FTTF (**15**) generated on b) two-inlet microchip at flow rates of 100 $\mu\text{L}/\text{min}$ (average diameter, $0.39 \pm 0.11 \mu\text{m}$) and c) four-inlet microchip at flow rates of 500;50;50;500 $\mu\text{L}/\text{min}$ (average diameter, $0.26 \pm 0.14 \mu\text{m}$). d) optical image of Cu-FTTF (**16**) by bulk synthesis, only dendrites structures. SEM images of Cu-FTTF generated on e) two-inlet microchip (average diameter, $0.27 \pm 0.13 \mu\text{m}$) and f) four-inlet microchip ($0.2 \pm 0.08 \mu\text{m}$).

Although $\text{Cu}(\text{NO}_3)_3$, $\text{Fe}(\text{NO}_3)_3$ and FeCl_3 induced the charge-transfer with FTTF (UV-Vis spectra, Figure 5.36b), only dendrites and particles while not 1D wire structures were observed (**17**, Figures 5.38a-c) (**18**, Figures 5.38d-f) (**19**, Figures 5.38g-i). Similarly, for the other metal salts, including FeCl_2 -FTTF (**20**, Figures 5.38j-k), ZnCl_2 -FTTF (**21**, Figures 5.38l-m) and $\text{Zn}(\text{NO}_3)_2$ -FTTF (**22**, Figures 5.38n-o), particles, dendrites or crystals were formed after reaction with FTTF.

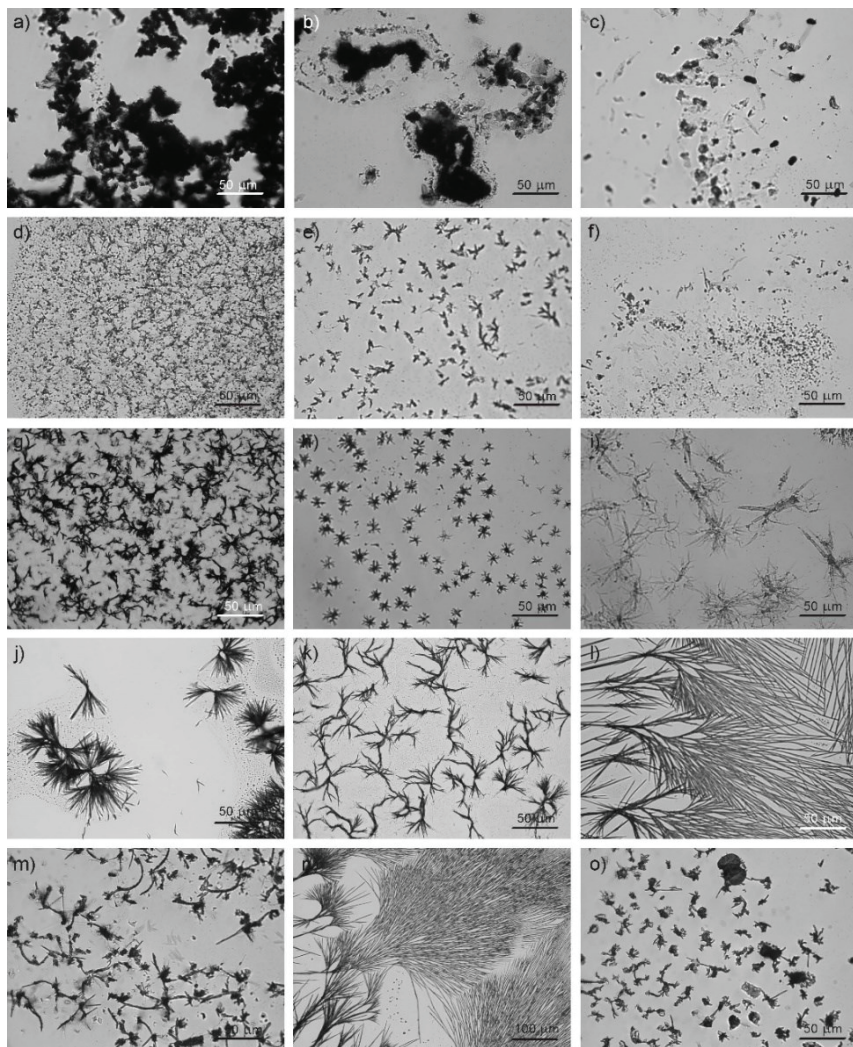


Figure 5.38. Optical images of structures from **17**, **18**, **19**, **20**, **21** and **22** in bulk and on microchips: **17** a) in bulk (clusters), b) on two-inlet chip (clusters) and c) four-inlet chip (particles). **18** d) in bulk (clusters), e) on two-inlet chip (small dendrites) and f) four-inlet chip (particles). **19** g) in bulk (small dendrites), h) on two-inlet chip (small dendrites) and i) four-inlet chip (large dendrites). **20** j) in bulk (large dendrites) and k) on four-inlet chip

(small dendrites). **21 l**) in bulk (well ordered crystal trees) and m) on four-inlet chip (large particles). **22 n**) in bulk (well ordered crystal trees) and o) on four-inlet chip (large particles). Notice the well ordered crystal trees in j), l) and n) are FTTF crystals.

c) Characterization of M-FTTF nanowires

IR spectra of **15** and **16** (obtained from microchips) and pure FTTF are displayed in Figure 5.40. The so synthesised nanowires **15** and **16** showed evidently shifted bands with the spectrum of pure FTTF in the range of 700 cm^{-1} - 1500 cm^{-1} (Figure 5.39), because of the charge-transfer reaction (UV-Vis spectra, Figure 5.36a). As emerged from the comparison of the IR vibrational modes of compounds **15**, **16** with FTTF, the aldehyde group (C=O) centred at about 1640 cm^{-1} remained after the formation of nanowires (Figure 5.39). This result suggests the possibility of further modifications of the wire using compounds which can bond to aldehyde groups e.g. amines.

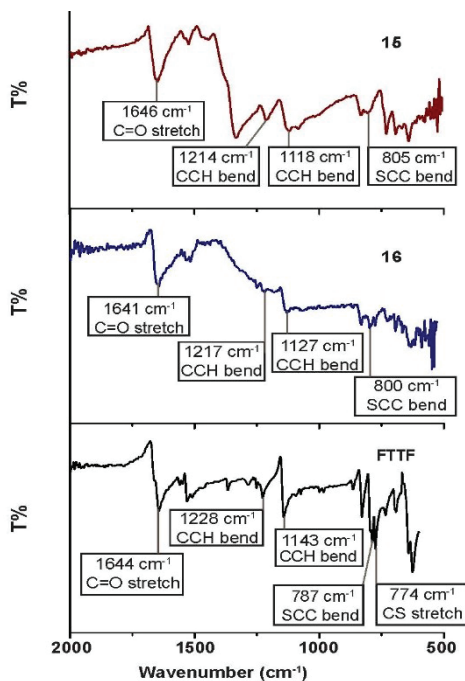


Figure 5.39. IR spectra of M-FTTF complexes. Au-FTTF (**15**), Cu-FTTF (**16**) and pure FTTF.

EDX-SEM spectra showed the presence of C, O, Au, S and Cl elements in Au-FTTF (**15**) (Figure 5.40a), and C, O, Cu, S, Cl in Cu-FTTF (**16**) (Figure 5.40b). Elemental analysis of **15** and **16** (Table 5.8) determined the composition of these two charge-transfer compounds of metal chloride and FTTF. These results demonstrated that the C₁ substitution of aldehyde group on TTF unit (Figure 5.24) did not block the stacking of TTF units, while active side groups could be preserved in the charge-transfer complexes.

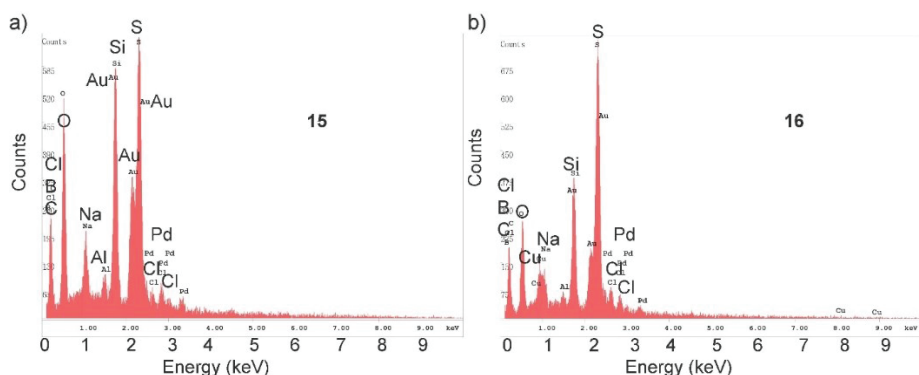


Figure 5.40. EDX-SEM spectra of M-FTTF complexes. a) Au-TTF (**15**) and b) Cu-TTF (**16**). Note the presence of Cl in a), and the presence of Cu and Cl in b).

Table 5.8. Elemental analysis of **15** and **16** complexes

Metal salts	Solvent	No.	Anal. % found (calculated)		Compound Formula
			C	H	
HAuCl ₄	CH ₃ CN	15	26.82 (25.21)	1.20 (1.20)	(FTTF) ₃ AuCl ₃
CuCl ₂	CH ₃ CN	16	28.97 (28.07)	1.72 (1.34)	(FTTF) ₂ CuCl ₂

Note: The compounds are numbered as in Table 5.4.

d) Electronic properties

I-V curves were measured for single nanowires of **15** and **16** formed on the four-inlet microchip, after connecting the nanowires to microelectrodes. As shown in Figures 5.41a and 5.41b, the nanowires showed metallic-like linear *I-V* curve. The electrical conductivities were calculated considering only the linear range of the curves in Figures 5.41a and 5.41b. And were found to be 0.66 S cm^{-1} and 0.84 S cm^{-1} for **15** (Figure 5.41c) and **16** (Figure 5.41d), respectively. Thus, these results indicated a conductive behaviour of M-FTTF nanowire structures at room temperature.

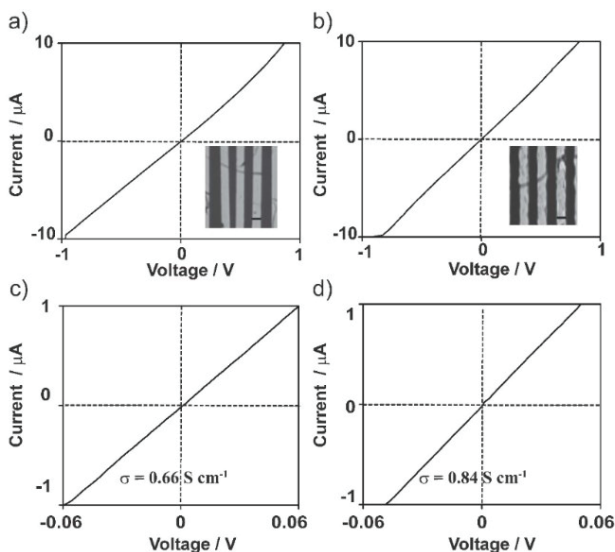


Figure 5.41. *I-V* curves of M-FTTF nanowires. a) Single Au-FTTF and b) Cu-FTTF nanowire formed on four-inlet microchip. Figure insets in a) and b) showed the aligned single nanowires on microelectrodes. The gaps between the microelectrodes are $5 \mu\text{m}$ as the scale bars. c) and d) Linear range of the *I-V* curves showing in Figures a) and b).

5.3.4 TCE-TTF, TET-TTF and BEDT-TTF

In an attempt to better understand the role of side groups in TTF derivatives, other TTF derivatives which own additional sulphur atoms at the periphery of the TTF skeleton¹⁸¹ (such as TET-TTF, TCE-TTF and BEDT-TTF) were chosen to react with transition metal ions. All these

three compounds were added to a solutions of a metal salt (HAuCl_4 and Cu(II) salts). After reacting with the latter, only BEDT-TTF resulted into wire structures (details will be discussed in the following chapter). This could be attributed to their different molecular structures, or more specifically, to the presence of short side groups at C_1 , C_2 -position ($-\text{S}-\text{CH}_2-\text{CH}_3$ and $-\text{S}-\text{CH}_2-\text{CN}$) for TET-TTF and TCE-TTF, respectively, instead of a planar S-containing aromatic ring as in BEDT-TTF (Figure 5.24). The short side groups in TET-TTF and TCE-TTF had low stacking capability, so that difficult to form wire structures.¹⁷²

Figure 5.42 shows the outcome of the reaction between TET-TTF, TCE-TTF with HAuCl_4 and CuCl_2 , proving the formation of macro-flake structures. Details on metal-BEDT-TTF nano-/microstructures are given in Chapter 5.3.5.

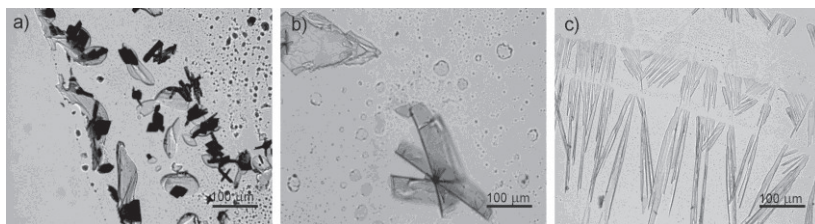


Figure 5.42. Optical images of compounds **28**, **29** and **30**. a) **28** (1.5 mM of HAuCl_4 and 6 mM of TET-TTF, both in CH_3CN), b) **29** (1.5 mM of CuCl_2 and 6 mM of TET-TTF, both in CH_3CN) and c) **30** (0.06 mM of HAuCl_4 and 0.24 mM of TCE-TTF, both in CH_3CN) generated on two-inlet microchips, respectively. All the compounds formed flake structures but no wire structures. Scale bars: 100 μm .

5.3.5 Metal-BEDT-TTF nano-/microstructures

a) UV-Vis spectroscopy

BEDT-TTF, with planar S-containing aromatic ring frames substituted at C_1, C_2 -position of TTF (Figure 5.24),¹⁷⁶ was used to react with HAuCl_4 , Cu(II) and Fe(III) salts and formed compounds **23**, **24**, **25**, **26** and **27** (Table 5.4). Here, a two-solvent protocol was applied, with metal salts dissolved in CH_3OH (0.06 mM) and BEDT-TTF in THF (0.24 mM), because of its low solubility in CH_3CN . As seen in Figure 5.43, the

absorbance shoulder at ~ 580 nm in all the spectra was observed and proved the charge-transfer between metal ions and BEDT-TTF.

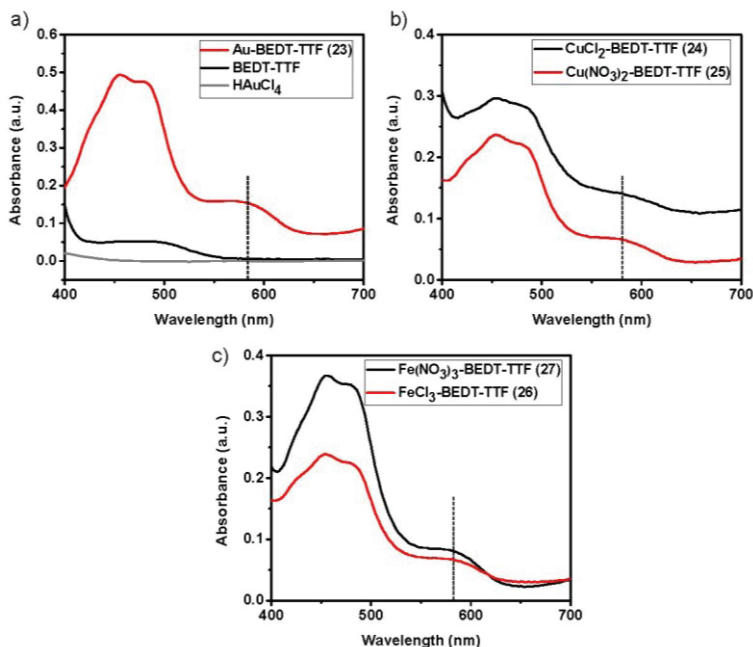


Figure 5.43. UV-Vis absorption spectra of solutions of M-BEDT-TTF. a) **23**, BEDT-TTF in THF, HAuCl_4 in CH_3OH , b) **24** and **25**. c) **27** and **26**. Final concentrations for BEDT-TTF were 0.24 mM while for other solutions about 0.06 mM. Note the absorbance at 580 nm for **23**, **24**, **25**, **26** and **27**.

b) Morphology and electrical property of M-BEDT-TTF complexes

While M-BEDT-TTF showed rods or large wire-like structures in the case of bulk synthesis (Figure 5.44), the structures obtained from microchips all exhibited nano-/microwire morphology (Figures 5.45a-c, 5.46a and 5.46c). Au-BEDT-TTF (**23**) and Fe-BEDT-TTF (**27**) formed nanowires (Figures 5.45a and 5.45c), while Cu-BEDT-TTF (**25**) resulted in microwires (Figure 5.45b). Morphology of M-TET-TTF, M-TCE-TTF and M-BEDT-TTF suggested that among the C_1 , C_2 -position substituted TTF derivatives with sulphur studied in this work, the aromatic ring

structure was more favourable than short linear groups for a strong molecular interaction to form stacking structures.^{172,182}

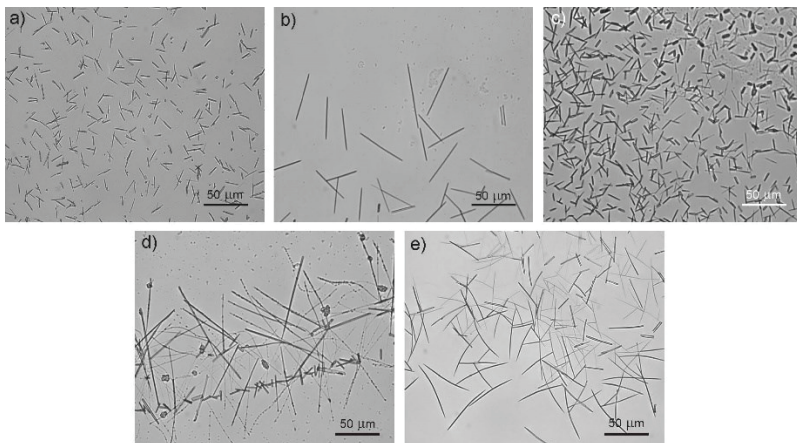


Figure 5.44. Optical images of compounds **23**, **24**, **25**, **26** and **27** formed in bulk synthesis. a) **23** ($1.73 \pm 0.61 \mu\text{m}$), b) **24** ($1.79 \pm 0.31 \mu\text{m}$), c) **25** ($3.16 \pm 0.82 \mu\text{m}$), d) **26** ($1.68 \pm 0.95 \mu\text{m}$), and e) **27** ($1.29 \pm 0.59 \mu\text{m}$) formed in bulk synthesis separately. All of them formed wire like structures. Scale bars: $50 \mu\text{m}$.

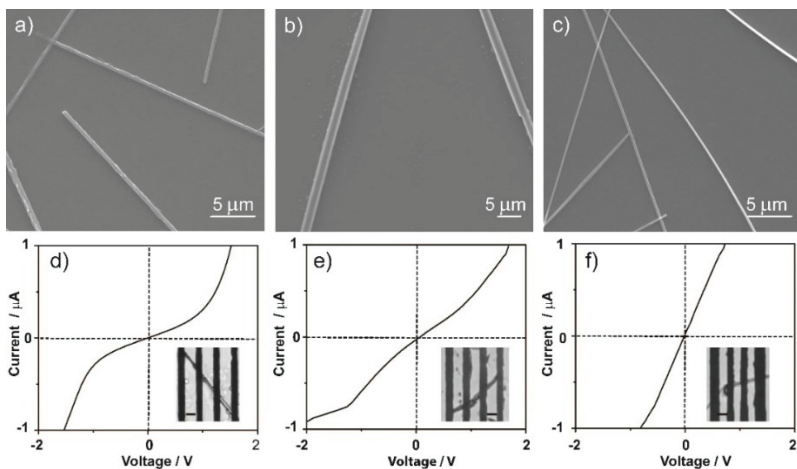


Figure 5.45. SEM images and I - V curves of structures of **23**, **25** and **27**. a) Au-BEDT-

TTF (**23**) (diameter: $0.56 \pm 0.12 \mu\text{m}$), b) Cu-BEDT-TTF (**25**) (diameter: $2.11 \pm 0.53 \mu\text{m}$) and c) Fe-BEDT-TTF (**27**) (average diameter: $0.47 \pm 0.11 \mu\text{m}$) formed on the four-inlet microchip. d), e) and f) I - V curves of single wires from **23**, **25** and **27**, respectively. Figure insets in d), e) and f) show the interconnecting single nano-/microwire on microelectrodes.

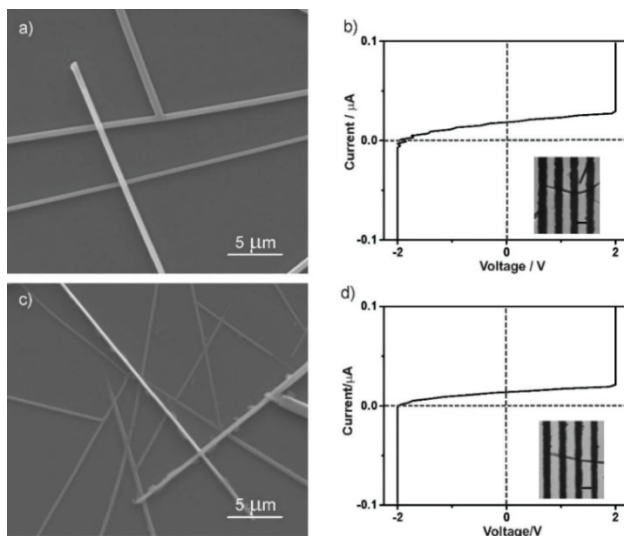


Figure 5.46. SEM images and I - V curves of structures of **24** and **26**. a) **24** (average diameter: $0.59 \pm 0.14 \mu\text{m}$). b) I - V curve of a single nanowire of **24**. c) SEM images of **26** (average diameter: $0.50 \pm 0.12 \mu\text{m}$). d) I - V curve of a single nanowire of **26**. Figure insets of b) and d) show the alignment of single nanowires on the microelectrodes. The gaps between the microelectrodes were $5 \mu\text{m}$ as the scale bar. A current overload in Figures b) and d) was observed when the low current sweep from $-0.1 \mu\text{A}$ to $+0.1 \mu\text{A}$ applied with a Keithley 2612 A system source meter.

BEDT is known as an excellent electron donor and to form various charge-transfer compounds with different electrical behaviours from insulators to semiconductors, or also to organic metal, according to their specific composition.^{14,183} In this work, the conductivity of single M-BEDT-TTF nano-/microwires was tested and measured by aligning single wires on interconnecting microelectrodes, as for the other M-TTF-based nanostructures. As shown in Figures 5.45d to 5.45f, all the structures

derived from the BEDT-TTF-based complexes (**23**, **25** and **27**) exhibited a non-linear behaviour in the current sweeping range from $-1\ \mu\text{A}$ to $+1\ \mu\text{A}$, proving the conductive nature of these wires at room temperature. However, the attempt in acquiring I - V curves of structures from **24** and **26** was not successful in this work with the source meter (Figure 5.46b and 5.46d, respectively). For the compounds **23**, **25** and **27**, the electrical conductivity was calculated taking into account the linear part of I - V curves (Figure 5.45) and found to be $6.3 \times 10^{-3}\ \text{S cm}^{-1}$, $4.8 \times 10^{-3}\ \text{S cm}^{-1}$ and $1.2 \times 10^{-2}\ \text{S cm}^{-1}$, respectively (Figure 5.47). The conductivity values so obtained are comparable to the values reported for other Cu-BEDTTTF powder products.^{174,176}

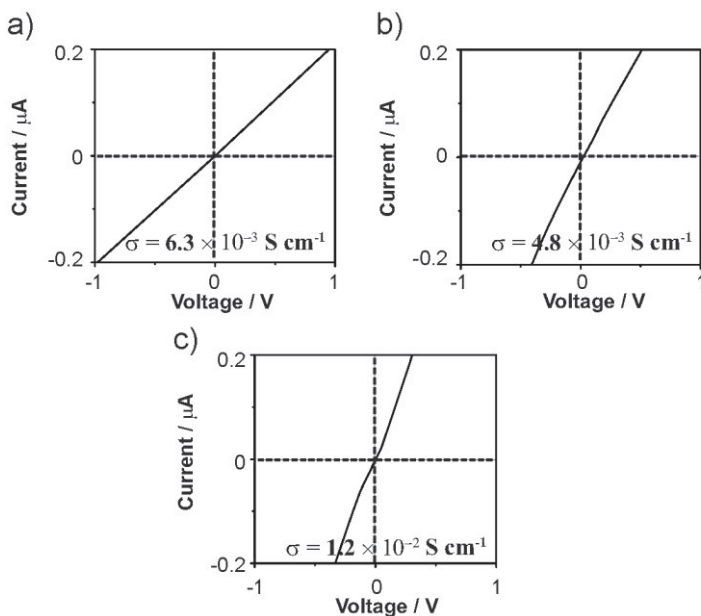


Figure 5.47. Linear I - V curves and calculated electrical conductivity of the single wires of **23**, **25** and **27**. a) **23**, $\sigma = 6.3 \times 10^{-3}\ \text{S cm}^{-1}$, b) **25**, $\sigma = 4.8 \times 10^{-3}\ \text{S cm}^{-1}$ and c) **27**, $\sigma = 1.2 \times 10^{-2}\ \text{S cm}^{-1}$. Such I - V characteristics represent the linear range of the curves in Figures 5.45d to 5.45f. σ refers to the conductivities at room temperature.

c) Characterization of M-BEDT-TTF wires

Due to the low product yield of reactions between metal salts and BEDT-TTF, IR and EA analysis was not carried out. EDX-SEM spectra of **23**, **25** and **27** are shown in Figure 5.48. Taking into account the spectrum of a glass slide (Figure 5.48a), the presence of C, S, Au and Cl elements was confirmed for the compound Au-BEDT-TTF (**23**) (Figure 5.48b), while C, N, Cu and S elements for Cu-BEDT-TTF (**25**) (Figure 5.48c) and C, N, Fe, S for Fe-BEDT-TTF (**27**) (Figure 5.48d). Thus, the relative composition of respective metal salts and BEDT-TTF could be determined in each complexes.

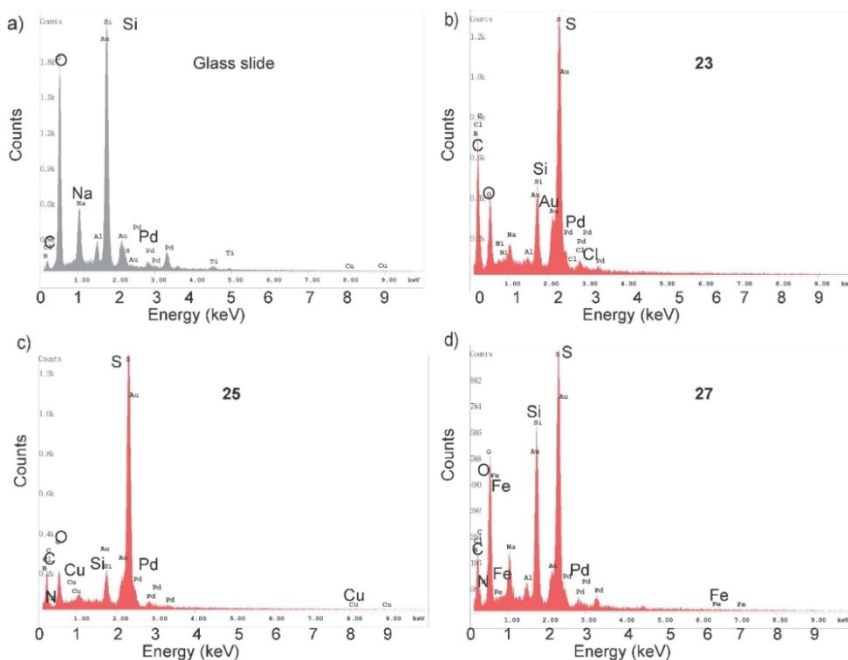


Figure 5.48. EDX-SEM spectra of M-BEDT-TTF. a) the glass slide, b) Au-BEDT-TTF (**23**), c) Cu-BEDT-TTF (**25**) and d) Fe-BEDT-TTF (**27**). Note the existence of Cu and Fe in Figures c) and d). The low intensity of N-peaks could be attributed to the low concentration of N in the wires.

5.3.6 Sensing of organic gases by single TTF-based wires

Since TTF-based charge-transfer compounds are conductive and can be applied as sensing platforms. Following, a first experiment was carried out using single Au-TTF hybrid wires as sensing elements for organic vapours, such as organic acids (e.g. acetic acid) and organic thiol (e.g. dodecanethiol), which are considered to be toxic in high concentrations. Such an experiment was conducted in a closed chamber filled with a saturated organic vapour gas.

Single Au-TTF wires were deposited and aligned on interconnecting microelectrode, and then exposed to different gases separately. The resistance response was obtained by using a four-point probe and measuring for 60 min at intervals of 10 min each. Different resistance signal (R) was observed for different analytes. As shown in Figure 5.49, negligible changes in the normalized resistance ratio (R/R^0) (R^0 represents the resistance of Au-TTF wires before exposure to gases) were observed for the wires exposed to dodecanethiol. However, when exposed to acetic acid, the resistance ratio of single Au-TTF wire increased gradually after 15 min and increased after 30 min. This indicates the higher selectivity of TTF towards acetic acid than dodecanethiol. Although such preliminary data showed that Au-TTF is relatively slow in sensing gases (with clear signal changes observable after 10 min), the high resistance ratio indicated the possible use of this structure as a gas sensor. Analogously, other TTF-based nano-/microwires are expected to exhibit similar sensing abilities, as they all have TTF-based structures and show common features in their conductive response. In the future, more work will be done on studying this sensing mechanism and developing fast responding gas sensors by using and improving different elements e.g. quantitative gas flow and closed microchamber.

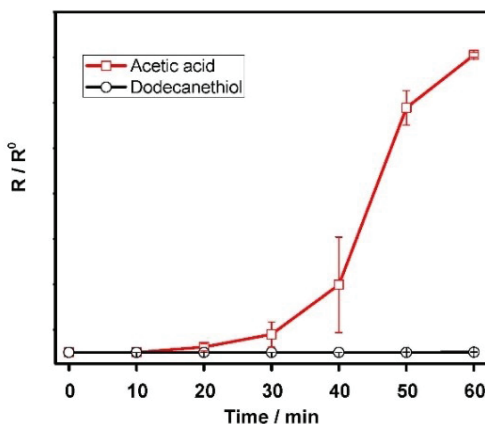


Figure 5.49. Sensing of organic gases by single Au-TTF wire. Normalized resistance response ratio (R/R^0) of single Au-TTF wires after exposing to two volatile organic vapours, acetic acid and dodecanethiol separately. (Exposure time: 60 min in total, with 10 min steps). Error bars indicate the standard deviation obtained from six measurements.

In Chapters 5.1-5.3, TTF-based metal-organic charge-transfer compounds were discussed. The sensing application and growth mechanism of Au-TTF, as well as characteristics of various metal-TTF based complexes were well understood. In Chapter 5.4, the synthesis and characterization of other metal-organic complex using a TCNQ as an organic ligand will be shown and discussed.

5.4 Localized synthesis of conductive Cu-TCNQ nanostructures in ultra-small microchambers for nanoelectronics

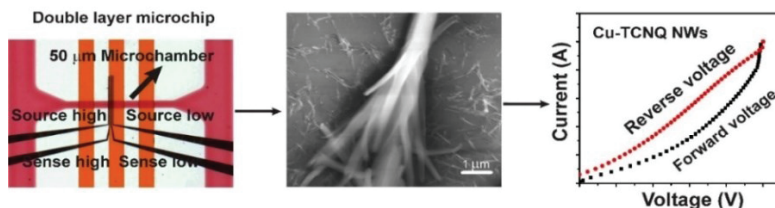


Figure 5.50. Graphic abstract of the synthesis, characterization and analysis of Cu-TCNQ. The synthesis was carried out in a 50 μm microchamber. The obtained Cu-TCNQ was characterized by SEM. A direct measurement of the I - V curves was achieved using the prefabricated microelectrodes after the synthesis. The results on this project has been discussed and the manuscript is ready for submission.

In the field of materials science, metal-organic complexes based on TCNQ have attracted considerable research interest, due to their intriguing electronic and magnetic properties, and their potential applications in building advanced conductive materials, sensors, magnetic devices, as well as energy and data storage substrates.^{32,184-187} Various metal-TCNQ complexes were synthesized and studied in the past decades, using different metals, such as Ag-TCNQ, Cu-TCNQ, Mn-TCNQ, Fe-TCNQ, Co-TCNQ and Ni-TCNQ.^{23,36,38,188} Among these charge-transfer salts, Ag-TCNQ and Cu-TCNQ are more advantageous than the others because they can be formed by self-assembly on the corresponding metal when exposed to TCNQ (either in gas⁴¹ or solution¹⁸⁹ phase).

In nanomaterials and nanotechnology field, Cu-TCNQ has received great attention after the discovery of its quasi-1D crystalline nanostructures.^{190,191} Because of their large surface-to-volume ratio and size effects, Cu-TCNQ nanowires showed their advantages for building nanoelectronic devices over their widely studied bulk and thin film counterparts. For this reason, much effort has been put in developing new approaches for the control of the Cu-TCNQ nanostructure growth. Reported methods fall into three categories: firstly, solution reaction of Cu(I) precursors with TCNQ solution in CH_3CN ;³⁹ secondly, “spontaneous electrolysis” technique with the reaction between TCNQ dissolved in CH_3CN and metallic copper (Cu^0);^{39,190} and thirdly, vapour

deposition of TCNQ on Cu⁰ metal surfaces.^{22,45} However, all these techniques required inert atmosphere since Cu⁰ is quickly oxidized when directly exposed to air.¹⁹² In some cases, high temperatures (over 100 °C) were also needed. Thus, the synthesis of Cu-TCNQ in less harsh environment at room temperature is still challenging. In addition, precise manipulating and positioning of nanostructures onto pre-fabricated microelectrodes is highly desirable to finely control their alignment, since this would make the overall assembly of final nanodevices easier. Another difficulty in the preparation of nano-sized crystal structures for electronic devices is the reproducibility with respect to uniform morphology.

To solve the abovementioned problems, microfluidics technique was shown to be an optimal approach, due to its possibility of a precise fluid handling, allowing a spatially controllable formation of structures inside locally confined microchambers. In addition, in combination with integrated electrodes in the microchambers, a direct contact of the nanostructures with microelectrodes is achievable without further complicated manipulation.^{76,93,193} Recently, the confined synthesis and integration of Ag-TCNQ in microchambers using a two-layer microchip have been reported.²⁸ Ag-TCNQ was synthesized by depositing TCNQ solution on dried Ag film, which is stable in air.

Figure 5.50 shows the general idea of the synthesis, characterization and analysis of Cu-TCNQ. In this work, the microchamber arrays were greatly improved for the localized formation of Cu-TCNQ nano-/microscale structures in ultra-small microchambers. This method allows not only a continuous and multiple chemical reactions in confined microchambers, but also an excellent fluid handling which ensures the *in situ* change of trapped Cu⁰ nanoparticles into Cu-TCNQ nanostructures. Furthermore, since the synthesis is carried out in a solution phase inside the microchip, exclusion of exogenous oxygen into the system is possible when pretreated (Ar gas bubbled) solutions are used. For the synthesis of Cu-TCNQ structures, the spontaneous electrolysis of Cu⁰ reacting with TCNQ solutions in microchambers was adopted. With the proposed method, the morphologies of Cu-TCNQ nano-/micro structures could be controlled by adjusting the concentration of precursors and the reaction time. Outcomes of this method were analysed by SEM. Moreover, the conductive property and memory effect of such synthesized Cu-TCNQ nanostructures was tested by using integrated microelectrode arrays without further manipulation. This work represents the first attempt to synthesize Cu-TCNQ nanostructures by microfluidic-assisted techniques in “normal” environment at room temperature, with direct integration into an electronic system.

5.4.1 Microchips with a microchamber array

As shown in Figure 5.51, the microfluidic device was a double-layer microchip made of PDMS via soft lithography, consisting of a top control layer with three gas channels and a fluid layer with eight parallel microchambers, separated by a thin and flexible PDMS membrane. The multilayer chip was assembled and integrated to a glass slide with pre-patterned microelectrodes to form the final device (Figures 5.51a and 5.51b). The microchambers could be operated by the three parallel control channels upon pressurization with N_2 gas (see Chapter 4.5). Compared to the microchamber array reported for Ag-TCNQ,²⁸ several aspects were improved in this chip design for Cu-TCNQ. Firstly, 50 μm wide microchambers were fabricated to reduce the volume of solutions required to a sub-nanolitre scale or even lower. Secondly, the microchannel towards inlet and outlet of the fluid layer were changed in order to better control the fluids into ultra-small chambers. Thirdly, for the electrical measurements of the structures formed in microchambers, a four-electrode system (source high, source low, sense high and sense low) was used in the four-point probe measurements (Figures 5.51c), instead of the two-point method adopted for the measurement of Ag-TCNQ. The synthesis of Cu^0 in microchamber by controlling the gas channels is shown in Figure 5.51d to 5.51f (detailed experimental procedure see Chapter 4.5).

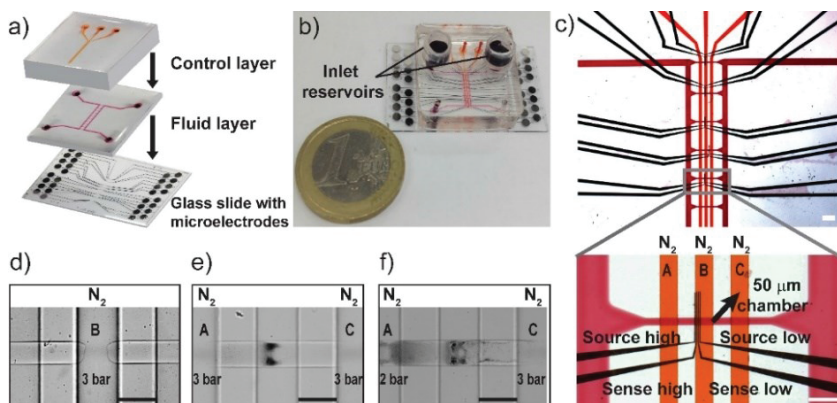
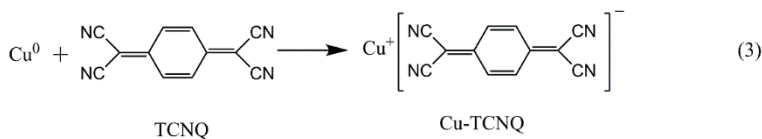
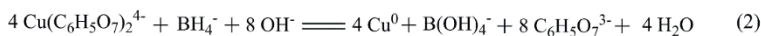


Figure 5.51. Microchip device for the synthesis of Cu-TCNQ structures. a) Schematic of the alignment of the microchip; b) Photograph of the final device with two reservoirs added to the inlets after the alignment of the microchip. A one Euro coin is shown for

scale; c) Top: optical image of the microchip, with orange and red food dyes in the control and fluidic layers, respectively; Bottom: magnification of one reaction microchamber (50 μm in width) with aligned microelectrodes. The four electrodes used in this experiment are shown in this image, with source high and source low electrodes outside, sense high and sense low electrodes insides. Scale bars: 200 μm ; d)-f) Operation of gas channels with d) the middle gas channel B pressured to 3 bar to totally close the chamber; e) the two side gas channels A and C pressured to 3 bar to stop flows and allow the reaction inside the microchamber (black particles started to form from the middle indicating the formation of Cu^0) and f) the channel A was released to 2 bar to allow the slow solvent exchange in the microchamber and wash the Cu^0 formed inside the chamber. Scale bars: 100 μm .

5.4.2 Reaction mechanism

Cu -TCNQ structures were synthesized by using Cu^0 and TCNQ dissolved in CH_3CN . As shown in Scheme 5.4, Cu^0 nanoparticles were produced by a two-step reduction process. In the first step, $\text{Cu}(\text{C}_6\text{H}_5\text{O}_7)_2^{4-}$ was obtained by mixing CuSO_4 and $\text{C}_6\text{H}_5\text{O}_7\text{Na}_3$ solutions (Scheme 5.4, Equation 1). In the second step, NaBH_4 dissolved in NaOH was used to reduce $\text{Cu}(\text{C}_6\text{H}_5\text{O}_7)_2^{4-}$ to Cu^0 (Scheme 5.4, Equation 2). After the formation of Cu^0 , the TCNQ solution in CH_3CN was added and, by reacting with Cu^0 , resulted in the formation of Cu -TCNQ, because of the ion transfer effect between the two precursors (Scheme 5.4, Equation 3).



Scheme 5.4. Reaction mechanism for the formation of Cu^0 and Cu -TCNQ.

5.4.3 Controlled synthesis of Cu and Cu -TCNQ structures

Since Cu^0 can be easily to be oxidized when in contact with air,¹⁹⁴ special precautions were taken in order to get rid of oxygen in the microchips. First of all, all the solutions were bubbled with argon gas for 20 min before each

experiment. Then, two reservoirs with water or CH_3CN were used for the two inlets of the chambers (Figure 5.51b), with the purpose of avoiding air bubbles into the microchannels during the experiment. With the so designed microchip, the localized synthesis of Cu^0 inside the microchamber was achieved by adjusting the pressure into the gas channels to 3 bar (Figures 5.51d and 5.51e, and Figure 4.3 (i) and (ii)). After the formation and washing of Cu^0 , the direct synthesis of charge-transfer compound Cu-TCNQ was achieved by slightly opening the valves to allow the diffusion of TCNQ solutions into confined microchambers with trapped Cu^0 particles (Figure 5.51f and Figure 4.3 (v), see Chapter 4.5 for further details).

The copper formed via this method appeared brown in colour and shiny as a metal. As observed by eye on a glass slide (Figure 5.52a), as well as under an optical microscope on a glass slide (Figure 5.52c) and in a microchannel (Figures 5.52d and 5.52e). This indicates the presence of metal copper. After the reaction with TCNQ solutions on a glass slide, a dark blue product was obtained (Figure 5.52b), indicating the formation of Cu-TCNQs. The wire morphologies were observed under microscope in a microchannel (Figure 5.52f).

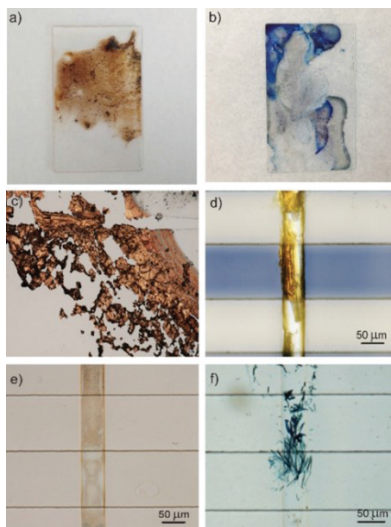


Figure 5.52. Photograph of Cu^0 and Cu-TCNQ. a) Cu^0 right after its formation on a non-

bonded chip by direct injection of Cu^{2+} and NaBH_4 solutions; b) Cu-TCNQ after dropping of TCNQ solutions on Cu^0 film formed on a non-bonded chip. Optical images of c) Cu^0 formed on a non-bonded chip after dried in vacuum; d) in a microchamber (reduced from 250 mM Cu^{2+}) and e) in a microchamber (reduced from 50 mM Cu^{2+}); f) dark blue Cu-TCNQ wires formed in microchannel. Scale bars: 50 μm . Note that the brown Cu^0 in Figure a) turned into black after exposure to air in tens of seconds, indicating the fast oxidation of Cu^0 .

With the microfluidic techniques, the density of Cu^0 layer and morphologies of Cu-TCNQ could be formed in a controlled way, for example, by using different concentration of precursors and controlling the reaction time (Table 5.9). High concentration of $\text{Cu}(\text{C}_6\text{H}_5\text{O}_7)_2^{4+}/\text{NaBH}_4$ (250 mM/ 500 mM) resulted in a thick Cu^0 layer (Figure 5.53a). Upon reaction with 5 mM TCNQ at a flow rate of 2 $\mu\text{L}/\text{min}$ for 10 min, dense short nano-/microrods (0.4-1 μm in diameter, 5-10 μm in length) were observed (Figures 5.53b and 5.53c). However, five times diluted $\text{Cu}(\text{C}_6\text{H}_5\text{O}_7)_2^{4+}/\text{NaBH}_4$ solutions (50 mM/100 mM) resulted in large particles of Cu^0 , followed by the formation of long nano-/microrods after reacting with 5 mM TCNQ for 10 min (Figures 5.53d-5.53f, structures with 0.8-1.5 μm in diameter, 10-50 μm in length). In contrast, a very low concentration of the $\text{Cu}(\text{C}_6\text{H}_5\text{O}_7)_2^{4+}/\text{NaBH}_4$ solution (25 mM/50 mM) was used and led to the formation of a thin Cu^0 layer in the channel (Figure 5.53g), after reacting with low concentrated TCNQ solution (2 mM) for 10 min. In this case, bundles of nanowire structures were observed (Figure 5.53h), as also seen by SEM results (Figures 5.54a and 5.54b). In addition, a longer reaction time (20 min) caused the formation of larger structures (Figure 5.53i), compared to those in Figure 5.53h. This may be due to the aggregation of wire structures.¹⁹⁰ Both the composition of Cu^0 and resulted Cu-TCNQ structures were determined by EDX (Figures 5.54c and 5.54d). Using high concentrations of $\text{Cu}(\text{C}_6\text{H}_5\text{O}_7)_2^{4+}/\text{NaBH}_4$ (250 mM/500 mM), bubbles were observed in the channel, likely due to the release of hydrogen in the redox reaction between NaBH_4 and $\text{Cu}(\text{C}_6\text{H}_5\text{O}_7)_2^{4+}$. Instead, this was not observed when low concentrated solutions were used. Thus, low concentration of precursors ($\text{Cu}(\text{C}_6\text{H}_5\text{O}_7)_2^{4+}/\text{NaBH}_4$, 25 mM/50 mM) and short reaction time (10 min) are ideal for the synthesis of nanometer scaled Cu-TCNQ structures.

5.4 Localized synthesis of conductive Cu-TCNQ nanostructures in ultra-small microchambers for nanoelectronics

Table 5.9. Morphology of structures formed under different reaction conditions on microchip

Cu(C ₆ H ₅ O ₇) ₂ ⁴⁺ /NaBH ₄ Concentration	TCNQ concentration	Reaction time	Morphology of products* Φ diameter, <i>L</i> length
250 mM/ 500 mM	5 mM	10 min	Short nano-/microrods Φ 0.4-1 μm. <i>L</i> 5-10 μm
50 mM/ 100 mM	5 mM	10 min	Long nano-/microrods Φ 0.8-1.5 μm. <i>L</i> 10-50 μm
25 mM/ 50 mM	2 mM	10 min	Nanowire bundles Φ 0.1-0.8 μm. <i>L</i> 5-20 μm
25 mM/ 50 mM	2 mM	20 min	Microrods

* The optical and SEM images are shown in Figures 5.53 and 5.54.

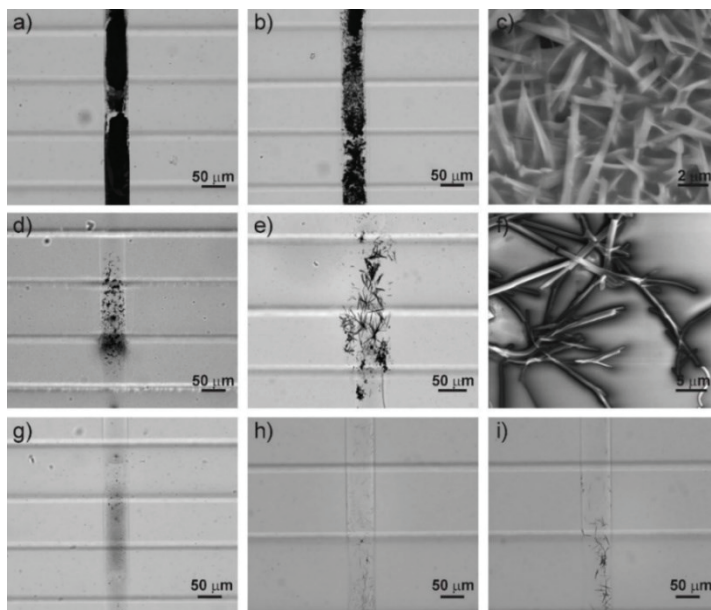


Figure 5.53. The Cu⁰ layer and Cu-TCNQ formed by using different concentrations of Cu²⁺ and reductant. a)-c) represents the a) Cu⁰ layer reduced from 250 mM Cu(C₆H₅O₇)₂⁴⁺/500 mM NaBH₄ b) Cu-TCNQ in microchamber after reaction with 5 mM

TCNQ at flow rate of 2 $\mu\text{L}/\text{min}$ for 10 min, and c) SEM image of Cu-TCNQ (short nano-/microrods, 0.4-1 μm in diameter, 5-10 μm in length). d) Cu^0 layer reduced from 50 mM $\text{Cu}(\text{C}_6\text{H}_5\text{O}_7)_2^{4-}/100$ mM NaBH_4 e) Cu-TCNQ in microchamber after reaction with 5 mM TCNQ at flow rate of 2 $\mu\text{L}/\text{min}$ for 10 min, and f) SEM image of Cu-TCNQ (long nano-/micro-rods, 0.8-1.5 μm in diameter, 10-50 μm in length). g) Cu^0 layer reduced from 25 mM $\text{Cu}(\text{C}_6\text{H}_5\text{O}_7)_2^{4-}/50$ mM NaBH_4 h) Cu-TCNQ in microchamber after reaction with 2 mM TCNQ at flow rate of 2 $\mu\text{L}/\text{min}$ for 10 min, and i) after 20 min.

5.4.4 Characterization of Cu-TCNQ nanostructures

a) SEM and EDX spectroscopy

Both the composition of the copper layer and formed Cu-TCNQ nanowires were determined by EDX. Compared to the spectrum of Cu^0 (Figure 5.54c), the appearance of N and the higher concentration of C proved that TCNQ (molecular formula $\text{C}_{12}\text{H}_4\text{N}_4$) is part of the resulted nanowires (Figure 5.54d). Combined with the Cu signal, it is evident that the nanowires are composed of Cu and TCNQ.

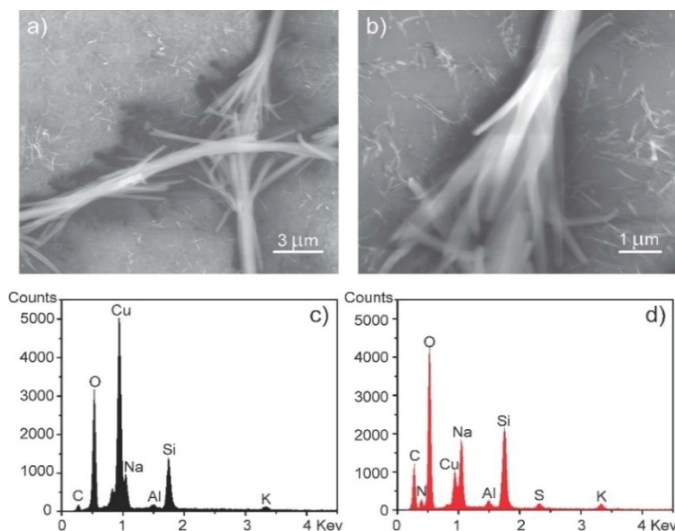


Figure 5.54. SEM images and EDX spectra of Cu-TCNQ nanostructures. The SEM images of a) Cu-TCNQ nanowire bundles (100-800 nm in diameter, 5-20 μm in length) and b) a wire bundle; c) The EDX spectrum of c) Cu layer (notice the strong Cu element

signal), and d) Cu-TCNQ nanowire bundles. The strong O signals in the EDX spectra mainly obtained from glass slide (Figure 5.57a) and partially from the oxidation of samples upon exposure to air.

b) UV-Vis absorption

The UV-Vis spectra of neutral TCNQ and Cu-TCNQ were obtained, with the latter obtained from eluted solution of a non-bonded microchip after the synthesis. As indicated in Figure 5.55, neutral TCNQ showed only one peak at 394 nm. In contrast, Cu-TCNQ solution exhibited a broad peak at 416 nm and absorption peaks at 746 nm and 840 nm, which could be assigned to TCNQ anion radicals in the sample.¹⁹⁰

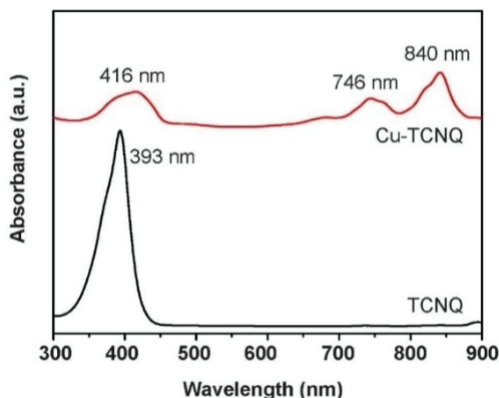


Figure 5.55. UV-Vis absorption spectra of TCNQ (black) and Cu-TCNQ (red) solutions in CH₃CN.

c) FT-IR and Raman spectroscopy

In reported studies, two polymorphs of Cu-TCNQ have been identified: one with quasi-1D structures and high electric conductivity (phase I), the other with pallets morphology and low conductivity (phase II).³⁹ These two phases could be identified by their distinct morphology, IR spectra and electronic characteristics.¹⁹⁰ In this work, Cu-TCNQ crystals showed

wire-like nano-/microstructures, suggesting the formation of Cu-TCNQ in phase I.

FT-IR and Raman measurements were carried out in order to determine the oxidation state of TCNQ molecules in neutral TCNQ and Cu-TCNQ nanostructures (Figure 5.56). As can be seen from the IR spectra (Figure 5.56a), compared to the spectrum of pure TCNQ, the C=C-H mode of Cu-TCNQ shifted from 861 cm^{-1} to 825 cm^{-1} . In addition, the C=C ring stretching peak at 1543 cm^{-1} split into two peaks at 1506 cm^{-1} and 1577 cm^{-1} . Typically, the peak at 1506 cm^{-1} denoted the formation of TCNQ anion radicals.¹⁹⁰ The C=C wing-stretching mode was also represented by the peak at 1354 cm^{-1} . Moreover, the strong band at $\sim 2200\text{ cm}^{-1}$ was associated to the C \equiv N stretching mode. Here, the strong absorption at 2200 cm^{-1} with a small shoulder peak at about 2172 cm^{-1} proved the formation of Cu-TCNQ (phase I), because the phase II would exhibit two strong sharp peaks.³⁹

The Raman spectral analysis of Cu-TCNQ (Figure 5.56b) showed the main characteristic vibration modes at 1205 cm^{-1} (C=C-H bending), 1377 cm^{-1} (C-CN stretching), 1606 cm^{-1} (C=C ring stretching), and 2209 cm^{-1} (C \equiv N stretching). Compared to the Raman spectrum of neutral TCNQ crystal, the C-CN stretching mode in Cu-TCNQ shifts from 1455 cm^{-1} to 1377 cm^{-1} , because of complete charge-transfer between Cu⁰ and TCNQ molecules.^{194,195} Thus, the FT-IR and Raman spectra clearly indicate the formation of Cu-TCNQ (phase I) in these nanostructures.

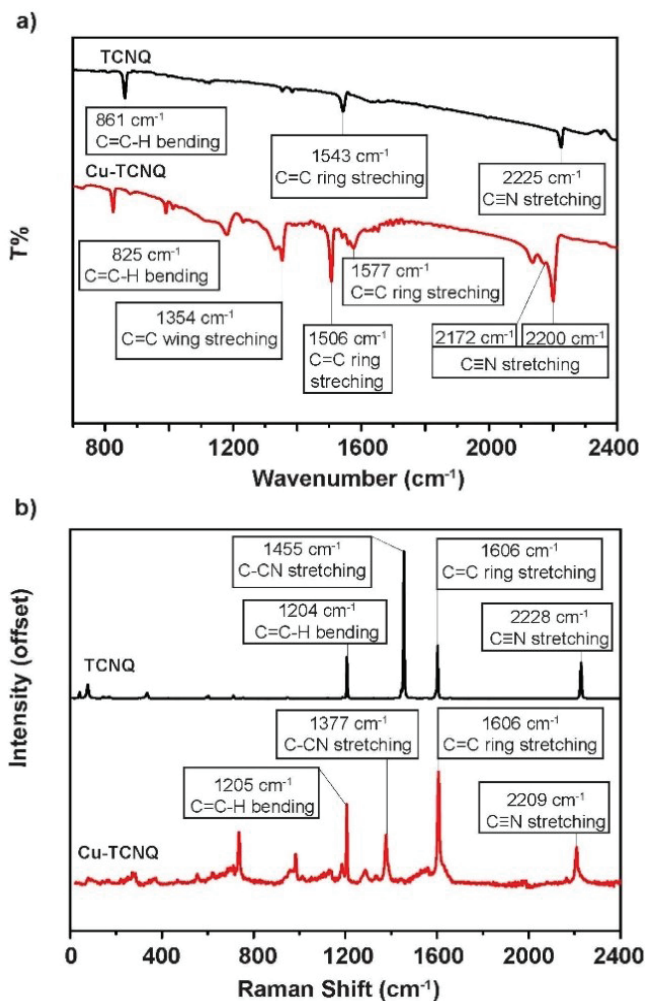


Figure 5.56. FT-IR and Raman analysis of TCNQ and Cu-TCNQ. a) FT-IR and b) Raman spectra of TCNQ and Cu-TCNQ nanowires obtained from non-bonded microchips at concentration of $\text{Cu}(\text{C}_6\text{H}_5\text{O}_7)_2^{4-}/\text{NaBH}_4$ (25 mM/ 50 mM) after reacting with 2 mM TCNQ.

5.4.5 Characterization of Cu-TCNQ microstructures

The larger microstructures formed at higher concentration of precursors (Figures 5.54e and 5.54f) were also characterized by EDX, FT-IR and Raman analysis. Compared to the EDX spectrum of glass slide (Figure 5.57a), the spectrum of the microstructures clearly showed the compositions of Cu-TCNQ with C, N and Cu (Figure 5.57b). FT-IR and Raman spectra of Cu-TCNQ microstructures (Figure 5.58) showed characteristics similar to those observed for nanowires (Figure 5.56), and suggested a similar composition of these structures. Thus, these results clearly proved the formation of Cu-TCNQ (phase I) microwire structures using this *in situ* synthesis technique.

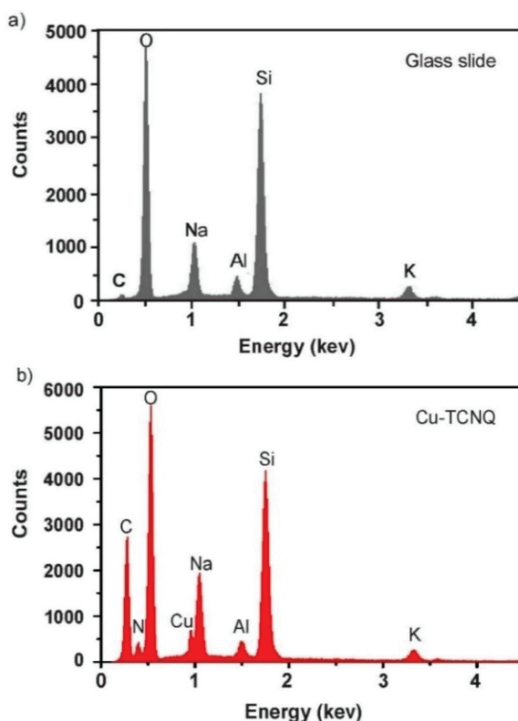


Figure 5.57. EDX-SEM spectra of a) glass slide and b) Cu-TCNQ microstructures. Compared to a), the spectrum b) clearly indicates the increase in C and presence of N and Cu in Cu-TCNQ.

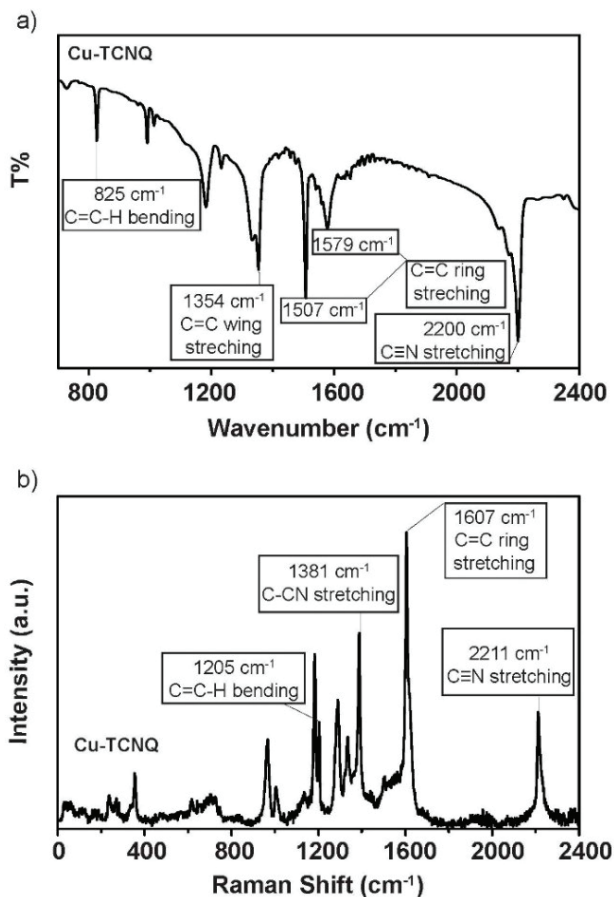


Figure 5.58. FT-IR and Raman characterization of Cu-TCNQ microstructures. a) FT-IR and b) Raman spectra of Cu-TCNQ microstructures. Samples used here were synthesized by the reaction of 5 mM TCNQ with a thick Cu^0 layer (250 mM $\text{Cu}(\text{C}_6\text{H}_5\text{O}_7)_2^{4-}/$ 500 mM NaBH_4).

5.4.6 Electrical properties of Cu-TCNQ nano-/microstructures

To confirm the possibility of a direct integration and to characterize the electrical properties of Cu-TCNQ nanostructures, the I - V curves of Cu^0 layer

before and after reacting with TCNQ solutions were obtained on-chip by four-point probe measurements after solvent evaporation in vacuum. The graph in Figure 5.59a shows a linear I - V sweep for the copper layer, indicating its typical metallic nature. In contrast, after the formation of nanostructures inside different microchambers, non-linear I - V curves were obtained (Figure 5.59b). The quasi-symmetric characteristics of the I - V curves for wire bundles indicated the formation of Cu-TCNQ crystals and the good contact with the prefabricated microelectrodes. Reproducible I - V responses indicated the possible application of this technique for parallelized integration of conductive nanowires. Moreover, the electrical properties of the synthesized nanowire devices were proven to be stable in air. By applying a voltage from 0 V to 10 V and back to 0 V, reversible hysteresis I - V curves were observed (Figure 5.59c). The two switchable states were confirmed and attributed to low and high conductivity states, or “OFF” and “ON” states, respectively (Equation 5.2). A detailed discussion of the “ON” and “OFF” states for M-TCNQ can be found in Chapter 1.4 and literature⁴⁵. The reversible hysteresis I - V curves proved the good memory behaviour of Cu-TCNQ nanowire bundles. The conductive behaviour of larger microstructures was also tested (Figure 5.59d) and the nonlinearity of the I - V curve provided an evidence that the Cu-TCNQ was in the conductive phase I.

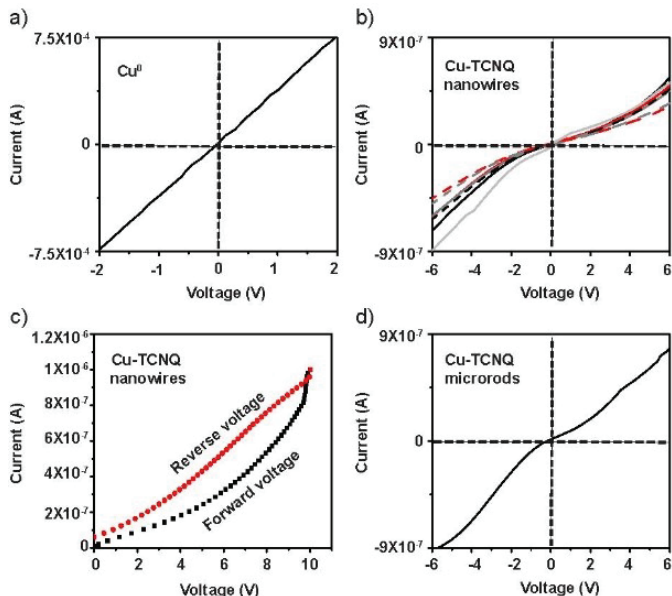
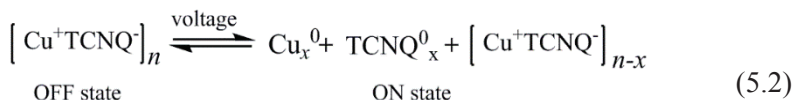


Figure 5.59. *I-V* characteristics of Cu⁰ and Cu-TCNQ at room-temperature. a) Cu⁰ film and b) multiple sweeps of different integrated Cu-TCNQ nanowire bundles in different microchambers. c) *I-V* curves recorded for Cu-TCNQ nanowire bundles showing hysteresis in the electrical response after sweeping the applied voltage from 0 V to 10 V. Forward voltage curve relates to the “ON” state, while reverse voltage curve relates to the “OFF” state. d) *I-V* curve of Cu-TCNQ microstructures. The non-linear characteristics indicates the formation of Cu-TCNQ crystals of conductive phase I.



The reversible conductivity response of the Cu-TCNQ nano-/microstructures obtained in this work showed consistency with other reported work.^{45,195} This proved also the efficiency of the microfluidic-based synthesis used here. In addition, the so proposed method demonstrated to achieve a well-control of conductive Cu-TCNQ (phase I) structures in ambient environment, showing the advantage of using microfluidic techniques, instead of the conventional bulk synthesis.

6 Conclusions and outlook

To summarize, various metal-organic nano-/microstructures were synthesized on microfluidic systems and their optical and structural properties and their use in sensing applications were investigated.

Regarding the first part of this project “*Label-free biosensors based on in situ formed and functionalized microwires in microfluidic devices*” (Chapter 5.1), an integrated Au-TTF wire-based microfluidic system with sensitive label-free biosensing capability was reported. With this method, the direct sensing of catecholamines involving dopamine and the indirect sensing of human IgG were tested by Raman measurements, both with a detection limit comparable to the one recently reported in other studies,^{148,155} but with the advantage in this work to conduct all the measurements on single wires. However, the so proposed biosensors could not distinguish dopamine from its carbon-hydroxylated product norepinephrine. This is likely attributed to the high similarity in molecular structure of these catecholamines, so that their Raman spectra overlap. This has been found also in previous studies by Raman spectroscopy.¹⁴⁹ However, the two approaches reported here are of general interest for the synthesis and characterization of various metal-organic structures with an active surface. Moreover, this work opens a new route to sensing devices based on *in situ* formed micro- and nanowires with an integrated microfluidic delivering system. In the future, by optimising the alignment and positioning of the wires formed inside the microchip, single micro-/nanowire sensing systems could also be fabricated and used as advanced sensing tools for chemicals and biomolecules.

In the frame of the second part “*Study of molecular self-organization in TTF crystals individual Au-TTF nano-/microwire by polarized confocal Raman spectroscopy*” (Chapter 5.2), the orientation and self-assembly of molecules in both a single TTF crystal and Au-TTF nanowire were studied. The non-destructive polarized confocal Raman spectroscopic analysis on a single TTF crystal proved the preferential ordering of molecules inside the crystal. Supported by the DFT calculations and

simulations of depolarization ratio, the angle between two molecules in a single TTF unit cell was calculated and showed little deviation from that calculated from single crystal X-ray diffraction data. In addition, a single Au-TTF nanowire was studied with the same technique. The result obtained indicated that there were two different molecule configurations in the wire, both tilted with respect to the long axis of wire.

In the frame of the third part “*Conductive single nanowires formed and analysed on microfluidic devices*” (Chapter 5.3), a comprehensive overview of different metal and TTF-based compounds (Table 5.4) was presented and highlighted the influence of the different preparation conditions (such as bulk (non-flow) vs laminar flow conditions) on the resulting morphology. The data obtained proved four-inlet microchip with laminar flow and solvent sheath streams worked efficiently to obtain long and thin nanowires. The conductive behaviour of single nanowires at room temperature proved by electrical characterization and suggested the use of such materials for fabricating nanodevices. A comparison between M-TTF and M-TTF derivatives indicated that M-TTF, M-FTTF and M-BEDT-TTF can lead to the formation of wire structures, while M-TET-TTF and M-TCE-TTF can only form crystals. Thus, for C₁, C₂-position substituted TTF derivatives with sulphur, the planar aromatic ring structure in BEDT-TTF can form stacking structures, much easier than those with short side groups (TET-TTF and TCE-TTF) under the reaction conditions described in this work. Among the M-TTF (and derivatives) systems studied here, the nanowires derived from M-TTF and M-FTTF exhibited high electrical conductivities from 10⁻¹ to 10 S cm⁻¹ at room temperature, one or two orders higher than those for M-BEDT-TTF, in accordance with previously reported work.^{10,13,174} The resulting overview table (Table 5.4) is a means to select TTF-based structures with desired structural and electrical properties, e.g. for sensing applications with a high conductivity. In the future, the use of different TTF-based wire structures for sensing of various analytes e.g. volatile organic compounds, cancer biomarkers could be studied and compared to the sensing platforms proposed so far.

Finally, a second organic ligand TCNQ was discussed in the last part “*Localized synthesis of conductive Cu-TCNQ nanostructures in ultra-small*

microchambers for nanoelectronics” (Chapter 5.4). In particular the microfluidic-based synthesis of conductive Cu-TCNQ in ambient environment at room temperature was achieved. Different morphologies of Cu-TCNQ nano-/microstructures could be synthesized in a controlled way by tuning the concentration of precursors and by changing the reaction time inside microchips. With this technique, reactions were confined in parallel ultra-small microchambers. Thus, the nanostructures were locally formed and integrated with prefabricated microelectrodes, and moreover, their electrical properties could be measured directly, without further micromanipulation. Cu-TCNQ nanostructures formed with the proposed method showed a conductive behaviour and a memory effect, indicating the possibility of using this technique for the building of nanoelectronics and nanoswitches in an easy and efficient way.

In general, each of these four subprojects addresses one or more aspects of the overall topic, i.e., firstly, to find suitable materials for nanowire sensors (Chapter 5.3 and 5.4); secondly, to characterize and understand how the structure is (Chapter 5.2 and 5.3); thirdly, to locally synthesize the wires (Chapter 5.1 and 5.4); lastly, to functionalize them for application as a sensor (Chapter 5.1). By this work, the formation mechanism, synthesis technique, structural properties of TTF and TCNQ-based metal-organic charge-transfer complexes were better understood. However, the synthesis and application of these structures have not been fully investigated, especially for the sensing applications based on conductive wires. In the future, deeper insight into three aspects can be gained: 1) molecular self-organization in TCNQ-based nanostructures, such as Ag-TCNQ and Cu-TCNQ; 2) synthesis of novel metal-organic compounds using different transition metals and bio-ligands; 3) development of novel electrical or optical sensors based on metal-TTF and metal-TCNQ structures widely characterized in this work. In particular, preliminary result in Chapter 5.3.6 had shown the sensing behaviour of conductive Au-TTF for organic gases. A further study in developing gas sensors using TTF/TCNQ-based conductive wires will be very important in building label-free sensing platforms with miniaturized size and high sensitivity.

Bibliography

- [1] Wudl, F.; Smith, G. M.; Hufnagel, E. J. Bis-1,3-dithiolium chloride: an unusually stable organic radical cation, *Journal of the Chemical Society D: Chemical Communications* **1970**, 1453-1454.
- [2] Acker, D. S.; Harder, R. J.; Hertler, W. R.; Mahler, W.; Melby, L. R.; Benson, R. E.; Mochel, W. E. 7,7,8,8-TETRACYANOQUINODIMETHANE AND ITS ELECTRICALLY CONDUCTING ANION-RADICAL DERIVATIVES, *Journal of the American Chemical Society* **1960**, 82, 6408-6409.
- [3] Coleman, L. B.; Cohen, M. J.; Sandman, D. J.; Yamagishi, F. G.; Garito, A. F.; Heeger, A. J. Superconducting fluctuations and the peierls instability in an organic solid, *Solid State Communications* **1973**, 12, 1125-1132.
- [4] Ferraris, J.; Cowan, D. O.; Walatka, V.; Perlstein, J. H. Electron transfer in a new highly conducting donor-acceptor complex, *Journal of the American Chemical Society* **1973**, 95, 948-949.
- [5] Mori, T.; Kawamoto, T. Organic conductors-from fundamentals to nonlinear conductivity, *Annual Reports Section "C" (Physical Chemistry)* **2007**, 103, 134-172.
- [6] Temkin, H.; Fitchen, D. B.; Wudl, F. Raman scattering in TTF crystals, *Solid State Communications* **1977**, 24, 87-92.
- [7] Pou-Américo, R.; Ortí, E.; Merchán, M.; Rubio, M.; Viruela, P. M. Electronic Transitions in Tetrathiafulvalene and Its Radical Cation: A Theoretical Contribution, *The Journal of Physical Chemistry A* **2002**, 106, 631-640.
- [8] Pou-Américo, R.; Viruela, P. M.; Viruela, R.; Rubio, M.; Ortí, E. Electronic spectra of tetrathiafulvalene and its radical cation: analysis of the performance of the time-dependent DFT approach, *Chemical Physics Letters* **2002**, 352, 491-498.
- [9] Nielsen, M. B.; Lomholt, C.; Becher, J. Tetrathiafulvalenes as building blocks in supramolecular chemistry II, *Chemical Society Reviews* **2000**, 29, 153-164.
- [10] Siedle, A. R.; Candela, G. A.; Finnegan, T. F.; Vanduyne, R. P.; Cape, T.; Kokoszka, G. F.; Woyciejes, P. M.; Hashmall, J. A. Copper and Gold Metallotetrathiaethylenes, *Inorganic Chemistry* **1981**, 20, 2635-2640.
- [11] Honda, M.; Katayama, C.; Tanaka, J.; Tanaka, M. Structure of the 2/1 complex dibenzotetrathiafulvalenium hexachlorocuprate(II), $2C_{14}H_8S_4^+ \cdot Cu_2Cl_6^{2-}$, *Acta Crystallographica Section C* **1985**, 41, 197-199.

- [12] Kim, Y. I.; Hatfield, W. E. Electrical, magnetic and spectroscopic properties of tetrathiafulvalene charge transfer compounds with iron, ruthenium, rhodium and iridium halides, *Inorganica Chimica Acta* **1991**, *188*, 15-24.
- [13] Inoue, M. B.; Inoue, M.; Fernando, Q.; Nebesny, K. W. Highly electroconductive tetrathiafulvalenium salts of copper halides, *Inorganic Chemistry* **1986**, *25*, 3976-3980.
- [14] Williams, J. M.; Emge, T. J.; Wang, H. H.; Beno, M. A.; Copps, P. T.; Hall, L. N.; Carlson, K. D.; Crabtree, G. W. Synthetic metals based on bis(ethylenedithio)tetrathiafulvalene (BEDT-TTF): synthesis, structure, and ambient-pressure superconductivity in (BEDT-TTF)₂I₃, *Inorganic Chemistry* **1984**, *23*, 2558-2560.
- [15] Ouahab, L. Organic/Inorganic Supramolecular Assemblies and Synergy between Physical Properties, *Chemistry of Materials* **1997**, *9*, 1909-1926.
- [16] Wudl, F.; Wobschall, D.; Hufnagel, E. J. Electrical conductivity by the bis(1,3-dithiole)-bis(1,3-dithiolium) system, *Journal of the American Chemical Society* **1972**, *94*, 670-672.
- [17] Scott, B. A.; La Placa, S. J.; Torrance, J. B.; Silverman, B. D.; Welber, B. The crystal chemistry of organic metals. Composition, structure, and stability in the tetrathiafulvalinium-halide systems, *Journal of the American Chemical Society* **1977**, *99*, 6631-6639.
- [18] Dahm, D. J.; Horn, P.; Johnson, G. R.; Miles, M. G.; Wilson, J. D. Classification of electrically conducting 'electron-transfer' compounds by crystal structure, *Journal of Crystal and Molecular Structure*, *5*, 27-34.
- [19] Phillips, T. E.; Kistenmacher, T. J.; Ferraris, J. P.; Cowan, D. O. Crystal structure of the radical-cation radical-anion salt from 2,2[prime or minute]-bi-1,3-dithiole and 7,7,8,8-tetracyanoquinodimethane, *Journal of the Chemical Society, Chemical Communications* **1973**, 471-472.
- [20] Kistenmacher, T. J.; Phillips, T. E.; Cowan, D. O. The crystal structure of the 1:1 radical cation-radical anion salt of 2,2'-bis-1,3-dithiole (TTF) and 7,7,8,8-tetracyanoquinodimethane (TCNQ), *Acta Crystallographica Section B* **1974**, *30*, 763-768.
- [21] Furukawa, H.; Cordova, K. E.; O'Keeffe, M.; Yaghi, O. M. The Chemistry and Applications of Metal-Organic Frameworks, *Science* **2013**, *341*.
- [22] Zheng, K. B.; Shen, H. T.; Ye, C. N.; Li, J. L.; Sun, D. L.; Chen, G. R. The electrical switching characteristics of single copper tetra-cyanoquinodimethane nanowire, *Nano-Micro Letters* **2009**, *1*, 23-26.
- [23] Nafady, A.; Bond, A. M.; Bilyk, A.; Harris, A. R.; Bhatt, A. I.; O'Mullane, A. P.; De Marco, R. Tuning the Electrocrystallization Parameters of Semiconducting

Co[TCNQ]₂⁻ Based Materials To Yield either Single Nanowires or Crystalline Thin Films, *Journal of the American Chemical Society* **2007**, *129*, 2369-2382.

[24] Naka, K.; Ando, D.; Wang, X.; Chujo, Y. Synthesis of Organic-Metal Hybrid Nanowires by Cooperative Self-Organization of Tetrathiafulvalene and Metallic Gold via Charge-Transfer, *Langmuir* **2007**, *23*, 3450-3454.

[25] Tanaka, K.; Matsumoto, T.; Ishiguro, F.; Chujo, Y. Conductivity regulation of the mixed-valence tetrathiafulvalene nanowire/poly(methyl methacrylate) composites using heterogeneous tetrathiafulvalene derivatives, *Journal of Materials Chemistry* **2011**, *21*, 9603-9607.

[26] Wang, X.; Itoh, H.; Naka, K.; Chujo, Y. Tetrathiafulvalene-Assisted Formation of Silver Dendritic Nanostructures in Acetonitrile, *Langmuir* **2003**, *19*, 6242-6246.

[27] Puigmarti-Luis, J.; Schaffhauser, D.; Burg, B. R.; Dittrich, P. S. A Microfluidic Approach for the Formation of Conductive Nanowires and Hollow Hybrid Structures, *Advanced Materials* **2010**, *22*, 2255-2259.

[28] Cvetkovic, B. Z.; Puigmarti-Luis, J.; Schaffhauser, D.; Ryll, T.; Schmid, S.; Dittrich, P. S. Confined Synthesis and Integration of Functional Materials in Sub-nanoliter Volumes, *ACS Nano* **2013**, *7*, 183-190.

[29] Kuhn, P.; Puigmarti-Luis, J.; Imaz, I.; MasPOCH, D.; Dittrich, P. S. Controlling the length and location of in situ formed nanowires by means of microfluidic tools, *Lab on a Chip* **2011**, *11*, 753-757.

[30] Taliaferro, M. L.; Palacio, F.; Miller, J. S. The magnetic behaviors of the metamagnetic and ferromagnetic phases of [Fe(C₅MeS)₂][TCNQ] (TCNQ = 7,7,8,8-tetracyano-p-quinodimethane). Determination of the phase diagram for the metamagnetic phase, *Journal of Materials Chemistry* **2006**, *16*, 2677-2684.

[31] Mo, X.-L.; Chen, G.-R.; Cai, Q.-J.; Fan, Z.-Y.; Xu, H.-H.; Yao, Y.; Yang, J.; Gu, H.-H.; Hua, Z.-Y. Preparation and electrical/optical bistable property of potassium tetracyanoquinodimethane thin films, *Thin Solid Films* **2003**, *436*, 259-263.

[32] Teresa Azcondo, M.; Ballester, L.; Golhen, S.; Gutierrez, A.; Ouahab, L.; Yartsev, S.; Delhaes, P. Structural, magnetic, electrical and optical characterization of systems built from [M([9]aneN₃)₂]²⁺ (M=Cu^{II} or Ni^{II}) and TCNQ or TCNQF₄, *Journal of Materials Chemistry* **1999**, *9*, 1237-1244.

[33] Wooster, T. J.; Bond, A. M. Ion selectivity obtained under voltammetric conditions when a TCNQ chemically modified electrode is presented with aqueous solutions containing tetraalkylammonium cations, *Analyst* **2003**, *128*, 1386-1390.

[34] Bartley, S. L.; Dunbar, K. R. [{Re₂Cl₄(dppm)₂]₂ (μ-TCNQ)], a Novel Charge Transfer Complex Derived from a Donor with a Metal-Metal Multiple Bond, *Angewandte Chemie International Edition in English* **1991**, *30*, 448-450.

- [35] Oshio, H.; Ino, E.; Mogi, I.; Ito, T. A weak antiferromagnetic interaction between manganese(²⁺) centers through a TCNQ column: crystal structures and magnetic properties of [Mn^{II}(tpa)(TCNQ)(CH₃OH)](TCNQ)₂.CH₃CN, [Mn^{II}(tpa)(μ-O₂CCH₃)₂(TCNQ)₂.2CH₃CN, and [Mn^{II}(tpa)(NCS)₂].CH₃CN (tpa = tris(2-pyridylmethyl)amine), *Inorganic Chemistry* **1993**, 32, 5697-5703.
- [36] Zhao, H.; Heintz, R. A.; Dunbar, K. R.; Rogers, R. D. Unprecedented Two-Dimensional Polymers of Mn(II) with TCNQ-• (TCNQ = 7,7,8,8-Tetracyanoquinodimethane), *Journal of the American Chemical Society* **1996**, 118, 12844-12845.
- [37] Torrance, J. B. An Overview of Organic Charge-Transfer Solids: Insulators, Metals, and the Neutral-Ionic Transition, *Molecular Crystals and Liquid Crystals* **1985**, 126, 55-67.
- [38] Potember, R. S.; Poehler, T. O.; Cowan, D. O. Electrical switching and memory phenomena in Cu-TCNQ thin films, *Applied Physics Letters* **1979**, 34, 405-407.
- [39] Heintz, R. A.; Zhao, H.; Ouyang, X.; Grandinetti, G.; Cowen, J.; Dunbar, K. R. New Insight into the Nature of Cu(TCNQ): Solution Routes to Two Distinct Polymorphs and Their Relationship to Crystalline Films That Display Bistable Switching Behavior, *Inorganic Chemistry* **1999**, 38, 144-156.
- [40] Huibiao, L.; Junbo, L.; Changshi, L.; Changshui, H.; Yuliang, L.; Zhong Lin, W.; Daoben, Z. Morphological tuning and conductivity of organic conductor nanowires, *Nanotechnology* **2007**, 18, 495704.
- [41] Liu, H.; Zhao, Q.; Li, Y.; Liu, Y.; Lu, F.; Zhuang, J.; Wang, S.; Jiang, L.; Zhu, D.; Yu, D.; Chi, L. Field Emission Properties of Large-Area Nanowires of Organic Charge-Transfer Complexes, *Journal of the American Chemical Society* **2005**, 127, 1120-1121.
- [42] Kepler, R. G.; Bierstedt, P. E.; Merrifield, R. E. Electronic Conduction and Exchange Interaction in a New Class of Conductive Organic Solids, *Physical Review Letters* **1960**, 5, 503-504.
- [43] Sato, C.; Wakamatsu, S.; Tadokoro, K.; Ishii, K. Polarized memory effect in the device including the organic charge-transfer complex, copper-tetracyanoquinodimethane, *Journal of Applied Physics* **1990**, 68, 6535-6537.
- [44] Kamitsos, E. I.; Tzinis, C. H.; Risen Jr, W. M. Raman study of the mechanism of electrical switching in Cu TCNQ films, *Solid State Communications* **1982**, 42, 561-565.
- [45] Müller, R.; De Jonge, S.; Myny, K.; Wouters, D. J.; Genoe, J.; Heremans, P. Organic CuTCNQ integrated in complementary metal oxide semiconductor copper back end-of-line for nonvolatile memories, *Applied Physics Letters* **2006**, 89, 223501.

- [46] Law, M.; Goldberger, J.; Yang, P. SEMICONDUCTOR NANOWIRES AND NANOTUBES, *Annual Review of Materials Research* **2004**, *34*, 83-122.
- [47] Kong, J.; Franklin, N. R.; Zhou, C.; Chapline, M. G.; Peng, S.; Cho, K.; Dai, H. Nanotube Molecular Wires as Chemical Sensors, *Science* **2000**, *287*, 622-625.
- [48] Han, S. W.; Lee, S.; Hong, J.; Jang, E.; Lee, T.; Koh, W.-G. Mutiscale substrates based on hydrogel-incorporated silicon nanowires for protein patterning and microarray-based immunoassays, *Biosensors and Bioelectronics* **2013**, *45*, 129-135.
- [49] Lee, M.; Baik, K. Y.; Noah, M.; Kwon, Y. K.; Lee, J. O.; Hong, S. Nanowire and nanotube transistors for lab-on-a-chip applications, *Lab on a Chip* **2009**, *9*, 2267-2280.
- [50] Cui, Y.; Wei, Q.; Park, H.; Lieber, C. M. Nanowire Nanosensors for Highly Sensitive and Selective Detection of Biological and Chemical Species, *Science* **2001**, *293*, 1289-1292.
- [51] Puigmarti-Luis, J.; Stadler, J.; Schaffhauser, D.; del Pino, A. P.; Burg, B. R.; Dittrich, P. S. Guided assembly of metal and hybrid conductive probes using floating potential dielectrophoresis, *Nanoscale* **2011**, *3*, 937-940.
- [52] Hoeben, F. J. M.; Jonkheijm, P.; Meijer, E. W.; Schenning, A. P. H. J. About Supramolecular Assemblies of π -Conjugated Systems, *Chemical Reviews* **2005**, *105*, 1491-1546.
- [53] Gan, H.; Liu, H.; Li, Y.; Zhao, Q.; Li, Y.; Wang, S.; Jiu, T.; Wang, N.; He, X.; Yu, D.; Zhu, D. Fabrication of Polydiacetylene Nanowires by Associated Self-Polymerization and Self-Assembly Processes for Efficient Field Emission Properties, *Journal of the American Chemical Society* **2005**, *127*, 12452-12453.
- [54] Clayton, D. A.; McPherson, T. E.; Pan, S.; Chen, M.; Dixon, D. A.; Hu, D. Spatial and temporal variation of surface-enhanced Raman scattering at Ag nanowires in aqueous solution, *Physical Chemistry Chemical Physics* **2013**, *15*, 850-859.
- [55] Park, K. S.; Cho, B.; Baek, J.; Hwang, J. K.; Lee, H.; Sung, M. M. Single-Crystal Organic Nanowire Electronics by Direct Printing from Molecular Solutions, *Advanced Functional Materials* **2013**, *23*, 4776-4784.
- [56] Chen, X.; Kis, A.; Zettl, A.; Bertozzi, C. R. A cell nanoinjector based on carbon nanotubes, *Proceedings of the National Academy of Sciences* **2007**, *104*, 8218-8222.
- [57] Kemp, N. T.; McGrouther, D.; Cochrane, J. W.; Newbury, R. Bridging the Gap: Polymer Nanowire Devices, *Advanced Materials* **2007**, *19*, 2634-2638.
- [58] Puigmartí-Luis, J.; Rubio-Martínez, M.; Hartfelder, U.; Imaz, I.; Maspocho, D.; Dittrich, P. S. Coordination Polymer Nanofibers Generated by Microfluidic Synthesis, *Journal of the American Chemical Society* **2011**, *133*, 4216-4219.

- [59] Imaz, I.; Rubio-Martínez, M.; Saletta, W. J.; Amabilino, D. B.; Maspoch, D. Amino Acid Based Metal–Organic Nanofibers, *Journal of the American Chemical Society* **2009**, *131*, 18222-18223.
- [60] Rieter, W. J.; Taylor, K. M. L.; An, H.; Lin, W.; Lin, W. Nanoscale Metal–Organic Frameworks as Potential Multimodal Contrast Enhancing Agents, *Journal of the American Chemical Society* **2006**, *128*, 9024-9025.
- [61] Hou, S.; Harrell, C. C.; Trofin, L.; Kohli, P.; Martin, C. R. Layer-by-Layer Nanotube Template Synthesis, *Journal of the American Chemical Society* **2004**, *126*, 5674-5675.
- [62] Li, Y.; Yang, X.-Y.; Feng, Y.; Yuan, Z.-Y.; Su, B.-L. One-Dimensional Metal Oxide Nanotubes, Nanowires, Nanoribbons, and Nanorods: Synthesis, Characterizations, Properties and Applications, *Critical Reviews in Solid State and Materials Sciences* **2012**, *37*, 1-74.
- [63] Xia, Y.; Yang, P.; Sun, Y.; Wu, Y.; Mayers, B.; Gates, B.; Yin, Y.; Kim, F.; Yan, H. One-Dimensional Nanostructures: Synthesis, Characterization, and Applications, *Advanced Materials* **2003**, *15*, 353-389.
- [64] Spokoyny, A. M.; Kim, D.; Sumrein, A.; Mirkin, C. A. Infinite coordination polymer nano- and microparticle structures, *Chemical Society Reviews* **2009**, *38*, 1218-1227.
- [65] Zhang, X.; Chen, Z.-K.; Loh, K. P. Coordination-Assisted Assembly of 1-D Nanostructured Light-Harvesting Antenna, *Journal of the American Chemical Society* **2009**, *131*, 7210-7211.
- [66] McDowell, J. J.; Zacharia, N. S.; Puzzo, D.; Manners, I.; Ozin, G. A. Electroactuation of Alkoxysilane-Functionalized Polyferrocenylsilane Microfibers, *Journal of the American Chemical Society* **2010**, *132*, 3236-3237.
- [67] Wang, J.-J.; Dai, L.-X.; Gao, Q.; Wu, P.-F.; Wang, X.-B. Electrospun nanofibers of polyferrocenylsilanes with different substituents at silicon, *European Polymer Journal* **2008**, *44*, 602-607.
- [68] Zhang, S.; Yang, S.; Lan, J.; Tang, Y.; Xue, Y.; You, J. Ultrasound-Induced Switching of Sheetlike Coordination Polymer Microparticles to Nanofibers Capable of Gelating Solvents, *Journal of the American Chemical Society* **2009**, *131*, 1689-1691.
- [69] Hui, J. K. H.; MacLachlan, M. J. Metal-containing nanofibers via coordination chemistry, *Coordination Chemistry Reviews* **2010**, *254*, 2363-2390.
- [70] Carne, A.; Carbonell, C.; Imaz, I.; Maspoch, D. Nanoscale metal-organic materials, *Chemical Society Reviews* **2011**, *40*, 291-305.
- [71] Terry, S. C.; Jerman, J. H.; Angell, J. B. A gas chromatographic air analyzer fabricated on a silicon wafer, *IEEE Transactions on Electron Devices* **1979**, *26*, 1880-1886.

- [72] Manz, A.; Graber, N.; Widmer, H. M. Miniaturized total chemical analysis systems: A novel concept for chemical sensing, *Sensors and Actuators B: Chemical* **1990**, *1*, 244-248.
- [73] Whitesides, G. M. The origins and the future of microfluidics, *Nature* **2006**, *442*, 368-373.
- [74] Avila, K.; Moxey, D.; de Lozar, A.; Avila, M.; Barkley, D.; Hof, B. The Onset of Turbulence in Pipe Flow, *Science* **2011**, *333*, 192-196.
- [75] Duffy, D. C.; McDonald, J. C.; Schueller, O. J. A.; Whitesides, G. M. Rapid Prototyping of Microfluidic Systems in Poly(dimethylsiloxane), *Analytical Chemistry* **1998**, *70*, 4974-4984.
- [76] Unger, M. A.; Chou, H.-P.; Thorsen, T.; Scherer, A.; Quake, S. R. Monolithic Microfabricated Valves and Pumps by Multilayer Soft Lithography, *Science* **2000**, *288*, 113-116.
- [77] Schaffhauser, D. F.; Andriani, O.; Ghezzi, C.; Forster, I. C.; Franco-Obregon, A.; Egli, M.; Dittrich, P. S. Microfluidic platform for electrophysiological studies on *Xenopus laevis* oocytes under varying gravity levels, *Lab on a Chip* **2011**, *11*, 3471-3478.
- [78] Küster, S. K.; Fagerer, S. R.; Verboket, P. E.; Eyer, K.; Jefimovs, K.; Zenobi, R.; Dittrich, P. S. Interfacing Droplet Microfluidics with Matrix-Assisted Laser Desorption/Ionization Mass Spectrometry: Label-Free Content Analysis of Single Droplets, *Analytical Chemistry* **2013**, *85*, 1285-1289.
- [79] Stamou, D.; Duschl, C.; Delamarche, E.; Vogel, H. Self-Assembled Microarrays of Attoliter Molecular Vessels, *Angewandte Chemie* **2003**, *115*, 5738-5741.
- [80] Cooksey, G. A.; Elliott, J. T.; Plant, A. L. Reproducibility and Robustness of a Real-Time Microfluidic Cell Toxicity Assay, *Analytical Chemistry* **2011**, *83*, 3890-3896.
- [81] Park, J. I.; Saffari, A.; Kumar, S.; Günther, A.; Kumacheva, E. Microfluidic Synthesis of Polymer and Inorganic Particulate Materials, *Annual Review of Materials Research* **2010**, *40*, 415-443.
- [82] Song, Y.; Holmes, J.; Kumar, C. S. S. R. Microfluidic Synthesis of Nanomaterials, *Small* **2008**, *4*, 698-711.
- [83] Dittrich, P. S.; Manz, A. Lab-on-a-chip: microfluidics in drug discovery, *Nature Reviews Drug Discovery* **2006**, *5*, 210-218.
- [84] El-Ali, J.; Sorger, P. K.; Jensen, K. F. Cells on chips, *Nature* **2006**, *442*, 403-411.
- [85] Gerber, D.; Maerkl, S. J.; Quake, S. R. An in vitro microfluidic approach to generating protein-interaction networks, *Nature Methods* **2009**, *6*, 71-74.

- [86] Hong, B. H.; Bae, S. C.; Lee, C.-W.; Jeong, S.; Kim, K. S. Ultrathin Single-Crystalline Silver Nanowire Arrays Formed in an Ambient Solution Phase, *Science* **2001**, *294*, 348-351.
- [87] Lee, J.-K.; Koh, W.-K.; Chae, W.-S.; Kim, Y.-R. Novel synthesis of organic nanowires and their optical properties, *Chemical Communications* **2002**, 138-139.
- [88] Tian, B.; Zheng, X.; Kempa, T. J.; Fang, Y.; Yu, N.; Yu, G.; Huang, J.; Lieber, C. M. Coaxial silicon nanowires as solar cells and nanoelectronic power sources, *Nature* **2007**, *449*, 885-889.
- [89] Gomar-Nadal, E.; Puigmarti-Luis, J.; Amabilino, D. B. Assembly of functional molecular nanostructures on surfaces, *Chemical Society Reviews* **2008**, *37*, 490-504.
- [90] García, M.; Batalla, P.; Escarpa, A. Metallic and polymeric nanowires for electrochemical sensing and biosensing, *TrAC Trends in Analytical Chemistry* **2014**, *57*, 6-22.
- [91] Kenis, P. J. A.; Ismagilov, R. F.; Whitesides, G. M. Microfabrication Inside Capillaries Using Multiphase Laminar Flow Patterning, *Science* **1999**, *285*, 83-85.
- [92] Pumera, M. Nanomaterials meet microfluidics, *Chemical Communications* **2011**, *47*, 5671-5680.
- [93] Dendukuri, D.; Pregibon, D. C.; Collins, J.; Hatton, T. A.; Doyle, P. S. Continuous-flow lithography for high-throughput microparticle synthesis, *Nature Materials* **2006**, *5*, 365-369.
- [94] Edel, J. B.; Fortt, R.; deMello, J. C.; deMello, A. J. Microfluidic routes to the controlled production of nanoparticles, *Chemical Communications* **2002**, 1136-1137.
- [95] Wang, Z.; Bao, R.; Zhang, X.; Ou, X.; Lee, C.-S.; Chang, J. C.; Zhang, X. One-Step Self-Assembly, Alignment, and Patterning of Organic Semiconductor Nanowires by Controlled Evaporation of Confined Microfluids, *Angewandte Chemie International Edition* **2011**, *50*, 2811-2815.
- [96] Jahn, A.; Vreeland, W. N.; Gaitan, M.; Locascio, L. E. Controlled Vesicle Self-Assembly in Microfluidic Channels with Hydrodynamic Focusing, *Journal of the American Chemical Society* **2004**, *126*, 2674-2675.
- [97] Eyer, K.; Stratz, S.; Kuhn, P.; Küster, S. K.; Dittrich, P. S. Implementing Enzyme-Linked Immunosorbent Assays on a Microfluidic Chip To Quantify Intracellular Molecules in Single Cells, *Analytical Chemistry* **2013**, *85*, 3280-3287.
- [98] Wang, J.; Bunimovich, Y. L.; Sui, G.; Savvas, S.; Wang, J.; Guo, Y.; Heath, J. R.; Tseng, H.-R. Electrochemical fabrication of conducting polymer nanowires in an integrated microfluidic system, *Chemical Communications* **2006**, 3075-3077.
- [99] Puigmarti-Luis, J.; Rubio-Martínez, M.; Imaz, I.; Cvetković, B. Z.; Abad, L.; Pérez del Pino, A.; MasPOCH, D.; Amabilino, D. B. Localized, Stepwise Template

Growth of Functional Nanowires from an Amino Acid-Supported Framework in a Microfluidic Chip, *ACS Nano* **2014**, 8, 818-826.

[100] Xing, Y.; Wyss, A.; Esser, N.; Dittrich, P. S. Label-free biosensors based on in situ formed and functionalized microwires in microfluidic devices, *Analyst* **2015**, 7896-7901.

[101] Eyer, K.; Kuhn, P.; Hanke, C.; Dittrich, P. S. A microchamber array for single cell isolation and analysis of intracellular biomolecules, *Lab on a Chip* **2012**, 12, 765-772.

[102] Boulron, B.; Wong, J.; Miko, C.; Forro, L.; Bockrath, M. A nanoscale probe for fluidic and ionic transport, *Nature Nanotechnology* **2007**, 2, 104-107.

[103] Cvetković, B. Z. PhD thesis, ETH ZURICH, 2012.

[104] Xia, Y.; Whitesides, G. M. Soft Lithography, *Angewandte Chemie International Edition* **1998**, 37, 550-575.

[105] Lisensky, G. C.; Campbell, D. J.; Beckman, K. J.; Calderon, C. E.; Doolan, P. W.; Rebecca, M. O.; Ellis, A. B. Replication and Compression of Surface Structures with Polydimethylsiloxane Elastomer, *Journal of Chemical Education* **1999**, 76, 537.

[106] Etchegoin, E. C. L. R. a. P. G. In *Principles of Surface-Enhanced Raman Spectroscopy*; Elsevier: Oxford UK, 2009.

[107] Kneipp, J.; Schut, T. B.; Kliffen, M.; Menke-Pluijmers, M.; Puppels, G. Characterization of breast duct epithelia: a Raman spectroscopic study, *Vibrational Spectroscopy* **2003**, 32, 67-74.

[108] Speiser, E.; Hinrichs, K.; Prete, P.; Lovergine, N.; Esser, N. Vibrational Raman scattering from surfaces of III–V semiconductors: Microscopic and macroscopic surface modes, *physica status solidi (b)* **2015**, 252, 11-18.

[109] Friedrich Siebert, P. H. In *Vibrational Spectroscopy in Life Science*; WILEY-VCH: Weinheim, 2008; Vol. 2.

[110] Long, D. A. *The Raman Effect: A Unified Treatment of the Theory of Raman Scattering by Molecules*; John Wiley & Sons Ltd: Chichester, 2002.

[111] Ewen Smith, G. D. *Modern Raman Spectroscopy: A Practical Approach*; John Wiley & Sons, Ltd., 2005.

[112] Zahn, D. R. T.; Gavrilă, G. N.; Salvan, G. Electronic and Vibrational Spectroscopies Applied to Organic/Inorganic Interfaces, *Chemical Reviews* **2007**, 107, 1161-1232.

[113] Griffiths, D. J. *Introduction to Electrodynamics*; 3rd ed.; Pearson Education, Dorling Kindersley, 2007.

- [114] Kasap, S. O. In *Principles of Electronic Materials and Devices*; 3rd ed.; S., M., Ed.; McGraw-Hill: New York, 2006.
- [115] Opilik, L.; Schmid, T.; Zenobi, R. Modern Raman Imaging: Vibrational Spectroscopy on the Micrometer and Nanometer Scales, *Annual Review of Analytical Chemistry* **2013**, *6*, 379-398.
- [116] Pézolet, M.; Nafie, L. A.; Peticolas, W. L. Complete polarization measurements for non-symmetric Raman tensors: Symmetry assignments of ferrocycytochrome C vibrations, *Journal of Raman Spectroscopy* **1973**, *1*, 455-464.
- [117] Cardona, M. In *Light Scattering in Solids II*; Güntherodt, M. C. a. G., Ed.; Springer: Berlin, Germany, 1982.
- [118] Brosseau, C. *Fundamentals of polarized light: a statistical optics approach*; Wiley: Germany, 1998.
- [119] John R. Ferraro, K. N. a. C. W. B. *Introductory Raman Spectroscopy*; Academic Press: San Diego: San Diego, CA 1994.
- [120] Allemand, C. D. Depolarization Ratio Measurements in Raman Spectrometry, *Applied Spectroscopy* **1970**, *24*, 348-353.
- [121] Ko, A. C. T.; Choo-Smith, L.-P. i.; Hewko, M.; Sowa, M. G.; Dong, C. C. S.; Cleghorn, B. Detection of early dental caries using polarized Raman spectroscopy, *Optics Express* **2006**, *14*, 203-215.
- [122] Wang, Y.; Yan, B.; Chen, L. SERS Tags: Novel Optical Nanoprobes for Bioanalysis, *Chemical Reviews* **2013**, *113*, 1391-1428.
- [123] Fabris, L.; Dante, M.; Nguyen, T.-Q.; Tok, J. B. H.; Bazan, G. C. SERS Aptatags: New Responsive Metallic Nanostructures for Heterogeneous Protein Detection by Surface Enhanced Raman Spectroscopy, *Advanced Functional Materials* **2008**, *18*, 2518-2525.
- [124] Pauzauskie, P. J.; Talaga, D.; Seo, K.; Yang, P.; Lagugné-Labarthe, F. Polarized Raman Confocal Microscopy of Single Gallium Nitride Nanowires, *Journal of the American Chemical Society* **2005**, *127*, 17146-17147.
- [125] Fréchette, J.; Carraro, C. Resolving Radial Composition Gradients in Polarized Confocal Raman Spectra of Individual 3C-SiC Nanowires, *Journal of the American Chemical Society* **2006**, *128*, 14774-14775.
- [126] Yu, T.; Zhao, X.; Shen, Z. X.; Wu, Y. H.; Su, W. H. Investigation of individual CuO nanorods by polarized micro-Raman scattering, *Journal of Crystal Growth* **2004**, *268*, 590-595.
- [127] Johnsen, S. *The Optics of Life: A Biologist's Guide to Light in Nature*; Princeton Univ. Press. , 2012.
- [128] In *Porto's notation*; Bilbao Crystallographic Server.

- [129] Lim, C.; Hong, J.; Chung, B. G.; deMello, A. J.; Choo, J. Optofluidic platforms based on surface-enhanced Raman scattering, *Analyst* **2010**, *135*, 837-844.
- [130] Batsanov, A. S. Tetrathiafulvalene revisited, *Acta Crystallographica Section C-Crystal Structure Communications* **2006**, *62*, O501-O504.
- [131] Wudl, F.; Kaplan, M. L.; Hufnagel, E. J.; Southwick, E. W. Convenient synthesis of 1,4,5,8-tetrahydro-1,4,5,8-tetrathiafulvalene, *The Journal of Organic Chemistry* **1974**, *39*, 3608-3609.
- [132] Frisch, M. J. T.; G. W.; Schlegel, H. B.; Scuseria, G. E.; Robb, M. A.; Cheeseman, J. R.; Scalmani, G.; Barone, V.; Mennucci, B.; Petersson, G. A.; Nakatsuji, H.; Caricato, M.; Li, X.; Hratchian, H. P.; Izmaylov, A. F.; Bloino, J.; Zheng, G.; Sonnenberg, J. L.; Hada, M.; Ehara, M.; Toyota, K.; Fukuda, R.; Hasegawa, J.; Ishida, M.; Nakajima, T.; Honda, Y.; Kitao, O.; Nakai, H.; Vreven, T.; Montgomery, J. A., Jr.; Peralta, J. E.; Ogliaro, F.; Bearpark, M.; Heyd, J. J.; Brothers, E.; Kudin, K. N.; Staroverov, V. N.; Kobayashi, R.; Normand, J.; Raghavachari, K.; Rendell, A.; Burant, J. C.; Iyengar, S. S.; Tomasi, J.; Cossi, M.; Rega, N.; Millam, J. M.; Klene, M.; Knox, J. E.; Cross, J. B.; Bakken, V.; Adamo, C.; Jaramillo, J.; Gomperts, R.; Stratmann, R. E.; Yazyev, O.; Austin, A. J.; Cammi, R.; Pomelli, C.; Ochterski, J. W.; Martin, R. L.; Morokuma, K.; Zakrzewski, V. G.; Voth, G. A.; Salvador, P.; Dannenberg, J. J.; Dapprich, S.; Daniels, A. D.; Farkas, Ö.; Foresman, J. B.; Ortiz, J. V.; Cioslowski, J.; Fox, D. J.; Gaussian, I. W. C., Ed. 2009.
- [133] Singh, D.; Vikram, K.; Singh, D. K.; Kiefer, W.; Singh, R. K. Raman and DFT study of hydrogen-bonded 2- and 3-chloropyridine with methanol, *Journal of Raman Spectroscopy* **2008**, *39*, 1423-1432.
- [134] Singh, D. K.; Srivastava, S. K.; Schlücker, S.; Singh, R. K.; Asthana, B. P. Self-association and hydrogen bonding of propionaldehyde in binary mixtures with water and methanol investigated by concentration-dependent polarized Raman study and DFT calculations, *Journal of Raman Spectroscopy* **2011**, *42*, 851-858.
- [135] Singh, D. K. A., B. P.; Srivastava, S. K. Modeling the weak hydrogen bonding of pyrrole and dichloromethane through Raman and DFT study, *Journal of Molecular Modeling* **2012**, *18* (8), 3541-3552.
- [136] Lam, A. T. N.; Yoon, J.; Ganbold, E.-O.; Singh, D. K.; Kim, D.; Cho, K.-H.; Son, S. J.; Choo, J.; Lee, S. Y.; Kim, S.; Joo, S.-W. Adsorption and desorption of tyrosine kinase inhibitor erlotinib on gold nanoparticles, *Journal of Colloid and Interface Science* **2014**, *425*, 96-101.
- [137] Lam, A. T. N.; Yoon, J.; Ganbold, E.-O.; Singh, D. K.; Kim, D.; Cho, K.-H.; Lee, S. Y.; Choo, J.; Lee, K.; Joo, S.-W. Colloidal gold nanoparticle conjugates of gefitinib, *Colloids and Surfaces B: Biointerfaces* **2014**, *123*, 61-67.

- [138] Lee, M.; Baik, K. Y.; Noah, M.; Kwon, Y.-K.; Lee, J.-O.; Hong, S. Nanowire and nanotube transistors for lab-on-a-chip applications, *Lab on a Chip* **2009**, 9, 2267-2280.
- [139] Hou, S.; Wang, S.; Yu, Z. T. F.; Zhu, N. Q. M.; Liu, K.; Sun, J.; Lin, W.-Y.; Shen, C. K. F.; Fang, X.; Tseng, H.-R. A Hydrodynamically Focused Stream as a Dynamic Template for Site-Specific Electrochemical Micropatterning of Conducting Polymers, *Angewandte Chemie International Edition* **2008**, 47, 1072-1075.
- [140] Kim, J.; Li, Z.; Park, I. Direct synthesis and integration of functional nanostructures in microfluidic devices, *Lab on a Chip* **2011**, 11, 1946-1951.
- [141] Comini, E.; Baratto, C.; Faglia, G.; Ferroni, M.; Vomiero, A.; Sberveglieri, G. Quasi-one dimensional metal oxide semiconductors: Preparation, characterization and application as chemical sensors, *Progress in Materials Science* **2009**, 54, 1-67.
- [142] Patolsky, F.; Zheng, G.; Lieber, C. M. Nanowire-Based Biosensors, *Analytical Chemistry* **2006**, 78, 4260-4269.
- [143] Chen, R. J.; Bangsaruntip, S.; Drouvalakis, K. A.; Wong Shi Kam, N.; Shim, M.; Li, Y.; Kim, W.; Utz, P. J.; Dai, H. Noncovalent functionalization of carbon nanotubes for highly specific electronic biosensors, *Proceedings of the National Academy of Sciences* **2003**, 100, 4984-4989.
- [144] Besteman, K.; Lee, J.-O.; Wiertz, F. G. M.; Heering, H. A.; Dekker, C. Enzyme-Coated Carbon Nanotubes as Single-Molecule Biosensors, *Nano Letters* **2003**, 3, 727-730.
- [145] Huynh, W. U.; Dittmer, J. J.; Alivisatos, A. P. Hybrid Nanorod-Polymer Solar Cells, *Science* **2002**, 295, 2425-2427.
- [146] Love, J. C.; Estroff, L. A.; Kriebel, J. K.; Nuzzo, R. G.; Whitesides, G. M. Self-Assembled Monolayers of Thiolates on Metals as a Form of Nanotechnology, *Chemical Reviews* **2005**, 105, 1103-1170.
- [147] Han, X. X.; Chen, L.; Ji, W.; Xie, Y.; Zhao, B.; Ozaki, Y. Label-Free Indirect Immunoassay Using an Avidin-Induced Surface-Enhanced Raman Scattering Substrate, *Small* **2011**, 7, 316-320.
- [148] Kho, K. W.; Dinis, U. S.; Kumar, A.; Olivo, M. Frequency Shifts in SERS for Biosensing, *ACS Nano* **2012**, 6, 4892-4902.
- [149] Volkan, M.; Stokes, D. L.; Vo-Dinh, T. Surface-Enhanced Raman of Dopamine and Neurotransmitters Using Sol-Gel Substrates and Polymer-Coated Fiber-Optic Probes, *Applied Spectroscopy* **2000**, 54, 1842-1848.
- [150] Wang, Y.; Lee, K.; Irudayaraj, J. SERS aptasensor from nanorod-nanoparticle junction for protein detection, *Chemical Communications* **2010**, 46, 613-615.

- [151] Miller, A. W.; Robyt, J. F. Sodium cyanoborohydride in the immobilization of proteins to glutaraldehyde-activated aminoalkyl silica, *Biotechnology and Bioengineering* **1983**, *25*, 2795-2800.
- [152] Sasso, L.; Heiskanen, A.; Diazzi, F.; Dimaki, M.; Castillo-Leon, J.; Vergani, M.; Landini, E.; Raiteri, R.; Ferrari, G.; Carminati, M.; Sampietro, M.; Svendsen, W. E.; Emneus, J. Doped overoxidized polypyrrole microelectrodes as sensors for the detection of dopamine released from cell populations, *Analyst* **2013**, *138*, 3651-3659.
- [153] Mcglashen, M. L.; Davis, K. L.; Morris, M. D. Surface-Enhanced Raman-Scattering of Dopamine at Polymer-Coated Silver Electrodes, *Analytical Chemistry* **1990**, *62*, 846-849.
- [154] Lee, N. S.; Hsieh, Y. Z.; Paisley, R. F.; Morris, M. D. Surface-enhanced Raman spectroscopy of the catecholamine neurotransmitters and related compounds, *Analytical Chemistry* **1988**, *60*, 442-446.
- [155] Oh, Y. J.; Jeong, K. H. Optofluidic SERS chip with plasmonic nanoprobes self-aligned along microfluidic channels, *Lab on a Chip* **2014**, *14*, 865-868.
- [156] Perumal, J.; Kong, K. V.; Dinish, U. S.; Bakker, R. M.; Olivo, M. Design and fabrication of random silver films as substrate for SERS based nano-stress sensing of proteins, *RSC Advances* **2014**, *4*, 12995-13000.
- [157] Li, M.; Cushing, S. K.; Zhang, J.; Suri, S.; Evans, R.; Petros, W. P.; Gibson, L. F.; Ma, D.; Liu, Y.; Wu, N. Three-Dimensional Hierarchical Plasmonic Nano-Architecture Enhanced Surface-Enhanced Raman Scattering Immunosensor for Cancer Biomarker Detection in Blood Plasma, *ACS Nano* **2013**, *7*, 4967-4976.
- [158] Hu, X. G.; Wang, T.; Wang, L.; Dong, S. J. Surface-enhanced Raman scattering of 4-aminothiophenol self-assembled monolayers in sandwich structure with nanoparticle shape dependence: Off-surface plasmon resonance condition, *Journal of Physical Chemistry C* **2007**, *111*, 6962-6969.
- [159] Cao, L.; Diao, P.; Tong, L.; Zhu, T.; Liu, Z. Surface-Enhanced Raman Scattering of p-Aminothiophenol on a Au(core)/Cu(shell) Nanoparticle Assembly, *ChemPhysChem* **2005**, *6*, 913-918.
- [160] Katan, C. First-Principles Study of the Structures and Vibrational Frequencies for Tetrathiafulvalene TTF and TTF-d4 in Different Oxidation States, *The Journal of Physical Chemistry A* **1999**, *103*, 1407-1413.
- [161] Ferraro, J. R. N., K. In *Introductory Raman Spectroscopy*; Academic Press: San Diego: CA, 1999.
- [162] Cooper, W. F.; Kenny, N. C.; Edmonds, J. W.; Nagel, A.; Wudl, F.; Coppens, P. Crystal and molecular structure of the aromatic sulphur compound 2,2[prime or minute]-bi-1,3-dithiole. Evidence for d-orbital participation in bonding, *Journal of the Chemical Society D: Chemical Communications* **1971**, 889-890.

- [163] Cooper, W. F. E., J. W.; Wudl, F.; Coppens, P. The 2-2'-bi-1,3-dithiole, *Crystal Structure Communications* **1974**, *3*, 23-26.
- [164] Sandman, D. J.; Epstein, A. J.; Chickos, J. S.; Ketchum, J.; Fu, J. S.; Scheraga, H. A. Crystal lattice and polarization energy of tetrathiafulvalene, *The Journal of Chemical Physics* **1979**, *70*, 305-313.
- [165] Berlinsky, A. J.; Hoyano, Y.; Weiler, L. Raman spectra of tetrathiofulvalene (TTF), *Chemical Physics Letters* **1977**, *45*, 419-421.
- [166] Bangar, M. A.; Shirale, D. J.; Chen, W.; Myung, N. V.; Mulchandani, A. Single Conducting Polymer Nanowire Chemiresistive Label-Free Immunosensor for Cancer Biomarker, *Analytical Chemistry* **2009**, *81*, 2168-2175.
- [167] Pescaglini, A.; Iacopino, D. Metal nanoparticle-semiconductor nanowire hybrid nanostructures for plasmon-enhanced optoelectronics and sensing, *Journal of Materials Chemistry C* **2015**, *3*, 11785-11800.
- [168] Bryce, M. R. Tetrathiafulvalenes as π -Electron Donors for Intramolecular Charge-Transfer Materials, *Advanced Materials* **1999**, *11*, 11-23.
- [169] Suzuki, W.; Fujiwara, E.; Kobayashi, A.; Fujishiro, Y.; Nishibori, E.; Takata, M.; Sakata, M.; Fujiwara, H.; Kobayashi, H. Highly Conducting Crystals Based on Single-Component Gold Complexes with Extended-TTF Dithiolate Ligands, *Journal of the American Chemical Society* **2003**, *125*, 1486-1487.
- [170] Segura, J. L.; Martín, N. New Concepts in Tetrathiafulvalene Chemistry, *Angewandte Chemie International Edition* **2001**, *40*, 1372-1409.
- [171] Choi, S. N.; Jung, W. S.; Lee, M. J.; Lee, Y. M.; Kim, Y. I. Synthesis and physicochemical properties of charge transfer compounds derived from the reaction of tetrathiafulvalene with copper(II), *Polyhedron* **2004**, *23*, 2111-2115.
- [172] Naka, K.; Ando, D.; Chujo, Y. Effect of substituent groups for formation of organic-metal hybrid nanowires by charge-transfer of tetrathiafulvalene derivatives with metal ion, *Synthetic Metals* **2009**, *159*, 931-934.
- [173] Geng, Y.; Wang, X.-J.; Chen, B.; Xue, H.; Zhao, Y.-P.; Lee, S.; Tung, C.-H.; Wu, L.-Z. Semiconducting Neutral Microstructures Fabricated by Coordinative Self-Assembly of Intramolecular Charge-Transfer Tetrathiafulvalene Derivatives, *Chemistry – A European Journal* **2009**, *15*, 5124-5129.
- [174] Kanehama, R.; Umemiya, M.; Iwahori, F.; Miyasaka, H.; Sugiura, K.-i.; Yamashita, M.; Yokochi, Y.; Ito, H.; Kuroda, S.-i.; Kishida, H.; Okamoto, H. Novel ET-Coordinated Copper(I) Complexes: Syntheses, Structures, and Physical Properties (ET = BEDT-TTF = Bis(ethylenedithio)tetrathiafulvalene), *Inorganic Chemistry* **2003**, *42*, 7173-7181.

- [175] Thangawng, A. L.; Howell Jr, P. B.; Richards, J. J.; Erickson, J. S.; Ligler, F. S. A simple sheath-flow microfluidic device for micro/nanomanufacturing: fabrication of hydrodynamically shaped polymer fibers, *Lab on a Chip* **2009**, *9*, 3126-3130.
- [176] Mas-Torrent, M.; Hadley, P.; Bromley, S. T.; Ribas, X.; Tarres, J.; Mas, M.; Molins, E.; Veciana, J.; Rovira, C. Correlation between crystal structure and mobility in organic field-effect transistors based on single crystals of tetrathiafulvalene derivatives, *Journal of the American Chemical Society* **2004**, *126*, 8546-8553.
- [177] Geiser, U.; Wang, H. H.; Hammond, C. E.; Firestone, M. A.; Beno, M. A.; Carlson, K. D.; Nunez, L.; Williams, J. M. Structure of di[3,4;3',4'-bis(ethylenedithio)-2,2',5,5'-tetrathiafulvalenium] dichlorocuprate(I), (BEDT-TTF)₂CuCl₂, *Acta Crystallographica Section C* **1987**, *43*, 656-659.
- [178] Hathaway, B. J.; Holah, D. G.; Postlethwaite, J. D. 630. The preparation and properties of some tetrakis(methylcyanide)copper(I) complexes, *Journal of the Chemical Society (Resumed)* **1961**, 3215-3218.
- [179] Bozio, R.; Zanon, I.; Girlando, A.; Pecile, C. Vibrational spectroscopy of molecular constituents of one-dimensional organic conductors. Tetrathiofulvalene (TTF), TTF⁺, and (TTF⁺)₂ dimer, *The Journal of Chemical Physics* **1979**, *71*, 2282-2293.
- [180] Curtis, N. F.; Curtis, Y. M. Some Nitrate-Amine Nickel(II) Compounds with Monodentate and Bidentate Nitrate Ions, *Inorganic Chemistry* **1965**, *4*, 804-809.
- [181] Jorgensen, T.; Hansen, T. K.; Becher, J. Tetrathiafulvalenes as building-blocks in supramolecular chemistry, *Chemical Society Reviews* **1994**, *23*, 41-51.
- [182] Novoa, J. J.; Rovira, M. C.; Rovira, C.; Veciana, J.; Tarrés, J. C.H...S and S...S: Two major forces in organic conductors, *Advanced Materials* **1995**, *7*, 233-237.
- [183] J. M. Williams, J. R. F., R. J. Thorn, K. D. Carlson, U. Geiser, H. H. Wang, A. M. Kini, and M.-H. Whangbo *Organic superconductors (including fullerenes): Synthesis, structure, properties, and theory.* ; Prentice Hall, Englewood Cliffs, NJ, 1992.
- [184] Inoue, M. B.; Inoue, M.; Fernando, Q.; Nebesny, K. W. Tetracyanoquinodimethan salts of copper chelate with tetrabenzo[b,f,j,n][1,5,9,13]tetraazacyclohexadecine: electrical properties and mixed-valence states, *The Journal of Physical Chemistry* **1987**, *91*, 527-530.
- [185] Kaim, W.; Moscherosch, M. The coordination chemistry of TCNE, TCNQ and related polynitrile π acceptors, *Coordination Chemistry Reviews* **1994**, *129*, 157-193.
- [186] Miller, J. S.; Calabrese, J. C.; Harlow, R. L.; Dixon, D. A.; Zhang, J. H.; Reiff, W. M.; Chittipeddi, S.; Selover, M. A.; Epstein, A. J. Ferromagnetic behavior of linear chain electron-transfer complexes. Decamethylferrocene electron-transfer salts of 2,5-disubstituted-7,7,8,8-tetracyano-*p*-quinodimethanes. Magnetic characterization of [Fe(C₆Me₅)₂]⁺[TCNQI₂]⁻ and structures of [TCNQI₂]ⁿ⁻ (n = 0, 1, 2), *Journal of the American Chemical Society* **1990**, *112*, 5496-5506.

- [187] Potember, R. S.; Hoffman, R. C.; Hu, H. S.; Cocchiaro, J. E.; Viands, C. A.; Poehler, T. O. Electronic Devices from Conducting Organics and Polymers, *Polymer Journal* **1987**, *19*, 147-156.
- [188] Zhao, H.; Heintz, R. A.; Ouyang, X.; Dunbar, K. R.; Campana, C. F.; Rogers, R. D. Spectroscopic, Thermal, and Magnetic Properties of Metal/TCNQ Network Polymers with Extensive Supramolecular Interactions between Layers, *Chemistry of Materials* **1999**, *11*, 736-746.
- [189] Liu, S.-G.; Liu, Y.-Q.; Wu, P.-J.; Zhu, D.-B. Multifaceted Study of CuTCNQ Thin-Film Materials. Fabrication, Morphology, and Spectral and Electrical Switching Properties, *Chemistry of Materials* **1996**, *8*, 2779-2787.
- [190] Liu, Y.; Ji, Z.; Tang, Q.; Jiang, L.; Li, H.; He, M.; Hu, W.; Zhang, D.; Jiang, L.; Wang, X.; Wang, C.; Liu, Y.; Zhu, D. Particle-Size Control and Patterning of a Charge-Transfer Complex for Nanoelectronics, *Advanced Materials* **2005**, *17*, 2953-2957.
- [191] O'Mullane, A. P.; Fay, N.; Nafady, A.; Bond, A. M. Preparation of Metal-TCNQ Charge-Transfer Complexes on Conducting and Insulating Surfaces by Photocrystallization, *Journal of the American Chemical Society* **2007**, *129*, 2066-2073.
- [192] Li, D.; Sutton, D.; Burgess, A.; Graham, D.; Calvert, P. D. Conductive copper and nickel lines via reactive inkjet printing, *Journal of Materials Chemistry* **2009**, *19*, 3719-3724.
- [193] Hansen, C. L.; Skordalakes, E.; Berger, J. M.; Quake, S. R. A robust and scalable microfluidic metering method that allows protein crystal growth by free interface diffusion, *Proceedings of the National Academy of Sciences* **2002**, *99*, 16531-16536.
- [194] Gucciardi, P. G.; Trusso, S.; Vasi, C.; Patane, S.; Allegrini, M. Nano-Raman imaging of Cu-TCNQ clusters in TCNQ thin films by scanning near-field optical microscopy, *Physical Chemistry Chemical Physics* **2002**, *4*, 2747-2753.
- [195] Xiao, K.; Ivanov, I. N.; Puretzky, A. A.; Liu, Z. Q.; Geohegan, D. B. Directed integration of tetracyanoquinodimethane-Cu organic nanowires into prefabricated device architectures, *Advanced Materials* **2006**, *18*, 2184-2188.

Appendix

A) Materials

SU-8 and developers for the resists were purchased from Microchem (Newton, MA, USA). 1H,1H,2H,2H-perfluorodecyl-dimethylchlorosilane was purchased from ABCR (Karlsruhe, Germany), and poly(dimethylsiloxane) (PDMS) (Sylgard 184) was obtained from Dow Corning (Midland, MI, USA). Acetonitrile (CH_3CN , 99.8+%), 4-Aminothiophenol (4-ATPh, 97%), 6-Aminofluorescein (95%), Cobalt(II) chloride hexahydrate ($\text{CoCl}_2 \cdot 6\text{H}_2\text{O}$, 98%), Copper(I) chloride powder (CuCl , 97%), Copper(II) chloride powder (CuCl_2 , 99%), Copper(II) sulfate (CuSO_4 , anhydrous, powder, $\geq 99.99\%$ trace metals basis), Dimethylsulfoxid (DMSO, 99.8+%), DL-Norepinephrine hydrochloride, ($\geq 97\%$ TLC), Dopamine hydrochloride, Ethanol (99.8+%), Ethanol (99.8+%), Gold(III) chloride trihydrate (HAuCl_4 , 99+% trace metal basis), Iron(II) chloride tetrahydrate ($\text{FeCl}_2 \cdot 4\text{H}_2\text{O}$, $\geq 99\%$), Iron(III) nitrate tetrahydrate ($\text{Fe}(\text{NO}_3)_3 \cdot 4\text{H}_2\text{O}$, $\geq 98\%$), Isoprenaline hydrochloride, L-Epinephrine, L-Phenylalanine ($\geq 99\%$), L-Tyrosine ($\geq 99\%$), Methanol (CH_3OH , 99.8+%), N-Hydroxysuccinimide (NHS, 98%), Nickel(II) chloride hexahydrate ($\text{NiCl}_2 \cdot 6\text{H}_2\text{O}$, 99.9%), Phosphate buffered saline (PBS) tablet, Sodium borohydride (NaBH_4 , powder, $\geq 98.0\%$), Sodium citrate dehydrate ($\text{C}_6\text{H}_5\text{O}_7\text{Na}_3 \cdot 2\text{H}_2\text{O}$), Sodium hydroxide (NaOH , reagent grade, $\geq 98\%$, pellets), and tetrahydrofuran (THF, anhydrous, $\geq 99.9\%$) were all purchased from Sigma-Aldrich (Buchs, Switzerland). 2-Aminoethanethiol hydrochloride (Cysteamine hydrochloride, 98%), Iron(III) chloride anhydrous (FeCl_3 , 98%), Manganese(II) chloride tetrahydrate ($\text{MnCl}_2 \cdot 4\text{H}_2\text{O}$, 99+%) were obtained from Acros Organics (Basel, Switzerland). Copper(II) nitrate trihydrate ($\text{Cu}(\text{NO}_3)_2 \cdot 3\text{H}_2\text{O}$, 98+%), Glutaraldehyde (GA, 50% in water solution) and Zinc chloride (ZnCl_2 , $\geq 98\%$) were purchased from Fluka (Buchs, Switzerland). Bis(ethylenedithio)-tetrathiafulvalene (BEDT-TTF), 1-Ethyl-3-(3-dimethylaminopropyl)carbodiimide hydrochloride (EDC, 98%), 2-Formyltetrathiafulvalene (FTTF, $\geq 98\%$), 7,7,8,8-Tetracyanoquinodimethane (TCNQ, $\geq 98.0\%$, HPLC), Tetrakis(ethylthio)tetrathiafulvalene (TET-TTF), 2,3,6,7-Tetrakis(2-cyanoethylthio)-tetrathiafulvalene (TCE-TTF) and Tetrathiafulvalene (TTF, 99+%) were obtained from TCI (Eschborn, Germany). Lissamine rhodamine B sulfonyl chloride (mixed isomers) and PBS solution (pH 7.40, 10 mM) were obtained

from Invitrogen (Lucerne, Switzerland). FITC-labeled human IgG antibody (0.5 mg/mL), Human IgG antibody (mAb mouse, 0.5 mg/mL) and Human IgG protein (4 mg/mL) were purchased from GenScript (Piscataway, NJ, USA). Cobalt(II) nitrate hexahydrate ($\text{Co}(\text{NO}_3)_2 \cdot 6\text{H}_2\text{O}$, $\geq 99.0\%$), Zinc nitrate hexahydrate ($\text{Zn}(\text{NO}_3)_2 \cdot 6\text{H}_2\text{O}$, extra pure) was purchased from MERCK (Merck Schuchardt OHG, Hohenbrunn, Germany). Nickel (II) nitrate hexahydrate ($\text{Ni}(\text{NO}_3)_2 \cdot 6\text{H}_2\text{O}$, GR for analysis) was purchased from VWR International AG (Dietikon, Switzerland). Ultrapure deionized (DI) water (Mill-Q purifiers, 18.2 $\text{M}\Omega \cdot \text{cm}$ at 25 °C) was used throughout the experiment.

B) Structures of important chemicals used Chapter 5.1

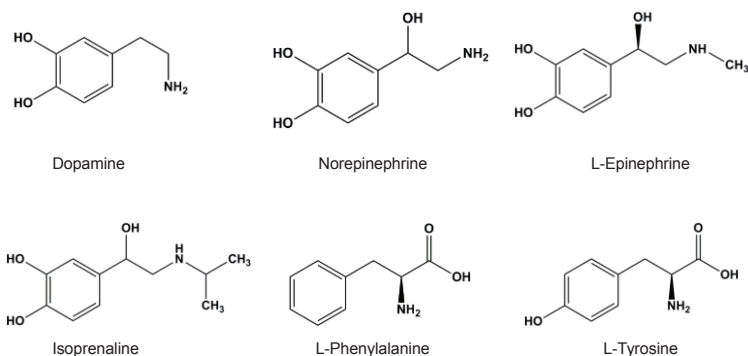


Figure 7.1. Structures of catecholamines and aromatic amino acids. Catecholamines including Dopamine (DA), Norepinephrine (NE), L-Epinephrine (EPI) and Isoprenaline (ISP). Aromatic amino acids including L-Phenylalanine (Phe) and L-Tyrosine (Ty).

Acknowledgement

First of all, I am very grateful to my supervisors, Prof. Dr. Norbert Esser and Prof. Dr. Petra S. Dittrich. It is because of their supervision and great support during the past three and a half years that I can finally manage to finish my doctoral research and this thesis. Great thanks to Prof. Esser for offering me the chance to work on this interesting and challenging project. Thanks for his constant encouragement, positive attitude and tireless effort in discussion on the project throughout the whole period. Thanks him for sharing inspiring and motivating insights in the interdisciplinary project.

Great thanks go to my second supervisor Prof. Petra S. Dittrich for giving me the opportunity to do research in her group in ETH Zürich. I am deeply impressed by her rich knowledge in microfluidics and bioanalytics, and also highly encouraged by her enthusiasm in doing research! Thanks for allowing me to follow my interests and small projects. This helped me not only to gain a broad understanding of my research field, but also to know how to refine research projects in the future.

Furthermore, I would like to thank all the examiners. Many thanks to Prof. Hildebrandt for agreeing to be the examiner with no hesitate. Thank all of them for their careful reading and revisions on this thesis. I appreciate all the suggestions, corrections and the time they invested. Great thanks goes to Prof. Birgit Kanngießner who agreed to be the chairman of my oral examination.

Following, I want to express my gratitude to my colleagues in Bioanalytics group of ETH Zürich: Dr. Eva Bönzli and Simone Stratz for their help in microfluidics experiments. My officemates in HCI F301, Dr. Tom Robinson for the valuable discussion and suggestions; Klaus Eyer for sharing biological samples and great help in sample preparation; Simon Küster for always keeping the nice working environment in the office. Also, my thanks goes to Dr. Daniel Schaffhauser for his great help in electrical measurements and valuable discussion on the results. Many thanks also for Pascal Verboket for chip design and microfabrication. Thank the whole group for the free time we spent together, badminton, Friday Bistro time, *etc.* These were so important to keep a free mind for better work. In addition, I want to address my gratitude to Christoph Bärtschi from the workshop, Dr. Karsten Kunze from the ScopeM Center for their help.

Great thanks to my colleagues in ISAS Berlin: Dr. Eugen Speiser, for his great help in my project, the valuable suggestions in experiment and useful

discussion in the results! Many thanks to Dr. Princia Salvatore for the very valuable discussion, useful suggestions and detailed corrections on this thesis. I want to thank Maximilian Ries for helping in translating the German abstract. Thank Dr. Maciej Neumann for his help in explaining the promotion system. Many thanks go to my officemates, Johannes Falkenburg (for the nice German-Chinese learning time and good suggestions on my presentation), Julian Plaickner, Timo Seemke for the good atmosphere in the office. It is very nice to share the office with them. I would like to thank the technician, Mr. Karsten Roland, also the other group members for their help.

Thank my collaborators, Andreas Wyss (D-MATL, ETH Zürich) for the Raman measurement, Dr. Guoguang Sun (ISAS Berlin) for the IR measurement and proof reading, Dr. Dheeraj Kumar Singh (Jacobs University, Bremen) for the DFT calculation.

Also, I would like to acknowledge the funding from DFG, with which I could do my research in Berlin and Zürich, also joining conferences to share and learn ideas. I enjoyed the period being a fellow of SALSA (School of Analytical Sciences Adlershof) which supports women in science during the past over three years. I want to thank the management director, Ms. Katharina Schultens, for her great support in feedback, discussion and suggestions. Also, deeply gratitude to Ms. Esther Santel for her help with everything. I will never forget the moment when I received her phone call in China in 2013. Thank other SALSA staff for their help and support. Thanks to my friends from SALSA school, Benita Schmidt and Natalia Ogorodnikova for their support and the friendship.

With the next few lines I want to direct my gratitude to my friends in Zürich and Berlin, Chengjun, Xiuxiu, Wenjie, Yuanyuan, Xiaojuan, Zhiyang and Jing, who always standing at my side. I never felt lonely when I was away from my family. Thanks for helping me settling down in the two cities and sharing the friendship, also the nice chats after work, about life, listening and advice.

Finally, I want to give my special and deep thanks to my family. Thanks for the support and love from my husband and my son during the separation period. Thanks to my husband Ming for sharing my depression when I encountered problems, and the joy when I made progress in work. Also thank my lovely son Zhitao who gives me a happy smile and a big hug every day. I could not manage to finish without their support. Their love is the power always encouraging me to pursue my life in scientific research, in the past and in the future!

Statement of authorship

This doctoral thesis will be submitted for the degree of Doctor rerum naturalium (Dr. rer. nat.). I hereby certify that this thesis was composed by myself about my work during the doctoral research period. All the collaborations and support from agencies and people have been specifically acknowledged. All references supporting this work have been quoted properly. I promise that this thesis does not contain any work extracted from a thesis, or research paper previously presented for another doctoral degree at this or other universities. I have prepared this thesis specifically for the degree of Dr. rer. nat., under supervision of Prof. Dr. Norbert Esser at the Leibniz-Institut für Analytische Wissenschaften – ISAS – e. V. Berlin during the period of May 2013 to October 2016 (with part of the cooperation work done in Eidgenössische Technische Hochschule Zürich).